

**DESIGN AND ANALYSIS OF  
SPECIALITY OPTICAL FIBER AND  
METAMATERIALS**

Thesis submitted by

**Reena**

In Partial Fulfilment of the Requirements for the Degree of  
**DOCTOR OF PHILOSOPHY**

Under the Supervision of

**Dr. AJEET KUMAR**

**&**

**Dr. YOGITA KALRA**



**Department of Applied Physics, Delhi Technological University  
Delhi, India**

**September-2021**



**©DELHI TECHNOLOGICAL UNIVERSITY-2021  
ALL RIGHTS RESERVED**





**DELHI TECHNOLOGICAL UNIVERSITY**  
(Govt. of National Capital Territory of Delhi)  
Shahbad Daultapur, Main Bawana Road,  
Delhi 110042, India

**CERTIFICATE**

This is to certify that the Ph.D. thesis entitled “**Design and analysis of speciality optical fiber and metamaterials**” submitted to the Delhi Technological University, Delhi for the award of the Doctor of Philosophy is based on the original research work carried out by me under the supervision of Dr. Ajeet Kumar and Dr. Yogita Kalra, Department of Applied Physics, Delhi Technological University, Delhi, India. It is further certified that the work embodied in this thesis has, neither partially nor fully submitted to any other university or institution for the award of any degree or diploma.

**Reena**

Candidate

(2K13/PhD/AP/06)

This is to certify that the above statement made by the candidate is correct to the best of our knowledge.

**Dr. Ajeet Kumar**

(Supervisor)

Assistant Professor

Department of Applied Physics

Delhi Technological University

**Dr. Yogita Kalra**

(Supervisor)

Assistant Professor

Department of Applied Physics

Delhi Technological University

25th September 2021

**Prof. Rinku Sharma**

(Head of the Department)

Department of Applied Physics

Delhi Technological University



## **ACKNOWLEDGEMENTS**

This thesis could have been accomplished with the help of many people for whom, I am very pleased to pay my gratitude.

First of all, I express my utmost gratitude to my supervisors Dr. Ajeet Kumar and Dr. Yogita Kalra for their proficient supervision and provided me peaceful and research oriented environment. I am grateful to them for their intellectual advice, prolific discussions, various suggestions, logical criticism and continuous support and motivation given to me during the period of my research. All these valuable things will definitely help me for further continuing my research.

I express respect towards the Honorable Vice-Chancellor, Delhi Technological University and Head of the Department, Applied Physics, Delhi Technological University for providing me worthy infrastructure for carrying my research work. I am further thankful to the SRC and DRC members for their valuable suggestions.

My sincere thanks to Prof. Ravindra Kumar Sinha whose suggestions and discussions helped me carrying out my research work.

I am thankful for my research fellows Dr. Than Singh Saini, Dr. Preeti Rani, Dr. Kamal Kishor, Dr. Venus Dillu, Dr. Nishant Shankhwar, Dr. Pooja Chauhan and Ms. Ritika Ranga who created positive, calm, helpful and assiduous environment in the laboratory. I am also thankful for all my friends who always motivates me.

Further, I am grateful to my respected and loving parents, for their love, support and encouragement. My caring and loving siblings Ms. Renu and Mr. Deepak Dalal, are always ready to help me. My humble thanks to my husband Mr. Sandeep Chaudhary, who is a sincere, punctual and workaholic person who always inspires and motivates me. I am also thankful to my respected parents-in-law whose blessings always stay over me. My sisters-in-law and brothers-in-law are also cooperative for me. My lovely kids Yashasvi and Agastya provide me stress free and healthy environment. I am indebted to all my family members for their moral support.

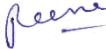
I acknowledge the DST for giving me opportunity to work in a project entitled “Specialty large mode area rectangular waveguides and fibers for high power applications” and granted

fellowship to carry out my research work. I carried out this project work under the supervision of Dr. Ajeet Kumar who was the principal investigator of the project.

I acknowledge the initiatives and support from the establishment of TIFAC-Centre of Relevance and Excellence in Fiber Optics and Optical Communication at Delhi Technological University (Formerly Delhi College of Engineering) Delhi, through the Mission REACH program of Technology Vision-2020 of the Government of India.

I am also thankful to the optical societies SPIE and OSA who gave me chance to enhance my network of research. They also provided me funding for attending workshops and conferences.

**Date: 24/09/2021**

  
**(Reena)**

**Place: Delhi**



## ABSTRACT

This thesis presents some novel designs related to optical fiber and metamaterials which are useful for the applications in many fields of optics and photonics. Special type of optical fibers like large mode area photonic crystal fiber designed in this thesis can be utilized for high power applications like high power lasers, amplifiers and sensors. The designs of metamaterials can be employed for nanoantenna, optical buffers and sensing applications.

The proposed rectangular core large mode area photonic crystal fiber in this work offers extended single mode operation by filtering all higher order modes. Higher order modes have been suppressed to ensure there is no modal dispersion despite large mode area so that non-linear effects could be avoided. Good beam quality can be obtained at the output end of the fiber laser using extended single mode operation. Size of air holes and Fluorine doped silica rods in the cladding region have been optimized to get better results. The proposed structure has an effective-mode area of fundamental mode as large as  $2147 \mu\text{m}^2$  at a wavelength of  $1.064 \mu\text{m}$  with very small loss of  $1.36 \times 10^{-2}$  dB/m. However, first higher order mode has very large confinement loss equal to 9.34 dB/m, which confirms effective single mode operation after 2.14 m propagation length. Moreover, this structure offers an extended single mode operation within a broad spectral range from  $\lambda = 1 \mu\text{m}$  to  $\lambda = 1.6 \mu\text{m}$  so that it is applicable in high power applications and communication.

Optical metamaterials are the artificially structured materials which are used to manipulate the direction of the flow of the light. In this work, all-dielectric and hybrid metal-dielectric metamaterials have been designed which are useful for the nanoantenna, optical buffers and sensing applications. Electric as well as magnetic dipoles have been optically induced in the nanoparticles. Azimuthally symmetric forward scattering with complete suppression of backward scattering using first Generalized Kerker's condition has been achieved for the allowed longitudinal mode and transverse modes in the optical region using single ellipsoidal nanoparticle. By changing the direction of the electric field, forward as well as backward scattering can be tuned at different wavelengths. Further, ellipsoidal core (Si) and shell ( $\text{SiO}_2$ ) metamaterial has been proposed for highly directional properties. In this case forward scattering has been attributed to the Fano resonance. Wavelengths at which Fano resonance takes place in the ellipsoidal nanoparticle exhibit higher directivity than the Kerker's type scattering or forward scattering shown by symmetrical structures like sphere and cube. In this

thesis, cuboidal nanoparticles in the shape of nanodisk and nanorod have been utilized as dielectric nanoantennas in the visible range. The dimensions of the nanoparticles have been tailored to bring the electric and magnetic dipoles together so that both of them spectrally overlap and on-resonance scattering of electric and magnetic dipole moments take place. There is a Fano dip in the backward scattering and therefore there is an enhancement in the forward scattering which leads to the improvement in directivity and radiation efficiency. These designs have applications in highly directional nanoantennas.

In this thesis, electromagnetically induced transparency has been reported in the Terahertz region which is useful for the optical buffers and ultrasensitive refractive index sensors. In the proposed design, electric dipole has been excited in the metal ring which serves as a bright mode and in the dielectric cube resonator, magnetic and electric dipole have been induced which act as quasi-dark mode and bright mode, respectively. Electric dipole of the metal ring interferes with the electric as well as magnetic dipoles of the dielectric cube which creates an EIT window in a broad region from 1.8 THz to 2.2 THz. A steep and constant phase change in transmission results in high group delay of 5 ps in the broad EIT window so that a large delay bandwidth product equal to 2 could be obtained so that it is useful in the application of optical buffers. Also, Metal dielectric structure provides the platform for high quality factor Fano resonance. Two resonance dips have been obtained with high quality factor using the metal-dielectric metamaterial Fano resonator. The quality factor of the Fano resonator turns out to be  $Q = 89.5$  at the first dip and  $Q = 23$  for the second Fano dip. This high quality factor leads to high figure of merit of sensor equal to 6 and 4 for first and second resonance dips, respectively which is useful for metamaterial based sensing devices and bio-sensors.

## **LIST OF PUBLICATIONS**

### **Publications in Refereed International Journals (Thesis)**

- [1] **Reena**, T. S. Saini, A. Kumar, Y. Kalra, and R. K. Sinha, “Rectangular-core large-mode-area photonic crystal fiber for high power applications: design and analysis,” *Applied Optics*, 55 (15), 4095 – 4100 (2016).
- [2] **Reena**, Y. Kalra, A. Kumar, and R. K. Sinha, “Tunable unidirectional scattering of ellipsoidal single nanoparticle,” *Journal of Applied Physics*, 119, 234102 (2016).
- [3] **R. Reena**, Y. Kalra, and A. Kumar, “Ellipsoidal all-dielectric Fano resonant core-shell metamaterials,” *Superlattices and Microstructures*, 118, 205 - 212 (2018).
- [4] **R. Reena**, Y. Kalra and A. Kumar, “Fano Resonant Cuboidal Dielectric Nanoantennas,” *Optics and Spectroscopy*, 127, 1122-1127 (2019).
- [5] **R. Reena**, Y. Kalra and A. Kumar, “Electromagnetically induced transparency-based metal dielectric metamaterial and its terahertz sensing application,” *Applied Optics*, 60(34), 10610-10616 (2021).

### **Publications in Refereed International Journals (outside Thesis)**

- [1] I. Devi, **R. Dalal**, Y. Kalra, and R. K. Sinha, “Modeling and design of all-dielectric cylindrical nanoantennas,” *Journal of Nanophotonics* 10, 046011-046011 (2016).

### **Publications in Refereed International Conferences and workshops (Thesis)**

- [1] **R. Dalal**, P. Rani, Y. Kalra and R. K. Sinha, “Zero backscattering by ellipsoidal single nanoparticle,” In *Laser Science*, pp. JW2A-77. Optical Society of America, 2015.
- [2] **R. Dalal**, Y. Kalra and R. K. Sinha, “Mie resonance in the arrays of dielectric rods in air,” In *Metamaterials, Metadevices, and Metasystems 2015*, vol. 9544, p. 95442X. International Society for Optics and Photonics, 2015.

- [3] **Reena**, I. Devi, Y. Kalra, & R. K. Sinha, “Multipolar optically induced electric and magnetic resonances in the ellipsoidal nanoparticles,” In Nanophotonic Materials XIII, vol. 9919, p. 99190T. International Society for Optics and Photonics, 2016.
- [4] **R. Dalal**, N. Shankhwar, Y. Kalra, A. Kumar and R. K. Sinha, “Fano resonant all-dielectric core-shell nanoparticles,” In Frontiers in Optics, pp. JW3A-67. Optical Society of America, 2017.
- [5] **R. Dalal**, Y. Kalra, and R. K. Sinha, “Forward scattering by the cylindrical dielectric nanoparticle,” In International Conference on Fibre Optics and Photonics, pp. Th4E-4. Optical Society of America, 2016.
- [6] **R. reena**, Y. Kalra, and R. K. Sinha, “Electric and magnetic hotspots in the Silicon Bow-Tie nanocavity,” In Frontiers in Optics, pp. JW4A-154. Optical Society of America, 2016.
- [7] **R. Dalal**, N. Shankhwar, Y. Kalra, A. Kumar and R. K. Sinha, “All-dielectric cylindrical nanoantennas in the visible range,” In Nanophotonic Materials XIV, vol. 10344, p. 103440K. International Society for Optics and Photonics, 2017.
- [8] **Reena**, Y. Kalra, A. Kumar, “Highly directional all-dielectric core-shell nanoantenna,” In Optics and Photonics: Theory and Computational Techniques, 2018.
- [9] **Reena**, Y. Kalra, A. Kumar, “Enhancement of Purcell factor in all-dielectric dimer.” Nanophotonic Materials XV. Vol. 10720. International Society for Optics and Photonics, 2018.

### **Publications in Refereed International Conferences and workshops (Outside Thesis)**

- [1] P. Rani, **R. Dalal**, Yogita Kalra and R. K. Sinha, “Polarization splitter in silicon-on-insulator photonic crystal; design and simulation,” In Frontiers in Optics, pp. FTu2B-5. Optical Society of America, 2015.
- [2] I. Devi, **Reena**, Y. Kalra and R. K. Sinha, “Design of tunable cylindrical dielectric nanoantenna,” In Nanophotonic Materials XIII, vol. 9919, p. 991903. International Society for Optics and Photonics, 2016.
- [3] N. Shankhwar, **R. Dalal**, Y. Kalra, A. Kumar and R. K. Sinha, “LiTaO<sub>3</sub> microcubes based metamaterial perfect absorber,” In Metamaterials, Metadevices, and

Metasystems 2017, vol. 10343, p. 103432L. International Society for Optics and Photonics, 2017.



# CONTENTS

---

<b>Title</b>	<b>Page No.</b>
Certificate	I
Acknowledgements	III
Abstract	V
List of Publications	VII
Contents	XI
List of Figures	XIII
List of Abbreviations	XIX

---

**1. Introduction**

---

<b>1.1</b> Introduction	3
<b>1.2</b> Speciality Optical Fibers	3
<b>1.2.1</b> Dispersion shifted fibers	5
<b>1.2.2</b> Dispersion compensating fibers	5
<b>1.2.3</b> Dispersion flattening fibers	5
<b>1.2.4</b> Multi-core fibers	6
<b>1.2.5</b> Photonic crystal fibers	6
<b>1.3</b> Metamaterials	8
<b>1.3.1</b> Metallic metamaterials	10
<b>1.3.2</b> Dielectric metamaterials	10
<b>1.3.3</b> Hybrid metal-dielectric metamaterials	11
<b>1.4</b> Overview of the Thesis	12
References	16

---

**2. Rectangular-core large-mode-area photonic crystal fiber for high power applications**

---

<b>2.1</b> Introduction	25
<b>2.2</b> Design Parameters of RCLMA PCF	27
<b>2.3</b> Formulation and Method of Analysis	28
<b>2.4</b> Numerical Results and Discussion	28
<b>2.5</b> Conclusion	34
References	36

---

---

### **3. Tunable unidirectional scattering of ellipsoidal dielectric meta-atom**

<b>3.1</b> Introduction	41
<b>3.2</b> Design Parameters of the Meta-atom	44
<b>3.3</b> Dipole Analysis	45
<b>3.4</b> Generalized Kerker's Condition	48
<b>3.5</b> Conclusion	52
References	53

---

### **4. Ellipsoidal all-dielectric Fano resonant core-shell metamaterials**

<b>4.1</b> Introduction	59
<b>4.2</b> Design and Analysis	61
<b>4.3</b> Results and Discussion	63
<b>4.4</b> Conclusion	69
References	70

---

### **5. Fano resonant cuboidal dielectric metamaterial nanoantennas**

<b>5.1</b> Introduction	75
<b>5.2</b> Design and Analysis	76
<b>5.3</b> Results and Discussion	79
<b>5.3.1</b> Forward and Backward Scattering Intensity	79
<b>5.3.2</b> Radiation Efficiency	84
<b>5.4</b> Conclusion	86
References	87

---

### **6. Electromagnetically induced transparency in metal-dielectric metamaterial**

<b>6.1</b> Introduction	91
<b>6.2</b> Design Parameters of the Metamaterial	94
<b>6.3</b> Resonance Properties	95
<b>6.4</b> Delay Bandwidth Product	101
<b>6.5</b> Analyte Thickness and Refractive Index Sensing	102
<b>6.6</b> Conclusion	106
References	108

---

### **7. Concluding Remarks and Future Scope**

---

115



## LIST OF FIGURES

**Fig. 1.1 (a) – (c)** Refractive index profiles ( $n$ ) of dispersion shifted fiber (DSF), dispersion compensating fiber (DCF) and dispersion flattened fiber (DFF) with respect to the distance from the center of core ( $r$ ). **(d) – (f)** Dispersion ( $D$ ) of dispersion shifted fibers (DSF), dispersion compensating fiber (DCF) and dispersion flattened fiber (DFF) with respect to the wavelength of operating wavelength ( $\lambda_0$ ) Dashed curves represent the dispersion in conventional single mode step index fiber.

.....(4)

**Fig. 1.2 (a)** Solid core and **(b)** Hollow core photonic crystal fiber.

.....(4)

**Fig. 1.3** Electric field distribution in the **(a)** metallic split ring resonator and **(b)** high index dielectric resonator. White arrows represent the direction of electric field and purple arrow in the center represent the direction of magnetic field.

.....(9)

**Fig. 2.1** Transverse view of rectangular core large mode area photonic crystal fiber.

.....(27)

**Fig. 2.2** Variation of the effective mode indices of FM, FHOM and SHOM with  $r_1$  while keeping other parameters fixed as  $n_f = 1.435$ ,  $r_2 = 2 \mu\text{m}$ ,  $A = 19 \mu\text{m}$  and  $\lambda = 1.064 \mu\text{m}$ .

.....(29)

**Fig. 2.3** Variation of the effective-mode-area of FM and the confinement losses of FM, FHOM and SHOM modes with  $r_1$  while keeping other parameters fixed,  $n_f = 1.435$ ,  $r_2 = 2 \mu\text{m}$ ,  $A = 19 \mu\text{m}$  and  $\lambda = 1.064 \mu\text{m}$ .

.....(29)

**Fig. 2.4** Variation of effective mode indices of FM, FHOM and SHOM with  $r_2$  while keeping other parameters fixed as:  $n_f = 1.435$ ,  $r_1 = 1.5 \mu\text{m}$ ,  $A = 19 \mu\text{m}$ , and  $\lambda = 1.064 \mu\text{m}$ .

.....(30)

**Fig. 2.5** Variation of effective-mode-area of FM and the confinement losses of FM, FHOM and SHOM modes with  $r_2$  while keeping other parameters fixed as:  $n_f = 1.435$ ,  $r_1 = 1.5 \mu\text{m}$ ,  $A = 19 \mu\text{m}$ , and  $\lambda = 1.064 \mu\text{m}$ .

.....(31)

**Fig. 2.6** Variation of effective mode indices of FM, FHOM and SHOM modes with refractive index of fluorine doped rods while keeping other parameter fixed as:  $r_1 = 1.5 \mu\text{m}$ ,  $r_2 = 2 \mu\text{m}$ ,  $A = 19 \mu\text{m}$ , and  $\lambda = 1.064 \mu\text{m}$ .

.....(31)

**Fig. 2.7** Variation of effective-mode-area of FM and the confinement loss of FM, FHOM and SHOM modes with refractive index of fluorine doped rods while keeping other parameter fixed as:  $r_1 = 1.5 \mu\text{m}$ ,  $r_2 = 2 \mu\text{m}$ ,  $A = 19 \mu\text{m}$  and  $\lambda = 1.064 \mu\text{m}$ .

.....(32)

**Fig. 2.8** Variation of effective mode area of FM and the confinement loss of FM, FHOM and SHOM with pitch while keeping other parameter fixed as:  $n_f = 1.435$ ,  $r_1 = 1.5 \mu\text{m}$ ,  $r_2 = 2 \mu\text{m}$ ,  $\lambda = 1.064$ .

.....(33)

**Fig. 2.9** Variation of effective mode area of FM and the confinement loss of FM, FHOM and SHOM with wavelength while keeping other parameter fixed as:  $n_f = 1.435$ ,  $r_1 = 1.5 \mu\text{m}$ ,  $r_2 = 2 \mu\text{m}$ , and  $\Lambda = 19 \mu\text{m}$ .

.....(34)

**Fig. 2.10** Contour plot of the normalized electric field intensity of FM and FHOM modes at optimized parameters as:  $n_f = 1.435$ ,  $r_1 = 1.5 \mu\text{m}$ ,  $r_2 = 2 \mu\text{m}$ ,  $\Lambda = 19 \mu\text{m}$ , and  $\lambda = 1.064 \mu\text{m}$ .

.....(34)

**Fig. 3.1 (a)** Orientation of the major-axis of the ellipsoidal nanoparticle in the laboratory frame around the x-axis or the direction of propagation  $k$  with angle  $\theta$ . **(b)** Rotation of the nanoparticle around the major-axis with angle  $\phi$ .

.....(44)

**Fig. 3.2 (a)** Scattering cross-section of the ellipsoidal nanoparticle when  $E \parallel$  to  $a$ -axis of the ellipsoid **(b) - (c)** Electric field inside the nanoparticle forming electric dipole and magnetic dipole. White arrows indicate electric lines of force.

.....(47)

**Fig. 3.3 (a)** Variation of scattering cross-section with wavelength when  $E \parallel b$ -axis of the ellipsoid **(b) - (c)** Electric field distribution patterns at the wavelengths where electric and dipoles are created.

.....(47)

**Fig. 3.4 (a)** Plot of scattering cross section with wavelength when  $E \parallel c$ -axis of the ellipsoidal nanoparticle. **(b) - (c)** Electric field distribution and direction of electric field shown by white lines.

.....(48)

**Fig. 3.5 (a)** Plot of real and imaginary parts of electric and magnetic polarizabilities of the nanoparticle with wavelength when  $E \parallel a$ -axis. **(b) - (c)** Far field scattering patterns show forward scattering at wavelength 680 nm and backward scattering at 607 nm.

.....(50)

**Fig. 3.6 (a)** Variation of electric and magnetic polarizabilities of the nanoparticle with wavelength when  $E \parallel b$ -axis. **(b) - (c)** Far field scattering patterns show forward scattering at wavelength 912 nm and backward scattering at 784 nm.

.....(51)

**Fig. 3.7 (a)** Wavelength dependence of real and imaginary parts of electric and magnetic polarizabilities of the nanoparticle when  $E \parallel c$ -axis. **(b) - (c)** Far field scattering patterns show forward scattering at wavelength 778 nm and backward scattering at 585 nm.

.....(52)

**Fig. 4.1** Schematic diagram of ellipsoidal nanoparticle **(a)** in the y-z plane and **(b)** in the x-y plane.

.....(61)

**Fig. 4.2** Scattering cross section of the nanoparticle representing broad electric dipole (ED) spectra and narrow magnetic dipole (MD) resonance.

.....(63)

**Fig. 4.3** Normalized forward (FW) and backward (BW) scattering intensity showing Fano dip of backward scattering at  $\lambda = 640$  nm and enhancement of forward scattering at the same wavelength.

.....(64)

**Fig. 4.4 (a)** Scattering spectra of ellipsoidal nanoparticle depicting distinct curves of dipoles and quadrupoles for core radius  $b = 35$  nm. **(b)** Forward and backward normalized scattering intensity showing Fano dips in the backward scattering at the wavelengths 490 nm and 440 nm due to dipole and quadrupole moments respectively. **(c) – (d)** Far-field scattering patterns at the Fano dip wavelengths.

.....(65)

**Fig. 4.5 (a)** Scattering spectra of the ellipsoidal nanoparticle at  $b = 55$  nm. **(b)** Forward and backward normalized scattering intensity showing Fano dips in the backward scattering at the wavelengths 600 nm and 540 nm. **(c) – (d)** Far-field scattering patterns at the Fano dip wavelengths.

.....(66)

**Fig. 4.6 (a)** Scattering spectra of the ellipsoidal nanoparticle at  $b = 75$  nm. **(b)** Forward and backward normalized scattering intensity showing Fano dip in the backward scattering at the wavelength 650 nm due to dipole moments only. **(c)** Variation of wavelength of Fano dips,  $FD_1$  and  $FD_2$  with length of semi-axis of ellipsoidal nanoparticle along electric field. **(d)** Far field scattering pattern at 650 nm.

.....(67)

**Fig. 4.7 (a)** Scattering spectra of the spherical nanoparticle of core radius 70 nm and shell thickness 80 nm. **(b)** Forward and backward normalized scattering intensity showing Fano dip in the backward scattering at the wavelength 630 nm due to dipole moments only. **(c)** Far field scattering pattern at 630 nm.

.....(68)

**Fig. 5.1** Schematic diagram of plane wave incident on cuboidal silicon nanoparticles transformed into the shape of **(a)** disk and **(b)** rod.

.....(77)

**Fig. 5.2 (a)** Scattering cross section spectra of cube having length 200 nm corresponding to electric dipole (ED) and magnetic dipole (MD). **(b)** Normalized forward (FW) and backward (BW) scattering.

.....(79)

**Fig. 5.3** Scattering cross section spectra for the electric dipole moment (ED) and magnetic dipole moment (MD) of the cuboidal nanodisk having dimensions  $a = b = 200$  nm (a)  $c = 50$  nm (b)  $c = 60$  nm (c)  $c = 70$  nm and (d)  $c = 80$  nm (e)-(h) Corresponding normalized scattering intensity depicting forward and backward scattering for  $c = 50 - 80$  nm. (i) Forward scattering intensity (j) backward scattering intensity of the cuboidal nanodisk with respect to wavelength and dimension of the nanodisk. (k) Forward to backward intensity ratio.  
 .....(81)

**Fig. 5.4** Scattering cross section spectra for the electric dipole moment (ED) and magnetic dipole moment (MD) of the cuboidal nanorod having dimensions  $a = b = 80$  nm (a)  $c = 80$  nm (b)  $c = 200$  nm and (c)  $c = 300$  nm (d)-(f) Corresponding normalized scattering intensity depicting forward and backward scattering for  $c = 80 - 300$  nm. Inset of the figure (f) shows Fano dip at the wavelength 520 m. (g) forward scattering intensity (h) backward scattering intensity of the cuboidal nanodisk with respect to wavelength and dimension of the nanodisk. (i) Forward to backward (FW/BW) intensity ratio.  
 .....(82)

**Fig. 5.5** Radiation efficiency of the disk having dimensions  $a = b = 200$  nm and  $c = 50$  nm. The inset shows the three dimensional radiation pattern at the wavelength 440 nm with directivity 3.9 in the forward direction.  
 .....(84)

**Fig. 5.6** Radiation efficiency and of the rod having dimensions  $a = b = 80$  nm and  $c = 200$  nm. The inset shows the three dimensional radiation pattern at the wavelength 520 nm having directivity 4.2 in the forward direction.  
 .....(85)

**Fig. 6.1** (a) 3-D and (b) 2-D view of the unit cell of the metamaterial along with dimensions showing normally incident excitation. In the geometry, at the top there is a dielectric cube of side  $a = 35$   $\mu\text{m}$ , in the bottom there is a metal ring of side  $l = 50$   $\mu\text{m}$ , width  $r = 6$   $\mu\text{m}$  and thickness  $d = 1.5$   $\mu\text{m}$ . Dielectric cube and metal ring are separated by a glass spacer of height  $p = 20$   $\mu\text{m}$ . (c) Periodic array of metamaterial with periodicity  $s = 65$   $\mu\text{m}$ .  
 .....(94)

**Fig. 6.2** (a) Transmission spectra of metal ring with spacer by varying the length of the ring. (b) Electric field distribution in the metal ring on the top of the spacer at electric dipolar resonance frequency for  $l = 50$   $\mu\text{m}$  at 1.72 THz. Black arrows represent the direction of electric field.  
 .....(96)

**Fig. 6.3** (a) Transmission spectra of the dielectric with spacer showing magnetic resonance at 1.79 THz and electric resonance at 2.3 THz. Electric field distribution of the dielectric at (b) magnetic resonance frequency and (c) electric resonance frequency. Black arrows in the figures (b) and (c) depict the directions of the electric field.  
 .....(97)

**Fig. 6.4** Transmission spectra of the EIT resonator with both dielectric and metal ring with glass spacer in between the both. Transmittance has been plotted for different length of the metal ring from  $l = 40$   $\mu\text{m}$  to  $l = 55$   $\mu\text{m}$ .  
 .....(99)

**Fig. 6.5 (a).** Transmittance spectra of EIT resonator for length of the ring,  $l = 50 \mu\text{m}$ . Electric field distribution in the hybrid EIT resonator at **(b)** 1.6 THz **(c)** 1.75 THz **(d)** 1.8 THz **(e)** 2.1 THz **(f)** 2.25 THz frequencies. Black arrows in the figures **(b)** - **(f)** depict the directions of the electric field.  
 .....(100)

**Fig. 6.6 (a)** Transmission phase in radians and **(b)** Group delay in picoseconds of the hybrid EIT metamaterial resonator.  
 .....(102)

**Fig. 6.7** Fano resonator as a sensing device with analyte on the top of it.  
 .....(102)

**Fig. 6.8** Transmission spectra of the Fano resonator for different analyte thicknesses with fixed refractive index of the analyte **(a)** for first Fano resonance dip and **(b)** second Fano dip.  
 .....(103)

**Fig. 6.9** Transmission spectra of the Fano resonator for different refractive index of analyte with fixed thickness of the analyte **(a)** for first Fano resonance dip and **(b)** second Fano resonance dip.  
 .....(104)

**Fig. 6.10** Frequency shift with respect to **(a)** analyte thickness and **(b)** refractive index of the analyte.  
 .....(105)

**Fig. 6.11** Figure of merits of first and second Fano dips with respect to the thickness of the analyte.  
 .....(105)



## **LIST OF ABBREVIATIONS**

- PCF: Photonic Crystal Fiber
- CSF: Conventional single mode fiber
- DSF: Dispersion shifted fiber
- DCF: Dispersion compensating fiber
- DFF: Dispersion flattening fiber
- WDM: Wavelength division multiplexing
- DWDM: Dense wavelength division multiplexing
- SDM: Space division multiplexing
- LMA: Large Mode Area
- RC: Rectangular Core
- PML: Perfectly Matched Layer
- MCVD: Modified Chemical Vapor Deposition
- FM: Fundamental Mode
- FHOM: First Higher Order Mode
- SHOM: Second Higher Order Mode
- SRR: Split Ring Resonator
- TM: Transverse Mode
- LM: Longitudinal Mode
- ED: Electric Dipole
- MD: Magnetic Dipole
- FEM: Finite Element Method
- FD: Fano Dip
- EIT: Electromagnetically Induced Transparency

- DBP: Delay Bandwidth Product
- RIU: Refractive Index Unit



# **CHAPTER-1**



---

# **CHAPTER-1**

---

## **INTRODUCTION**

---

### **1.1 Introduction**

Due to the increasing demands of data transmission, data storage and signal processing in the field of computing and communication, optical and photonic devices have become a subject of considerable interest. After the invention of laser in 1960, optical world has revolutionized not only the field of communication but also offered its excellence in the fields of medical sciences, industry, defense, printing, green technology, optical sensing, imaging and spectroscopy [1- 4]. In future, electronic circuits would be replaced by photonic circuits for data transmission and computing due to low loss, high speed and less energy consumption. Optical and photonic devices like optical fibers and metamaterials have the ability to routing, confining and modulation of light in a useful manner at micro and nano scales. In this thesis, special types of optical fibers and metamaterials have been designed and their analysis have been done for various applications like high power fiber lasers, amplifiers, nanoantennas, optical memory and sensing.

### **1.2 Speciality optical fibers**

Optical fiber is a structure that consists of a cylindrical central dielectric core usually made up of silica which is surrounded by cladding made up of dielectric material of a slightly lower

refractive index used to confine and guide light beam from one place to another by the mechanism of total internal reflection. Conventional single mode optical fibers (CSF) are mainly step index fibers and they were initially optimized to operate at 1330 nm wavelength since material dispersion is very low in the silica at this wavelength. However, power loss is high in the conventional single mode optical fibers due to which a large number of amplifiers are required. In order to minimize the losses, to increase the transmission capacity in the optical fiber and to utilize the optical fiber for various applications, different kinds of speciality optical fibers have been designed [5 - 33].

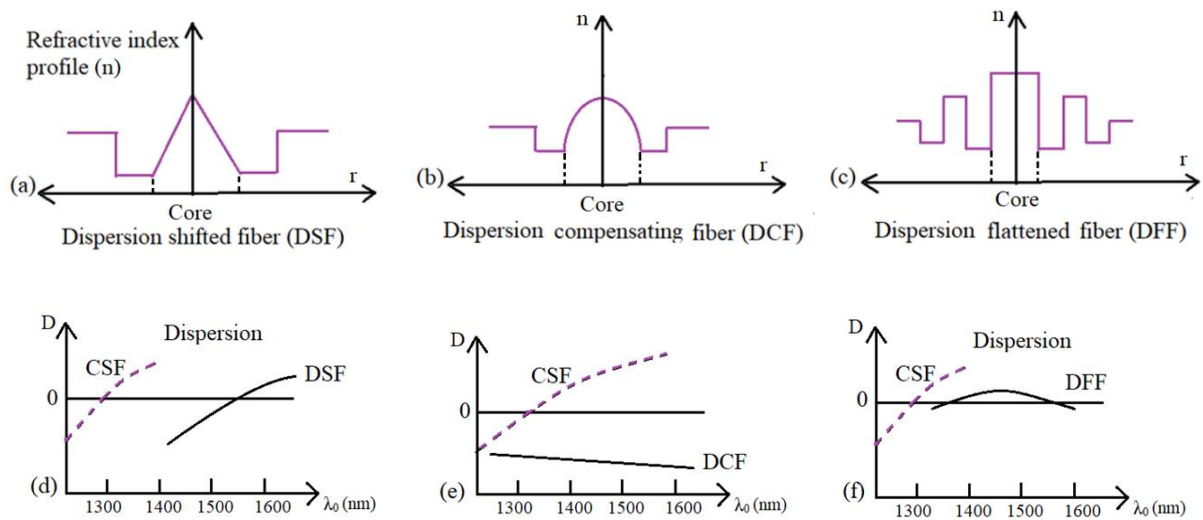


Figure 1.1. (a) – (c) Refractive index profiles (n) of dispersion shifted fiber (DSF), dispersion compensating fiber (DCF) and dispersion flattened fiber (DFF) with respect to the distance from the center of core (r). (d) – (f) Dispersion (D) of dispersion shifted fibers (DSF), dispersion compensating fiber (DCF) and dispersion flattened fiber (DFF) with respect to the wavelength of operating wavelength ( $\lambda_0$ ). Dashed curves represent the dispersion in conventional single mode step index fiber.

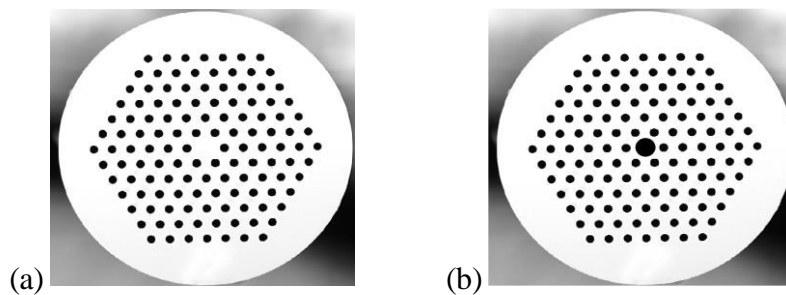


Figure 1.2. (a) Solid core and (b) Hollow core photonic crystal fiber.

Some of the speciality optical fibers are as follows:

### **1.2.1 Dispersion shifted fibers**

The loss of silica attains a minimum value of nearly 0.2 dB/Km at 1550 nm of wavelength. Therefore, special type of optical fibers have been designed which have nearly -19 ps/Km/nm waveguide dispersion to compensate the material dispersion of 19 ps/Km/nm at 1550 nm so that minimum loss and low dispersion could be obtained. Such type of optical fibers are called dispersion shifted fibers (DSFs). Most of the DSFs have triangular shape refractive index profile core as shown in the figure 1.1 (a). Dispersion profile of DSF has been shown in figure 1.1 (d) which shows zero dispersion at the wavelength 1550 nm. The main disadvantage of DSFs is that they have short cut-off wavelength so that fibers become sensitive to bending loss.

### **1.2.2 Dispersion compensating fibers**

The CSFs have zero dispersion at around 1300 nm of wavelength but attenuation is higher than the 1550 nm of wavelength. It would have been very costly and cumbersome to replace CSFs by DSFs. Therefore, to exploit the lowest-loss window around 1550 nm with the existing fiber network of CSFs and to utilize wavelength division multiplexing (WDM) to increase the data capacity, special kind of optical fibers have been designed with very large negative waveguide dispersion which could be used to compensate the dispersion in the CSFs operating at 1550 nm. Such type of speciality optical fibers are called dispersion compensating fibers (DCFs) and they can be applied at the end of the CSFs to reverse the pulse broadening caused by chromatic or material dispersion and to restore the original pulse shape. Refractive index profile of DCF is dome-like shape as shown in the figure 1.1 (b) and dispersion profile of DCF has been shown in the figure 1.1 (e).

### **1.2.3 Dispersion flattening fibers**

As DSFs have zero dispersion at 1550 nm wavelength only but have large dispersion at other wavelengths so that only one laser around 1550 nm could only be used for data transmission otherwise there would be four wave mixing while carrying signals from multiple lasers. Therefore, dense wavelength division multiplexing (DWDM) cannot be possible in DSFs. Therefore, to increase the data transmission capacity dispersion flattening fibers (DFF) have been utilized for DWDM. Refractive index profile ( $n$ ) and dispersion ( $D$ ) have been shown in the figures 1.1 (c) and 1.1 (f), respectively. They have very low dispersion in a very broad region of wavelength from 1300 nm to 1600 nm.

### **1.2.4 Multi-core fibers**

Multi-core fibers are the speciality optical fibers having multiple cores within the same cladding. These types of speciality fibers have been used for space division multiplexing (SDM) to increase the data capacity of transmission by reducing the construction costs.

### **1.2.5 Photonic crystal fibers**

Photonic crystal fibers (PCFs) are the special type of optical fibers that consist of silica core surrounded by micro-structured cladding having regular array of air holes. In these kinds of photonic crystal fibers, where core is made up of silica, light is confined to the solid core by total internal reflection. There is another type of photonic crystal fibers where light is guided by the mechanism of photonic band gap. In such PCFs, core is made up of air hole instead of silica. Among all the speciality optical fibers, photonic crystal fibers are most popular now-a-days due to their amazing properties like endlessly single-mode, large mode-area, efficient dispersion management and low confinement losses [9-12]. These properties are highly desirable in telecommunications, sensing, high power fiber lasers and amplifiers and sensing [9 - 20]. In high power devices, the main limitation in its performance consists of nonlinear effects such as self-phase modulation, four-wave mixing, stimulated Raman scattering, and

stimulated Brillouin scattering [19, 20]. These limitations due to nonlinear effects may be overcome by using large mode area (LMA) fibers. LMA fibers have potential applications in different fields such as high power delivery, multi-wavelength guidance, short pulse delivery and broadband interferometry. LMA fiber facilitates high power levels to be transmitted through the optical fiber without the effects produced by the nonlinear properties of the fiber. Due to the increase of numerical aperture (NA), fiber with LMA is limited by the fact that fiber becomes multimode, which causes modal dispersion. Therefore, it is difficult to obtain single mode using LMA.

The LMA and single-mode operation can also be obtained by scaling down the NA of the conventional step index fiber [21] and by using special cladding geometries or index profiles to discriminate higher order modes [22 - 25]. A graded index cladding design with a radial increase of refractive index profile has been proposed for optical fiber for LMA single-mode operation [22]. A LMA optical fiber design consisting of a cladding formed by alternative high and low index regions has been proposed [23]. LMA with single-mode operation optical fiber design with coaxial dual cores and leaky cladding has been proposed [24]. Dussardier et al. fabricated a LMA with single-mode operation based on leaky-mode filtering by a modified chemical vapour deposition (MCVD) technique [25]. This fiber structure has a leaky cladding that discriminates the fundamental mode from higher order modes. However, there are some disadvantages of these LMA step-index fibers. The extended single-mode operation is impossible in conventional LMA fiber. A few higher order modes are always supported in this type of LMA fiber.

However, the PCF structure has many interesting properties compared to the conventional fibers. Earlier, different design approaches of air holes in the cladding region had been considered for achieving LMA PCFs with single-mode operation. A high power air-clad microstructure ytterbium-doped PCF laser has been demonstrated with a  $350 \mu\text{m}^2$  mode field

area of the propagating mode [26]. Tsuchida et al. proposed a novel LMA PCF with single-mode operation and low bending loss for high power delivery applications [27]. Using the fact that silica PCF with a doped central core enables the reduction of confinement and bending losses, a novel technique has been applied to improve these properties in LMA PCF by employing a different level of doping concentration around the core region [28]. Napierala et al. demonstrated experimentally an asymmetric design having a set of small air holes on one side of the fiber and larger air holes on the opposite sides [29]. In this PCF design, for increasing the loss of higher order modes at the bending of the PCF, two additional missing air holes are inserted in the cladding region. Ademgil and Haxha proposed endlessly single-mode PCF with improved effective-mode area based on introducing higher index material in the cladding region [30]. The effective-mode area of the proposed PCF reported is smaller than  $200 \mu\text{m}^2$  at  $1.064 \mu\text{m}$  wavelength. LMA PCF structures have been designed based on selective material-filled technology [31, 32]. Photonic bandgap fiber with single-mode operation and multiple cladding regions has been designed with a very large mode area of  $\sim 2650 \mu\text{m}^2$  [33].

In this thesis, rectangular-core (RC) LMA PCF structure has been proposed that offers extended single-mode operation by suppressing all higher order modes. The PCF is designed in such a way that initially it supports several leaky modes, out of which only the fundamental mode survives after a finite propagation length. A 20 dB confinement loss to the first higher order modes ensures effective single-mode operation. The proposed PCF structure supports effective single-mode operation only after 2.14 m of the fiber with effective-mode area as large as  $2147 \mu\text{m}^2$  which makes our proposed design suitable for communication and high power applications.

### **1.3 Metamaterials**

Metamaterials are the artificially structured materials whose unprecedented properties could not be observed in the naturally occurring materials. In case of optical metamaterials, the basic



electromagnetic parameters i.e. electric permittivity and magnetic permeability are different from the natural optical materials. It was the long held belief that for the non-magnetic materials, magnetic permeability does not vary from one. However, in 1999, J. B. Pendry *et al.* introduced several artificial materials designed to provide a desired magnetic response at microwave and lower frequencies [34]. These structures consisted of arrays of wire loops producing an effective magnetic response even negative magnetic permeability in the GHz frequency range. Their work turned the theoretical work of V. G. Veselago [35] into reality. Following J. B. Pendry, many people worked on these artificial materials called metamaterials [35 - 50]. Now, it has become a hot topic due to its vast applications like perfect lensing, cloaking, light harvesting, perfect reflecting mirrors, nano-antennas, sensing, second-harmonic generation and other non-linear phenomenon [42 - 47].

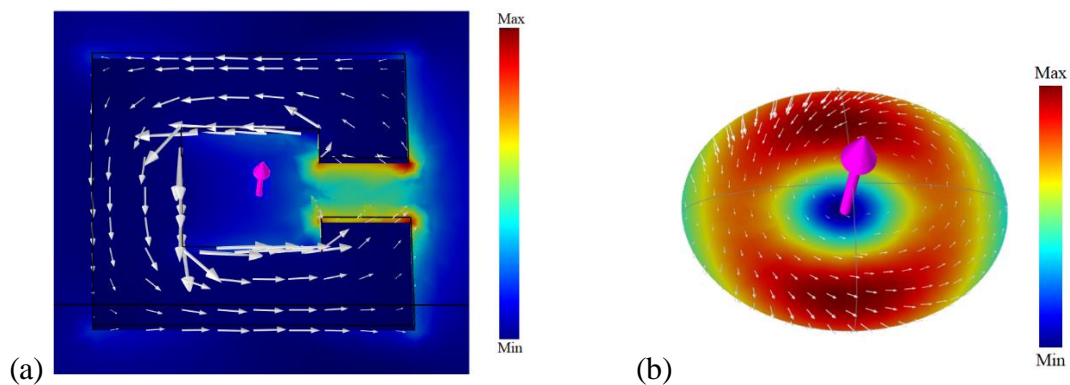


Figure 1.3. Electric field distribution in the (a) metallic split ring resonator and (b) high index dielectric resonator. White arrows represent the direction of electric field and purple arrow in the center represent the direction of magnetic field.

Metamaterials are the special kind of subwavelength resonators which are arranged in a periodic manner and whose electromagnetic properties are derived from the resonating elements in the same way as electromagnetic properties of conventional materials depend on the atoms or molecules [40]. Units of metamaterials are structured on a scale much shorter than their operating wavelength so that they can be considered as a homogeneous media for the

electromagnetic radiation of operating wavelength which is otherwise an inhomogeneous media.

On the basis of materials, there are three types of metamaterials as follows:

### **1.3.1 Metallic metamaterials**

In metallic metamaterials, split ring resonators (SRR) as shown in the figure 1.3 (a) are the mostly used metamaterials. SRR is considered to be the basic unit of metamaterial or usually called the magnetic meta-atom as it provides magnetic response due to inductance-capacitance (LC) resonance associated with it [36]. However, electric response can be easily obtained in most of the materials from radio frequencies to ultraviolet frequencies. But the SRR structure can operate only at lower frequencies in the range of GHz. SRR has been designed in the rectangular C-shape so that they can work in the visible region [37]. Some other efforts have also made to get magnetic response at 780 nm wavelength by making Fishnet structures [38]. But the radiative and non-radiative losses in the metals depreciate the properties of metamaterials especially at optical region.

### **1.3.2 Dielectric metamaterials**

An alternative approach to devise metamaterials, which evades metallic inclusions, is to employ materials with high dielectric constant which are called dielectric metamaterials [49 - 56]. A strong magnetic response can be obtained in such metamaterials even in the visible range which could not be possible using metals as shown in the figure 1.3 (b). M. Kerker *et al.* in 1983, explored unusual scattering effects by spheres composed of magnetic materials [54]. One of the significant findings was that backscattering by the magnetic sphere could be totally eliminated if electric permittivity of the magnetic sphere is equal to the magnetic permeability i.e.  $\epsilon = \mu$ . This effect can be attributed to the fact that the magnetic sphere supports overlapped

in-phase electric and magnetic moments of multipoles of same order and magnitude so that backscattered gain equals to zero. At that time this theory was useless due to the absence of magnetic sphere. However, the advent of magnetic meta-atom especially high dielectric meta-atoms have brought this theory into new realm [34, 53]. A new branch of nanophotonics which is termed as meta-optics has come into limelight which relies on optically induced magnetic responses. Huygens sources which are the overlapped electric and magnetic dipole resonances, could be now employed for designing optical antennas known as nanoantennas which are analogous to RF antennas but operating in the optical region [58, 59]. In this thesis, Kerker's conditions have been applied for the unidirectional scattering which is required in the nanoantennas.

Another approach to utilize dielectric meta-atoms for unidirectional scattering is to generate Fano resonance [60]. Fano resonance is an interference phenomenon between resonant and continuum states which gives rise to asymmetric profile in contrast to Lorentzian symmetric profile first discovered by Ugo Fano [61]. Fano dip has been obtained in the backward scattering due to the interference of electric and magnetic dipoles and quadrupoles and subsequently forward scattering could be enhanced at the same wavelength. This phenomenon leads to more directional scattering than the Kerker's type scattering as unidirectional scattering takes place at the wavelength of resonance. In this thesis, Fano resonance phenomenon has been applied for the enhancement of forward scattering for the nanoantenna applications.

### **1.3.3 Hybrid metal-dielectric metamaterials**

The metamaterials which utilize the resonance properties of metals as well as high refractive index dielectrics to explore various applications are called hybrid metamaterials. In this thesis, hybrid metamaterials have been employed to induce electromagnetically induced transparency (EIT). Electromagnetically induced transparency in the metamaterials refers to the interference

between the radiant and subradiant modes which makes the opaque medium transparent in a narrow frequency region [62]. Also, there occurs a steep change in the transmission phase within the transparency window which has potential applications in slow light devices, optical buffers, sensing and enhanced non-linear effects [62 - 65]. In this thesis, EIT has been employed for making optical buffers and sensors.

### **The main objectives of this thesis are**

1. To design and analyze special kind of optical fiber called photonic crystal fiber for single mode operation with large mode area for high power applications like fiber laser and amplifiers.
2. To design and analyze tunable lossless ellipsoidal dielectric metamaterial with highly directional scattering properties for nanoantenna applications.
3. To design and analyze core-shell ellipsoidal dielectric metamaterial for dual-band highly directional nanoantenna applications in the visible region.
4. To design and analyze cuboidal dielectric metamaterial nanoantenna with high directivity and radiation efficiency.
5. To design and analyze hybrid metal-dielectric metamaterial analogue of electromagnetically induced transparency for the application of optical buffers and sensors.

## **1.4 Overview of the thesis**

This thesis encompasses seven chapters in it with novel designs of photonic crystal fiber and metamaterials which are suitable for the applications like high power fiber laser, amplifiers, nanoantennas and sensing. The first chapter is the introduction which comprises the basic ideas and formulism on which the thesis work is based on.

In the chapter 2, a rectangular-core large mode area photonic crystal fiber structure has been proposed that offers extended single-mode operation by suppressing all the higher order modes to avoid the non-linear effects. In the proposed structure, there are four rectangular rings of air holes around the central silica core. The second ring of the structure has been modified by taking the down doped fused silica rods in place of the air holes. Confinement loss and effective-mode-area of FM (fundamental mode), FHOM (first higher order mode) and SHOM (second higher order) modes of the proposed PCF structure have been calculated. Variations in confinement loss and effective mode area have been analysed by changing different parameters of the fiber. The proposed PCF structure possesses effective-mode-area  $2147 \mu\text{m}^2$  at  $\lambda=1.064 \mu\text{m}$  with confinement losses of  $\sim 1.36 \times 10^{-2}$  dB/m and  $\sim 9.34$  dB/m for FM and FHOM respectively. At  $1.55 \mu\text{m}$ , the structure possesses the effective-mode-area of FM mode as large as  $5688 \mu\text{m}^2$  with the confinement losses of  $0.6$  dB/m and  $\sim 20.23$  dB/m for FM and FHOM respectively. Therefore, the proposed PCF structure can be used for the compact high power delivery devices such as high power fiber lasers and amplifiers.

In chapter 3, tri-axial ellipsoidal dielectric meta-atom has been employed for unidirectional scattering. Due to three-fold symmetry, ellipsoidal nanoparticle exhibits three types of resonant modes, one longitudinal mode and two transverse modes. In this chapter, tunable and azimuthally symmetric unidirectional scattering of ellipsoidal dielectric metamaterial has been analyzed. The dimensions of the nanoparticle are chosen in such a way that wavelength of forward scattering falls in the optical region. Electric and magnetic dipoles have been optically induced in the ellipsoidal dielectric nanoparticle. Generalized Kerker's condition has been applied where electric and magnetic dipoles spectrally meet. Due to the three types of longitudinal and transverse modes, complete forward unidirectional scattering takes place in the visible and near infrared region at three wavelengths  $680 \text{ nm}$ ,  $912 \text{ nm}$  and  $778 \text{ nm}$  just by changing the direction of incident electric field, satisfying the generalized Kerker's condition.

Thus, ellipsoidal nanoparticles can be used to achieve tunable unidirectional scattering. Tunable unidirectional properties exhibited by these nanoparticles can lead to a large number of applications for the development of low loss and ultra-compact optical nanoantennas, nanolasers, spectroscopy, high resolution near field microscopy, optical imaging and sensing.

In chapter 4, ellipsoidal core-shell metamaterial has been proposed for highly directional properties. In the proposed design, core is made up of Silicon and shell is made up of Silica. At the wavelength of magnetic resonance, Fano dip occurs in the backward scattering cross section and forward scattering enhancement takes place at the same wavelength so that there is an increment in the directivity. Effect on the directivity has been analyzed by changing the length of ellipsoidal nanoparticle along semi-axes. Two Fano resonances have been observed by decreasing the length of the nanoparticle along the semi-axis of electric polarization, where first and second Fano resonances are attributed to the dipole and quadrupole moments, respectively. These Fano resonant wavelengths in ellipsoidal nanoparticle exhibit higher directivity than the Kerker's type scattering or forward scattering shown by symmetrical structures like sphere. So, this core-shell metamaterial can act as an efficient directional nanoantenna.

In chapter 5, cuboidal silicon metamaterial has been proposed to achieve unidirectional enhanced forward scattering in contrast to symmetrical cubic nanoparticles. Both variants of cuboidal nanoparticles, i.e., nanodisk and nanorod type structures have been analyzed to get spectrally overlapping electric and magnetic dipole resonances. In the case of cuboidal nanodisk, electric and magnetic dipole resonances come closer by decreasing the height of the nanoparticle in the direction of polarization of the incident plane wave. At a particular height of cuboidal nanodisk, i.e., 50 nm, electric and magnetic resonances spectrally overlap and due to the broad electric and narrow magnetic dipole resonance, Fano dip takes place at the wavelength of 440 nm which results in enhanced forward scattering at that wavelength.

Forward and backward scattering have also been calculated at other heights of nanodisk, to show the difference. In the case of nanorod, height of the nanoparticle has been increased in the direction of propagation. At the height of 300 nm, electric and magnetic dipole resonances spectrally overlap and Fano resonance takes place at the wavelength of 520 nm. Forward scattering is enhanced and backward scattering is suppressed at this height of the nanorod. Moreover, optimized cuboidal nanodisk and nanorod metamaterials exhibit high value of radiation efficiency and directivity. Thus, these cuboidal nanodisk and nanorod act as highly directional nanoantennas.

In chapter 6, a hybrid metal-dielectric metamaterial structure has been proposed to get broadband polarization independent electromagnetically induced transparency in the terahertz region. Metal ring provides us electric dipole which act as bright mode while electric and magnetic dipoles of the dielectric cube excited at different frequencies serve as bright and quasi-dark modes. Electric dipole of the metal ring interferes with the electric as well as magnetic dipoles of the dielectric cube which creates an EIT window in a broad region from 1.8 THz to 2.2 THz. A steep and constant phase change in transmission results in high group delay of 5 ps in the broad EIT window so that a large delay bandwidth product equal to 2 could be obtained. Therefore, our proposed design has the potential applications in optical buffers and high transmission band pass filters. In addition to it, the interaction between bright mode of metal ring and quasi-dark mode of dielectric cube results into Fano dip at 1.75 THz with the quality factor of 89.5 and interaction of bright mode of metal ring and bright mode of dielectric cube results into another Fano dip at frequency of 2.25 THz with quality factor of 23. This has further been used to design a Fano resonance based sensor with sensitivities 25 GHz/RIU and 50 GHz/RIU and figure of merits 6 and 4 for the first and second resonance dips, respectively.

Chapter 7 includes summary of the thesis work and the future research scope by utilizing the current thesis work.

## References

- [1] VE Babicheva, N Kinsey, GV Naik, M Ferrera, AV Lavrinenko, VM Shalaev and A Boltasseva, “Towards CMOS-compatible nanophotonics: Ultra-compact modulators using alternative plasmonic materials” *Optics Express*, 21(22) (2013).
- [2] M Taghinejad and W Cai, “All-optical control of light in micro-and nanophotonics” *ACS Photonics*, 6(5) (2019).
- [3] O Yavas, M Svedendahl, P Dobosz, V Sanz and R Quidant, “On-a-chip biosensing based on all-dielectric nanoresonators” *Nano Letters*, 17(7) (2017).
- [4] X Ni, AV Kildishev and VM Shalaev, “Metasurface holograms for visible light” *Nature Communications*, 4(1) (2013).
- [5] K. Thyagarajan, , R.K.Varshney, P. Palai, A.K. Ghatak and I.C.Goyal, “A novel design of a dispersion compensating fiber” *IEEE Photonics Technology Letters*, 8(11), 1510-1512 (1996).
- [6] Y. Liu, J. Wang, Y. Li, R. Wang, J. Li and X. Xie, “A novel hybrid photonic crystal dispersion compensating fiber with multiple windows” *Optics and Laser Technology*, 44(7), 2076-2079 (2012).
- [7] L. F. Mollenauer, S. G. Evangelides and H. A. Haus, “Long-distance soliton propagation using lumped amplifiers and dispersion shifted fiber” *Journal of Lightwave Technology*, 9(2), 194-197 (1991).
- [8] K. F. Lee, J. Chen, C. Liang, X. Li, P.L. Voss and P. Kumar, “Generation of high-purity telecom-band entangled photon pairs in dispersion-shifted fiber” *Optics Letters*, 31(12), 1905-1907 (2006).
- [9] W. H. Reeves, D. V. Skryabin, F. Biancalana, J. C. Knight, P. St. J. Russell, F. G. Omenetto, A. Efimov, and A. J. Taylor, “Transformation and control of ultra-short pulses in dispersion-engineered photonic crystal fibers” *Nature* 424, 511–515 (2003).
- [10] F. Beltrán-Mejía, C. M. B. Cordeiro, P. André, and E. Silvestre, “Broadband dispersion compensation using inner cladding modes in photonic crystal fibers” *Optics Express*, 20, 3467–3472 (2012).
- [11] T. S. Saini, A. Kumar, and R. K. Sinha, “Triangular-core large mode area photonic crystal fiber with low bending loss for high power applications” *Applied Optics*, 53, 7246–7251 (2014).



- [12] K. Kishor, R. K. Sinha, and A. D. Varshney, “Experimental verification of improved effective index method for endlessly single mode photonic crystal fiber” *Optics and Lasers in Engineering*, 50, 182–186 (2012).
- [13] G. Jiang, Y. Fu, and Y. Huang, “High birefringence rectangular-hole photonic crystal fiber” *Optical Fiber Technology*, 26, 163–171 (2015).
- [14] J. Liao and J. Sun, “High birefringent rectangular lattice photonic crystal fibers with low confinement loss employing different sizes of elliptical air holes in the cladding and the core” *Optical Fiber Technology*, 18, 457–461 (2012).
- [15] I. Abdelaziz, H. Ademgil, F. Abdelmalek, S. Haxha, T. Gorman, and H. Bourchiha, “Design of a large effective mode area photonic crystal fiber with modified rings” *Optics Communications* 283, 5218–5223 (2010).
- [16] T. S. Saini, A. Kumar, and R. K. Sinha, “Broadband mid-IR supercontinuum generation in  $\text{As}_2\text{Se}_3$  based chalcogenide photonic crystal fiber: a new design and analysis,” *Optics Communications*, 347, 13–19 (2015).
- [17] T. S. Saini, A. Kumar, and R. K. Sinha, “Broadband mid-infrared supercontinuum spectra spanning 2–15  $\mu\text{m}$  using  $\text{As}_2\text{Se}_3$  chalcogenide glass triangular-core graded-index photonic crystal fiber” *Journal of Lightwave Technology*, 33, 3914–3920 (2015).
- [18] L. E. Hooper, P. J. Mosley, A. C. Muir, W. J. Wadsworth, and J. C. Knight, “Coherent supercontinuum generation in photonic crystal fiber with all-normal group velocity dispersion” *Optics Express* 19, 4902–4907 (2011).
- [19] J. Limpert, F. Röser, D. N. Schimpf, E. Seise, T. Eidam, S. Hädrich, J. Rothhardt, C. Jauregui, and A. Tünnermann, “High repetition rate gigawatt peak power fiber laser systems: challenges, design and experiment” *IEEE Journal of Selected Topics in Quantum Electronics*, 15, 159–169 (2009).
- [20] M. F. S. Ferreira, “Nonlinear effects in optical fibers: limitations and benefits” *Proceedings SPIE* 6793, 679302 (2008).
- [21] N. G. R. Broderick, H. L. Offerhause, D. J. Richardson, R. A. Sammut, J. E. Caplen, and L. Dong, “Large mode area fibers for high power applications” *Optical Fiber Technology*, 5, 185–196 (1999).
- [22] V. Rastogi and K. S. Chiang, “Leaky optical fiber for large mode area single mode operation” *Electronics Letters*, 39, 1110–1112 (2003).
- [23] A. Kumar and V. Rastogi, “Design and analysis of a multilayer cladding large-mode-area optical fiber” *Journal of Optics A: Pure and Applied Optics*, 10, 015303 (2008).

- [24] A. Kumar, V. Rastogi, C. Kakkar, and B. Dussardier, “Co-axial dualcore resonant leaky fibre for optical amplifiers” *Journal of Optics A: Pure and Applied Optics*, 10, 115306 (2008).
- [25] B. Dussardier, V. Rastogi, A. Kumar, and G. Monnom, “Largemode-area leaky optical fiber fabricated by MCVD” *Applied Optics*, 50, 3118–3122 (2011).
- [26] J. Limpert, T. Schreiber, S. Nolte, H. Zellmer, A. Tünnermann, R. Iliew, F. Lederer, J. Broeng, G. Vienn, A. Petersson, and C. Jakobsen, “High-power air-clad large-mode-area photonic crystal fiber laser” *Optics Express*, 11, 818–823 (2003).
- [27] Y. Tsuchida, K. Saitoh, and M. Koshiba, “Design of single-mode holey fibers with large-mode-area and low bending losses: the significance of the ring-core region” *Optics Express*, 15, 1794–1802 (2007).
- [28] H. Ademgil and S. Haxha, “Bending insensitive large mode area photonic crystal fiber” *Optik*, 122, 1950–1956 (2011).
- [29] M. Napierala, E. B. Pawlik, T. Nasilowski, P. Mergo, F. Berghmans and H. Thienpont, “Photonic crystal fiber with large mode area and characteristic bending properties” *IEEE Photonics Technology Letters*, 24, 1409–1411 (2012).
- [30] H. Ademgil and S. Haxha, “Endlessly single mode photonic crystal fiber with improved effective mode area” *Optics Communications*, 285, 1514–1518 (2012).
- [31] T. S. Saini, A. Kumar, V. Rastogi, and R. K. Sinha, “Selectively filled large-mode-area photonic crystal fiber for high power applications” *Proceedings SPIE 8847*, 88471Q (2013).
- [32] J. Li, J. Wang, Y. Cheng, R. Wang, B. Zhang, and H. Wang, “Novel large mode area photonic crystal fibers material-filled structure” *Optics and Laser Technology*, 48, 375–380 (2013).
- [33] G. Gu, F. Kong, T. W. Hawkins, M. Jones, and L. Dong, “Extending mode areas of single-mode all-solid photonic bandgap fibers” *Optics Express*, 23, 9147–9156 (2015).
- [34] J. B. Pendry, A. J. Holden, D. J. Robbins and W. J. Stewart, “Magnetism from conductors and enhanced nonlinear phenomena” *IEEE Transactions on Microwave Theory and Techniques*, 47(11), 2075-2084 (1999).
- [35] V. G. Veselago, “Electrodynamics of substances with simultaneously negative  $\epsilon$  and  $\mu$ ” *Uspekhi Fizicheskikh Nauk*, 92, 517 (1967).
- [36] D. R. Smith, W. J. Padilla, D. C. Vier, S. C. Nemat-Nasser, and S. Schultz, “Composite medium with simultaneously negative permeability and permittivity” *Physical Review Letters*, 84, 4184–4187 (2000).

- [37] B. Lahiri, S. G. McMeekin, A. Z. Khokhar, M. Richard and N. P. Johnson, “Magnetic response of split ring resonators (SRRs) at visible frequencies” *Optics Express*, 18(3), 3210-3218 (2010).
- [38] G. Dolling, M. Wegener, C. M. Soukoulis and S. Linden, “Negative-index metamaterial at 780 nm wavelength” *Optics Letters*, 32(1), 53–55 (2007).
- [39] V. M. Shalaev, “Optical negative-index metamaterials” *Nature Photonics*, 1, 41–48 (2007).
- [40] S. A. Ramakrishna, “Physics of negative refractive index materials” *Reports on Progress in Physics*, 68, 449–521 (2005).
- [41] B. Popa and S. A. Cummer, “Compact Dielectric Particles as a Building Block for Low-Loss Magnetic Metamaterials” *Physical Review Letters*, 100, 207401 (2008).
- [42] J. B. Pendry, “Negative refraction makes a perfect lens” *Physical Review Letters*, 85(18), 3966 (2000).
- [43] A. O. Bak, E. O. Yoxall, P. Sarriugarte, V. Giannini, S.A. Maier, R. Hillenbrand, J.B. Pendry and C.C. Phillips, “Harnessing a quantum design approach for making low-loss superlenses” *Nano Letters*, 16 (3), 1609-1613 (2016).
- [44] K. Lindfors, D. Dregely, M. Lippitz, N. Engheta, M. Totzeck and H. Giessen, “Imaging and steering unidirectional emission from nanoantenna array metasurfaces” *ACS Photonics* 3 (2), 286-292 (2016).
- [45] J. Yan, M. Churong, L. Pu, W. Chengxin and Y. Guowei, “Electrically controlled scattering in a hybrid dielectric-plasmonic nanoantenna” *Nano Letters*, 17 (8), 4793-4800 (2017).
- [46] Y. Jin, “Engineering plasmonic gold nanostructures and metamaterials for biosensing and nanomedicine” *Advanced Materials*, 24 (38) 5153-5165 (2012).
- [47] D. Lee, H. Jeong and S. Lim, “Electronically switchable broadband metamaterial absorber” *Scientific Reports*, 7 (1) 4891 (2017).
- [48] W. Cai, U. K. Chettiar, A. V. Kildishev and V. M. Shalaev, “Optical cloaking with metamaterials” *Nature Photonics*, 1 (4) 224-227 (2007).
- [49] S. Zhang, W. Fan, K. J. Malloy and S. R. J. Brueck, “Near-infrared double negative metamaterials” *Optics Express*, 13(13), 4922 (2005).
- [50] S. Jahani and Z. Jacob, “All-dielectric metamaterials” *Nature Nanotech.* 11, (2016).
- [51] Q. Zhao, J. Zhou, F. Zhang, D. Lippens, “Mie resonance-based dielectric metamaterials” *Materials Today*, 12(12) (2009).

- [52] Z. Ma, S. M. Hanham, P. Albella, B. Ng, H. T. Lu, Y. Gong, S. A. Maier, and M. Hong, “Terahertz All-Dielectric Magnetic Mirror Metasurfaces” *ACS Photonics*, 3, 1010–1018 (2016).
- [53] A. I. Kuznetsov, A. E. Miroschnichenko, Y. H. Fu, J. B. Zhang and B. Luk’yanchuk, “Magnetic light” *Scientific Reports*, 2, 492 (2012).
- [54] M. Kerker, D.-S. Wang and C. L. Giles “Electromagnetic scattering by magnetic spheres” *Journal of Optical Society of America*, 73(6), (1983).
- [55] W Liu and Y. S. Kivshar, “Generalized Kerker effects in nanophotonics and meta-optics [Invited]” *Optics Express*, 26(10) (2018).
- [56] A. B. Evlyukhin, S. M. Novikov, U. Zywietz, R. L. Eriksen, C. Reinhardt, S. I. Bozhevolnyi and B. N. Chichkov, “Demonstration of Magnetic Dipole Resonances of Dielectric Nanospheres in the Visible Region” *Nano Letters*, 12, 3749–3755 (2012).
- [57] Y. Tsuchimoto, T. Yano, T. Hayashi, and M. Hara, “Fano resonant all-dielectric core/shell nanoparticles with ultrahigh scattering directionality in the visible region” *Optics Express*, 24(13), (2016).
- [58] M. Decker, I. Staude, M. Falkner, J. Dominguez, D.N. Neshev, I. Brener, T. Pertsch, and Y. S. Kivshar, “High-efficiency dielectric Huygens’ surfaces” *Advanced Optical Materials*, 3(6), 813-820 (2015).
- [59] J. M. Geffrin, B. García-Cámara, R. Gómez-Medina, P. Albella, L.S.Froufe-Pérez, C. Eyraud, A. Litman, R. Vaillon, F. González, M. Nieto-Vesperinas and J. J. Sáenz, “Magnetic and electric coherence in forward-and back-scattered electromagnetic waves by a single dielectric subwavelength sphere” *Nature Communications*, 3(1), 1-8 (2012).
- [60] Y. Tsuchimoto, T. A. Yano, T. Hayashi and M. Hara, “Fano resonant all-dielectric core/shell nanoparticles with ultrahigh scattering directionality in the visible region” *Optics Express*, 24(13), 14451-14462, (2016).
- [61] U. Fano, “Effects of configuration interaction on intensities and phase shifts” *Physical Review*, 124(6), 1866 (1961).
- [62] M. Fleischhauer, A. Imamoglu and J. P. Marangos, “Electromagnetically induced transparency: Optics in coherent media” *Reviews of Modern Physics*, 77(2), 633, (2005).
- [63] B. Tang, L. Dai, and C. Jiang, “Electromagnetically induced transparency in hybrid plasmonic-dielectric system” *Optics Express*, 19(2), 628-637 (2011).
- [64] H. M. Li, S. B. Liu, S. Y. Liu, S. Y. Wang, H. F. Zhang, B. R. Bian and X. K. Kong, “Electromagnetically induced transparency with large delay-bandwidth product

induced by magnetic resonance near field coupling to electric resonance” *Applied Physics Letters*, 106(11), 114101 (2015).

- [65] T. Ma, Q. Huang, H. He, Y. Zhao, X. Lin and Y. Lu, “All-dielectric metamaterial analogue of electromagnetically induced transparency and its sensing application in terahertz range” *Optics Express*, 27(12), (2019) 16624-16634.



# **CHAPTER-2**





---

## CHAPTER-2

---

### RECTANGULAR-CORE LARGE-MODE-AREA PHOTONIC CRYSTAL FIBER FOR HIGH POWER APPLICATIONS \*

---

#### 2.1 Introduction

Photonic crystal fibers have drawn a lot of attention due to their unique properties like large mode area despite single mode operation, dispersion tailoring, super continuum generation, high birefringence and so on [1 - 10]. All these properties could not be achieved using conventional optical fibers. PCF is the kind of speciality optical fiber with a periodic array of air holes in its cladding region running along its length. Such fibers guide light due to center defect created at a design stage. Among all the attributes of PCFs, large-mode-area is the most important because it supports high transmission in the fiber lasers and amplifiers [11, 12]. LMA fiber enables high power levels to be transmitted through the optical fiber by mitigating the non-linear effects. However, LMA fibers have the limitation that fiber becomes multimoded which causes modal dispersion.

---

\* **Reena**, T. S. Saini, A. Kumar, Y. Kalra, and R. K. Sinha, "Rectangular-core large-mode-area photonic crystal fiber for high power applications: design and analysis," *Journal of Applied Optics*, 55 (15), 4095 – 4100 (2016).

---

Various techniques have been adopted in the literature to suppress the higher order modes like designing graded index cladding, alternative high and low index cladding, co-axial cores with leaky cladding and leaky mode filtering using modified chemical vapour deposition technique [13 - 16]. However, the extended single mode operation is impossible in conventional LMA fiber. Therefore, large mode area photonic crystal fibers are the good alternative for single mode operation.

LMA PCFs with single mode operation has been employed with different design approaches of air holes in the cladding region. A high power air-clad microstructure has been demonstrated by designing ytterbium-doped photonic crystal fiber laser with mode field area  $350 \mu\text{m}^2$  of propagating mode [17]. A LMA PCF with single-mode operation and low bending loss has been designed for high power delivery applications [18]. To reduce the confinement and bending losses, silica photonic crystal fiber with doped center core has been designed with different level of doping concentration around the core region [19]. For enlarging the loss of higher order modes at bending of the PCF, two additional missing air holes are inserted in the cladding region [20]. Endlessly single-mode photonic crystal fiber has been designed with improved effective-mode-area based on introducing higher index material in the cladding region [21]. Novel large-mode-area photonic crystal fiber structure have been designed based on selectively material-filled technology [22, 23]. Photonic band gap fiber having single-mode operation with multiple cladding has been designed with very large mode area of  $\sim 2650 \mu\text{m}^2$  at  $1.064 \mu\text{m}$  wavelength [24].

In this chapter, a rectangular-core large mode area photonic crystal fiber structure has been designed which offers extended single-mode operation by suppressing all higher order modes. The PCF is designed in such a way that initially it supports several leaky modes, out of which only fundamental mode survives after a finite propagation length. A 20 dB confinement loss

to the first higher order modes ensure the effective single-mode operation. Simulated results show that the confinement loss of first higher order mode at  $\lambda=1.064 \mu\text{m}$  is 9.34 dB/m, therefore proposed PCF structure supports effective single-mode operation only after 2.14 m length of the fiber, with effective mode area as large as  $2147 \mu\text{m}^2$ , which can mitigate nonlinear effects effectively.

## 2.2 Design parameters of RC LMA PCF

The transverse cross-sectional view of proposed RC LMA PCF design has been shown in Figure 2.1. In the proposed design, rectangular array of air holes has been drawn in the fused silica along the length of the fiber. One air hole has been removed from the center to make a core. There have been four rectangular rings of air holes around the central core. The second ring of the structure has been modified by taking the down doped fused silica rods in place of the air holes. The rods, in the second ring, have the diameter of  $d_1$ . The diameter of the air holes in the first, third and fourth rings is taken as  $d_2$ . Distance between the centers of two adjoining air holes, i.e. pitch has been taken as a constant value  $A$ . A circular perfectly matched layer (PML) has been implemented around the cladding of the fiber to avoid the unnecessary reflections.

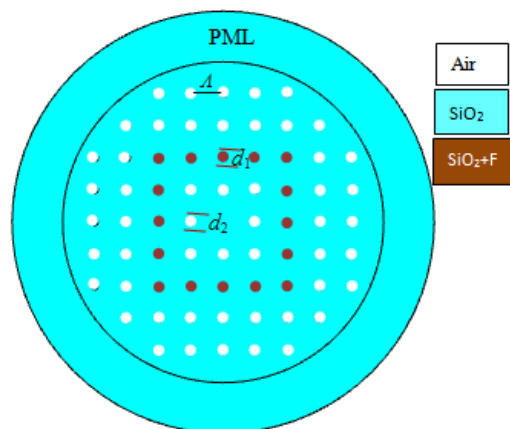


Figure 2.1 Transverse view of rectangular core large mode area photonic crystal fiber

## 2.3 Formulation and method of analysis

The propagation constant of the PCF structure is complex. The real part of the propagation constant corresponds to the effective index of the mode and imaginary part corresponds to the confinement loss of the propagating mode. The confinement loss can be calculated using the imaginary part of modes by the following relation

$$L \left[ \frac{dB}{m} \right] = \frac{40\pi}{\ln(10)\lambda} \text{Im}(n_{eff}) = 8.686k_0 \text{Im}(n_{eff}) \quad (2.1)$$

where,  $\text{Im}(n_{eff})$  is the imaginary part of the effective mode index of that mode and  $\lambda$  is the operating wavelength of light in meter.

The effective mode area of the mode of the proposed LMA PCF has been calculated using the following equation

$$A_{eff} = \frac{(\iint |E|^2 dx dy)^2}{\iint |E|^4 dx dy} \quad (2.2)$$

where,  $E$  is the amplitude of the transverse electric field propagating through the fiber. The effective indices and the confinement losses of the modes are calculated using finite element based commercially available software 'COMSOL Multiphysics' based on full vectorial finite element method.

## 2.4 Numerical results and discussion

In the proposed structure, the effective mode index, confinement loss and effective-mode-area has been investigated. The refractive index of fused silica has been taken as 1.45 at 1.064  $\mu\text{m}$ . For this structure, the confinement losses of the modes increase on increasing mode order. To

confirm this, in our study, we have investigated first three modes i.e. fundamental mode (FM), First higher order mode (FHOM) and the second higher order mode (SHOM).

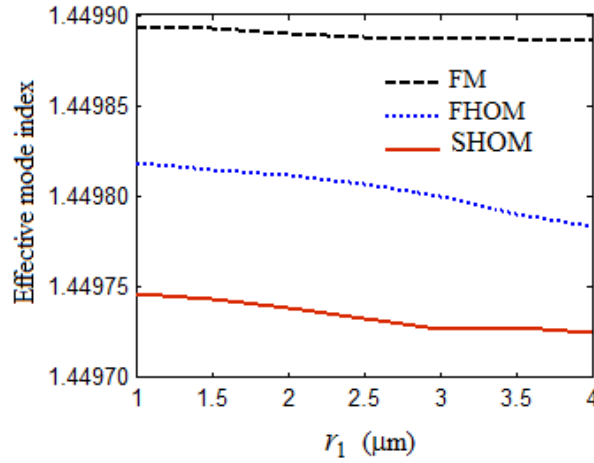


Figure 2.2 Variation of the effective mode indices of FM, FHOM and SHOM with  $r_1$  while keeping other parameters fixed as  $n_f = 1.435$ ,  $r_2 = 2 \mu\text{m}$ ,  $A = 19 \mu\text{m}$  and  $\lambda = 1.064 \mu\text{m}$ .

Initially, we have chosen the structural parameters as  $r_2 = 2 \mu\text{m}$ ,  $A = 19 \mu\text{m}$  and  $n_f = 1.435$  and then we observed the effect of  $r_1$ . As illustrated in Figure 2.2, the effective mode indices of the FM, FHOM and SHOM decrease with  $r_1$ . This is due to the increment in air filling fraction of structure on increasing  $r_1$ . It is also clear from the figure that the effective index of the FM is always larger than that of the FHOM and SHOM.

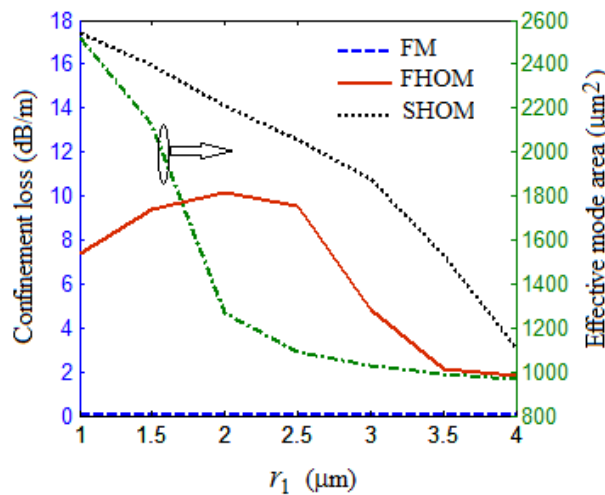


Figure 2.3 Variation of the effective-mode-area of FM and the confinement losses of FM, FHOM and SHOM modes with  $r_1$  while keeping other parameters fixed,  $n_f = 1.435$ ,  $r_2 = 2 \mu\text{m}$ ,  $A = 19 \mu\text{m}$  and  $\lambda = 1.064 \mu\text{m}$ .

Variation of confinement loss and effective-mode-area of FM, FHOM and SHOM modes of the proposed PCF structure have been shown in the figure 2.3. Initially, the confinement loss of FHOM increases up to  $r_1 = 2 \mu\text{m}$  and then start to decrease. This is due to the resonance effect of FHOM to the cladding in this range of  $r_1$ . Due to resonance effect of FHOM at  $r_1 = 2 \mu\text{m}$ , the design introduces the confinement loss of  $\sim 10.18 \text{ dB/m}$ , however, the FM offer very small confinement loss at this value of  $r_1$  with effective mode area of  $1269 \mu\text{m}^2$ . The confinement loss of the SHOM is always larger than that of the FHOM. The effective-mode-area of FM decreased on increasing  $r_1$ , which is quite obvious. The index contrast between core and cladding increases on increasing  $r_1$ . Therefore, there is more and more enhancement in guidance of FM, leading to reduction in effective-mode-area. In order to achieve the maximum allowed mode-area for FM with maximum possible confinement loss to FHOM, we have chosen  $r_1 = 1.5 \mu\text{m}$ . At this value of  $r_1$ , the confinement losses of FM and FHOM are  $1.36 \times 10^{-2} \text{ dB/m}$  and  $9.34 \text{ dB/m}$  respectively. Thus design can work as single-mode PCF with a very large mode-area of  $\sim 2147 \mu\text{m}^2$ .

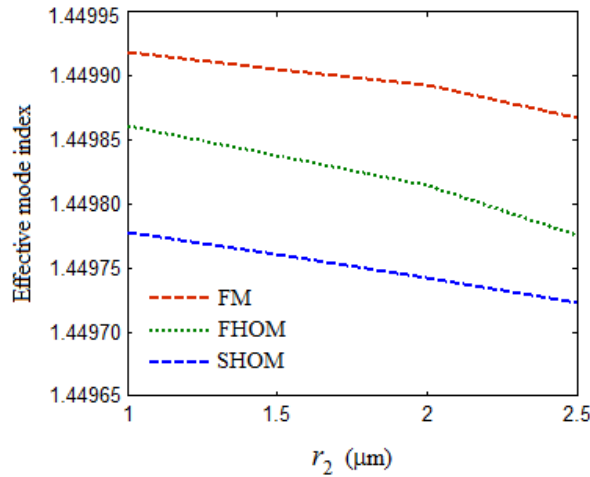


Figure 2.4 Variation of effective mode indices of FM, FHOM and SHOM with  $r_2$  while keeping other parameters fixed as:  $n_f = 1.435$ ,  $r_1 = 1.5 \mu\text{m}$ ,  $A = 19 \mu\text{m}$ , and  $\lambda = 1.064 \mu\text{m}$ .

The effect of  $r_2$  on effective mode indices of the FM, FHOM and SHOM has been illustrated in figure 2.4. The effective mode indices of the modes decrease slowly with  $r_2$ . The variation of confinement losses of FM, FHOM and SHOM modes and the effective-mode-area of FM

mode with  $r_2$  have been revealed in Figure 2.5. The confinement loss of FHOM mode is  $\sim 8$  dB/m for  $1 \mu\text{m} < r_2 < 2.5 \mu\text{m}$ . The effective-mode-area of the FM decreases with  $r_2$ . This is because of the larger confinement of the FM in the cladding. The confinement loss of FHOM is  $\sim 9.34$  dB/m around  $r_2 = 2 \mu\text{m}$  and the effective-mode-area of FM is  $2147 \mu\text{m}^2$  which makes the fiber suitable for high power applications.

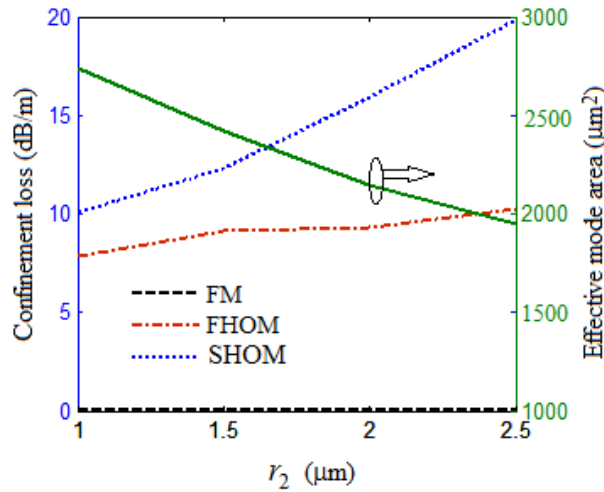


Figure 2.5 Variation of effective-mode-area of FM and the confinement losses of FM, FHOM and SHOM modes with  $r_2$  while keeping other parameters fixed as:  $n_f = 1.435$ ,  $r_1 = 1.5 \mu\text{m}$ ,  $A = 19 \mu\text{m}$ , and  $\lambda = 1.064 \mu\text{m}$ .

We can observe from Figure 2.6 that the effective mode index of FHOM and SHOM is almost independent of the increase in the refractive index of fluorine doped rods in second ring. While small increment in the effective mode index of FM can be observed on increasing  $n_f$ .

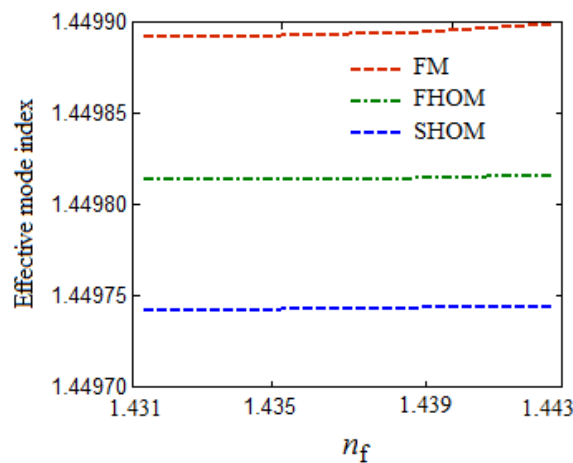


Figure 2.6 Variation of effective mode indices of FM, FHOM and SHOM modes with refractive index of fluorine doped rods while keeping other parameter fixed as:  $r_1 = 1.5 \mu\text{m}$ ,  $r_2 = 2 \mu\text{m}$ ,  $A = 19 \mu\text{m}$ , and  $\lambda = 1.064 \mu\text{m}$ .

The dependence of confinement losses of FM, FHOM and SHOM and effective-mode-area of FM with  $n_f$  has been depicted in figure 2.7. The confinement loss of FM is always very small while, the loss of the FHOM decreases slowly on increasing the  $n_f$ . Although, the effective-mode-area of FM is larger at larger values of  $n_f$ , but the confinement loss of FHOM becomes  $< \sim 8$  dB/m which can lead to propagation of higher order modes. Therefore, for single-mode operation the value of  $n_f$  should be less than 1.44. The confinement of the SHOM is always very large.

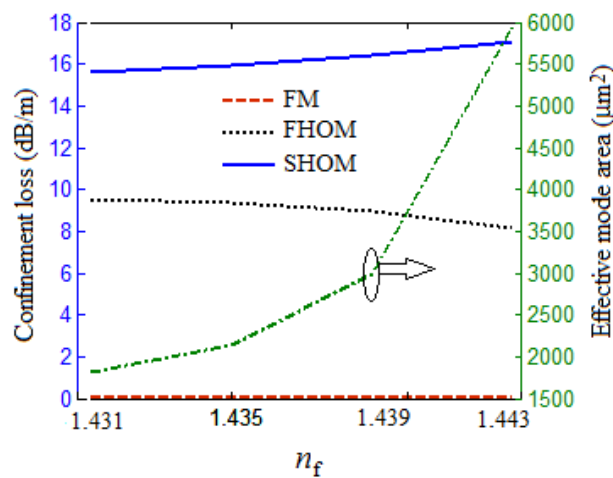


Figure 2.7 Variation of effective-mode-area of FM and the confinement loss of FM, FHOM and SHOM modes with refractive index of fluorine doped rods while keeping other parameter fixed as:  $r_1 = 1.5 \mu\text{m}$ ,  $r_2 = 2 \mu\text{m}$ ,  $A = 19 \mu\text{m}$  and  $\lambda = 1.064 \mu\text{m}$ .

The variation of confinement losses of FM, FHOM and SHOM modes and the effective-mode-area of FM with the pitch of the structure has been illustrated in figure 2.8. On increasing the value of the pitch the effective mode area of FM mode increasing but at higher value of pitch the loss of the all the modes decreases which leads to the confinement of the higher order modes within the PCF structure. At pitch  $A = 19 \mu\text{m}$ , the PCF structure offers the effective mode area as large as  $2147 \mu\text{m}^2$  with very low confinement loss of  $1.36 \times 10^{-2}$  dB/m. The confinement loss of the FHOM is 9.34 dB/m at pitch =  $19 \mu\text{m}$ . Therefore, fiber will offer the effective single mode operation after 2.14 m propagation length of the PCF.



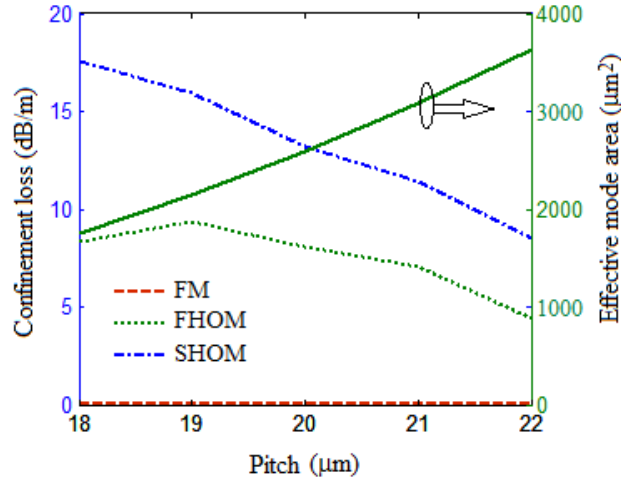


Figure 2.8. Variation of effective mode area of FM and the confinement loss of FM, FHOM and SHOM with pitch while keeping other parameter fixed as:  $n_f = 1.435$ ,  $r_1 = 1.5 \mu\text{m}$ ,  $r_2 = 2 \mu\text{m}$ ,  $\lambda = 1.064$ .

Figure 2.9 illustrates the variation of confinement losses of FM, FHOM and SHOM modes and effective-mode-area of FM with wavelength ranging from  $0.9 \mu\text{m}$  to  $1.6 \mu\text{m}$ . The confinement losses of all the three modes and the effective-mode-area of FM increase with increase in wavelength due to spreading of the field in the leaky cladding region at higher wavelengths. At  $\lambda = 1.064 \mu\text{m}$ , the confinement loss of FM is as low as  $\sim 1.36 \times 10^{-2}$  dB/m with effective-mode-area as large as  $2147 \mu\text{m}^2$  and the confinement loss of FHOM is as high as  $\sim 9.34$  dB/m. On the other hand, at  $\lambda = 1.55 \mu\text{m}$ , the confinement loss of FM is as low as  $\sim 0.6$  dB/m with effective-mode-area of FM as large as  $\sim 5688 \mu\text{m}^2$  and the confinement loss of FHOM is as high as  $20.23$  dB/m.

The maximum confinement loss of FM is  $\sim 0.7$  dB/m at  $1.6 \mu\text{m}$ . The minimum confinement loss of FHOM is  $\sim 8$  dB/m at  $1 \mu\text{m}$ . Therefore, a  $\sim 2.5$  m long PCF is suitable to offer extended effective single-mode operation in the spectral range of  $1.0 - 1.6 \mu\text{m}$ .

The contour plots of FHOM and FM have been shown in Figure 2.10 for  $\lambda = 1.064 \mu\text{m}$ ,  $r_1 = 1.5 \mu\text{m}$ ,  $r_2 = 2 \mu\text{m}$ ,  $A = 19 \mu\text{m}$  and  $n_f = 1.435$ . It can be observed that the FHOM is leaking towards the cladding region while, the FM is well confined within the core of the PCF structure.

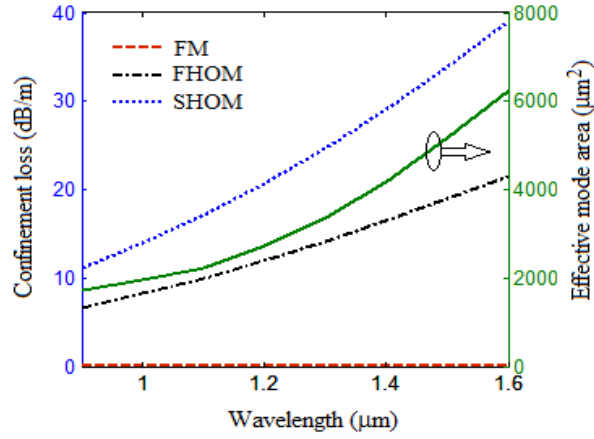


Figure 2.9. Variation of effective mode area of FM and the confinement loss of FM, FHOM and SHOM with wavelength while keeping other parameter fixed as:  $n_f=1.435$ ,  $r_1=1.5 \mu\text{m}$ ,  $r_2=2 \mu\text{m}$ , and  $A=19 \mu\text{m}$ .

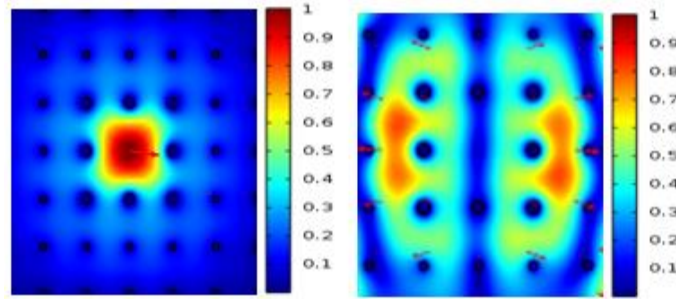


Figure 2.10. Contour plot of the normalized electric field intensity of FM and FHOM modes at optimized parameters as:  $n_f=1.435$ ,  $r_1=1.5 \mu\text{m}$ ,  $r_2=2 \mu\text{m}$ ,  $A=19 \mu\text{m}$ , and  $\lambda=1.064 \mu\text{m}$ .

## 2.5 Conclusion

In conclusion, we can articulate that by choosing proper structural and the refractive index of the material rods one can tune the confinement losses of FM and FHOM modes of the proposed RC PCF structure. The proposed PCF structure possesses effective-mode-area as large as  $2147 \mu\text{m}^2$  at  $\lambda=1.064 \mu\text{m}$  with confinement losses of  $\sim 1.36 \times 10^{-2} \text{ dB/m}$  and  $\sim 9.34 \text{ dB/m}$  for FM and FHOM respectively. Therefore, after propagating 2.14 m length the loss of FHOM exceeds 20 dB and FM mode is only propagating mode at  $1.064 \mu\text{m}$ . At  $1.55 \mu\text{m}$ , the structure possesses the effective-mode-area of FM mode as large as  $5688 \mu\text{m}^2$  with the confinement losses of  $0.6 \text{ dB/m}$  and  $\sim 20.23 \text{ dB/m}$  for FM and FHOM respectively. After travelling approximately 1 m distance through the PCF, the FHOM suffers by more than 20 dB loss while FM offers only

0.6 dB loss. Therefore, only 1 m long PCF is sufficient to obtain effective single-mode operation at 1.55  $\mu\text{m}$ . Our proposed RC-PCF design offers effective-mode-area larger than that of the earlier reported in other triangular core and hexagonal geometries [3, 23]. Such large-mode-area PCF structure is able to eliminate all the unwanted nonlinear effects. Based on these mentioned numerical results and analysis we can say that the proposed PCF structure can be used for high power applications such as high power fiber lasers, amplifiers and sensors.

## References

- [1] W. H. Reeves, D. V. Skryabin, F. Biancalana, J. C. Knight, P. St. J. Russell, F. G. Omenetto, A. Efimov and A. J. Taylor, “Transformation and control of ultra-short pulses in dispersion-engineered photonic crystal fibers” *Nature*, 424, 511–515 (2003).
- [2] F. Beltrán-Mejía, C. M. B. Cordeiro, P. André and E. Silvestre, “Broadband dispersion compensation using inner cladding modes in photonic crystal fibers” *Optics Express*, 20, 3467–3472 (2012).
- [3] T. S. Saini, A. Kumar and R. K. Sinha, “Triangular-core large mode area photonic crystal fiber with low bending loss for high power applications” *Applied Optics*, 53, 7246–7251 (2014).
- [4] K. Kishor, R. K. Sinha and A. D. Varshney, “Experimental verification of improved effective index method for endlessly single mode photonic crystal fiber” *Optics and Lasers in Engineering*, 50, 182–186 (2012).
- [5] G. Jiang, Y. Fu and Y. Huang, “High birefringence rectangular-hole photonic crystal fiber” *Optical Fiber Technology*, 26, 163–171 (2015).
- [6] J. Liao and J. Sun, “High birefringent rectangular lattice photonic crystal fibers with low confinement loss employing different sizes of elliptical air holes in the cladding and the core” *Optical Fiber Technology*, 18, 457–461 (2012).
- [7] I. Abdelaziz, H. Ademgil, F. Abdelmalek, S. Haxha, T. Gorman and H. Bouchiha, “Design of a large effective mode area photonic crystal fiber with modified rings” *Optics Communications*, 283, 5218–5223 (2010).
- [8] T. S. Saini, A. Kumar and R. K. Sinha, “Broadband mid-IR supercontinuum generation in As<sub>2</sub>Se<sub>3</sub> based chalcogenide photonic crystal fiber: a new design and analysis” *Optics Communications*, 347, 13–19 (2015).
- [9] T. S. Saini, A. Kumar and R. K. Sinha, “Broadband mid-infrared supercontinuum spectra spanning 2–15  $\mu\text{m}$  using As<sub>2</sub>Se<sub>3</sub> chalcogenide glass triangular-core graded-index photonic crystal fiber” *Journal of Lightwave Technology*, 33, 3914–3920 (2015).
- [10] L. E. Hooper, P. J. Mosley, A. C. Muir, W. J. Wadsworth and J. C. Knight, “Coherent supercontinuum generation in photonic crystal fiber with all-normal group velocity dispersion” *Optics Express*, 19, 4902–4907 (2011).
- [11] S. K. Varshney, K. Saitoh, M. Koshiba, B. P. Pal and R. K. Sinha, “Design of S-band erbium doped concentric dual core photonic crystal fiber amplifiers with ASE suppression,” *Journal of Lightwave Technology*, 27, 1725–1733 (2009).

- [12] K. Wen, H. Peng, J. Wang, R. Wang, and J. H. Li, "Finite element analysis of a novel weak pressure sensor based on fiber Bragg grating in photonic crystal fibers," *Optical Engineering*, 48, 034402 (2009).
- [13] V. Rastogi and K. S. Chiang, "Leaky optical fiber for large mode area single mode operation" *Electronics Letters*, 39, 1110–1112 (2003).
- [14] A. Kumar and V. Rastogi, "Design and analysis of a multilayer cladding large-mode-area optical fiber" *Journal of Optics A: Pure and Applied Optics*, 10, 015303 (2008).
- [15] A. Kumar, V. Rastogi, C. Kakkar, and B. Dussardier, "Co-axial dualcore resonant leaky fibre for optical amplifiers" *Journal of Optics A: Pure and Applied Optics*, 10, 115306 (2008).
- [16] B. Dussardier, V. Rastogi, A. Kumar, and G. Monnom, "Largemode-area leaky optical fiber fabricated by MCVD" *Applied Optics*, 50, 3118–3122 (2011).
- [17] J. Limpert, T. Schreiber, S. Nolte, H. Zellmer, A. Tünnermann, R. Iliew, F. Lederer, J. Broeng, G. Vienn, A. Petersson, and C. Jakobsen, "High-power air-clad large-mode-area photonic crystal fiber laser" *Optics Express*, 11, 818–823 (2003).
- [18] Y. Tsuchida, K. Saitoh, and M. Koshiba, "Design of single-mode holey fibers with large-mode-area and low bending losses: the significance of the ring-core region" *Optics Express*, 15, 1794–1802 (2007).
- [19] H. Ademgil and S. Haxha, "Bending insensitive large mode area photonic crystal fiber" *Optik*, 122, 1950–1956 (2011).
- [20] M. Napierala, E. B. Pawlik, T. Nasilowski, P. Mergo, F. Berghmans and H. Thienpont, "Photonic crystal fiber with large mode area and characteristic bending properties" *IEEE Photonics Technology Letters*, 24, 1409–1411 (2012).
- [21] H. Ademgil and S. Haxha, "Endlessly single mode photonic crystal fiber with improved effective mode area" *Optics Communications*, 285, 1514–1518 (2012).
- [22] T. S. Saini, A. Kumar, V. Rastogi, and R. K. Sinha, "Selectively filled large-mode-area photonic crystal fiber for high power applications" *Proceedings SPIE 8847*, 88471Q (2013).
- [23] J. Li, J. Wang, Y. Cheng, R. Wang, B. Zhang, and H. Wang, "Novel large mode area photonic crystal fibers material-filled structure" *Optical Laser Technology*, 48, 375–380 (2013).
- [24] G. Gu, F. Kong, T. W. Hawkins, M. Jones, and L. Dong, "Extending mode areas of single-mode all-solid photonic bandgap fibers" *Optics Express*, 23, 9147–9156 (2015).



# **CHAPTER-3**





---

## CHAPTER-3

---

### TUNABLE UNIDIRECTIONAL SCATTERING OF ELLIPSOIDAL DIELECTRIC META-ATOM \*

---

#### 3.1 Introduction

In the previous chapter, large mode area photonic crystal fiber has been designed which is a speciality optical fiber and can be used for single mode operation in high power applications and communication. In this chapter, dielectric meta-atom, which is a basic constituent unit of metamaterials has been utilized for unidirectional scattering in the optical region which is useful in the design and development of tunable, low-loss and ultra-compact nanoantennas. Metamaterials are the special type of artificially structured materials unlike conventional optical materials, whose electromagnetic properties do not depend on the material composition i.e. atoms or molecules but depend on its basic constituent units, meta-atoms [1 - 4]. Due to which they show unusual and unprecedented electromagnetic properties like negative refraction, diffraction-free lensing, unidirectional scattering and object cloaking [1 - 33].

---

\* **Reena**, Y. Kalra, A. Kumar, and R. K. Sinha, "Tunable unidirectional scattering of ellipsoidal single nanoparticle," *Journal of Applied Physics*, 119, 234102 (2016).

---

Magnetic response of ordinary non-magnetic materials towards electromagnetic field is very small because magnetic permeability of the non-magnetic materials is unity. However, metallic split ring resonators (SRR) display not only magnetic response even they are able to achieve negative magnetic permeability [4 - 6, 8 -13]. This is the reason behind that metallic SRR is also called magnetic meta-atom. But the SRR can operate only at lower frequencies in the range of GHz. Although different approaches have been adopted to get the magnetic response at the higher frequencies like SRR has been designed in the rectangular C-shape, by making Fishnet structures and by taking paired metallic paired nanorods etc. [4, 9 - 15]. However, metal's losses and absorption at the higher frequencies affect the quality of the metallic nanostructure. Therefore, large permittivity dielectrics are being used as the alternative of metals due to negligible absorption [23 - 33]. A strong magnetic response can be obtained in such metamaterials even in the visible range which could not be possible using metals. First of all, Kuznetsov et al. demonstrated experimentally magnetic resonance in the visible spectrum region using high-dielectric nanoparticles [27]. Due to the light-matter interaction, electric and magnetic dipoles are produced in the dielectric nanoparticles of large permittivity at resonant frequencies. Therefore, they are called the dielectric meta-atoms as they show electric as well as magnetic response even in the visible region.

Scattering properties of light by various types of nanoparticles have been studied to manipulate and confine electromagnetic waves on the nanometer scale due to their numerous applications such as sensing, nanoantennas, photovoltaics and medicine [34 - 38]. M. Kerker *et al.* studied scattering effects by spheres composed of magnetic materials [28]. In their study they found that backscattering by the magnetic sphere could be totally eliminated if electric permittivity of the magnetic sphere is equal to the magnetic permeability i.e.  $\epsilon = \mu$ . However, there was no physical significance of this theory due to the absence of magnetic sphere. But this theory came into light after the discovery of magnetic meta-atom especially high dielectric

meta-atoms. Huygens sources which are the overlapped electric and magnetic dipole resonances, could now be employed for designing optical antennas known as nanoantennas which are analogous to RF antennas but operating in the optical region [32, 33, 39].

In this chapter, Kerker's conditions have been applied for the unidirectional scattering which is required in the highly directional nanoantennas. The wavelength at which first generalized Kerker's condition is satisfied, forward scattering takes place by suppressing the backward scattering to zero and the wavelength at which second generalized Kerker's condition is satisfied, most of the light is scattered in the backward direction [39 - 41]. Unidirectional forward scattering (Huygen's source) and backward scattering (Huygen's reflector) are used to design all-dielectric optical nanoantennas [33]. Complete forward scattering and high directivity has been achieved in many symmetrical structures like sphere and cube [37, 39]. Fu et al. have calculated forward to backward scattering ratio for spheroidal Si nanoparticles [42]. In spheroidal nanoparticle, two axes are equal and only one axis has different dimensions. But ellipsoidal nanoparticle has all the axes unequal. Ellipsoidal nanoparticle has the advantage that it has three-fold symmetry which leads to three types of modes, two transverse modes (TM) and one longitudinal mode (LM). Polarizability of the nanoparticle changes by changing the direction of incident electric field along three unequal axes of the ellipsoid. Hence, the forward scattering can be tuned at different wavelengths by changing the direction of incident electric field, which is not possible in case of symmetric structures like sphere and cube. Kalkbrenner et al. experimentally demonstrated the rotation of the single gold ellipsoidal nanoparticle attached to the tip of glass fiber [43]. Eventually, it is also feasible to rotate dielectric nanoparticle using this technique, so that it is useful in various nanophotonic applications like nanoantennas, optical imaging and energy harvesting.

### 3.2 Design parameters of the meta-atom

Triaxial ellipsoidal dielectric nonmagnetic nanoparticle has been considered with lengths of semi-principal axes as 'a', 'b' and 'c', where length along 'a' has been taken as semi-major axis. Ellipsoidal particles are classified into three categories based on the relative length of the three principal axes namely oblate spheroids ( $a = b > c$ ), prolate spheroids ( $a = b < c$ ) and scalene ellipsoids ( $a > b > c$ ). In this chapter, scalene ellipsoid has been considered which leads to three distinct modes, one longitudinal mode and two transverse modes. The effective radius of the equivolume sphere for the ellipsoidal nanoparticle is given by  $r_{\text{eff}} = (a * b * c)^{1/3}$ .

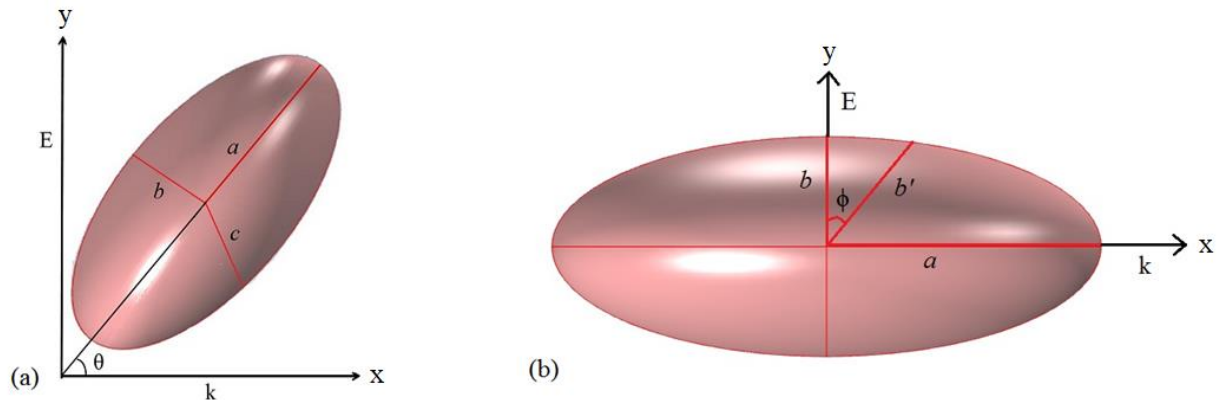


Figure 3.1 (a) Orientation of the major-axis of the ellipsoidal nanoparticle in the laboratory frame around the x-axis or the direction of propagation k with angle  $\theta$ . (b) Rotation of the nanoparticle around the major-axis with angle  $\phi$ .

Material of the nanoparticle has been taken to be Ge which has high permittivity,  $\epsilon_r = 20$ , required for the design of low loss high dielectric nanoantennas [44]. Dimensions of ellipsoid have been taken as  $a = 125$  nm,  $b = 100$  nm and  $c = 50$  nm. The dimensions of the nanoparticle are chosen in such a way that wavelength of forward scattering falls in the optical region. Incident radiation has been taken to be linearly polarized in the y-direction and propagates in the x-direction. Orientation of the nanoparticle has been shown in figure 3.1 (a) and rotation of the nanoparticle when major axis is parallel to the x-axis has been shown in figure 3.1 (b).

### 3.3 Dipole analysis

Due to the light-matter interaction, electric and magnetic dipoles are generated at the particular wavelengths  $\lambda_{ED}$  and  $\lambda_{MD}$ . The electric dipole moment  $\mathbf{p}$  and magnetic dipole moment  $\mathbf{m}$  can be expressed as

$$\mathbf{p} = \varepsilon_0(1 - \varepsilon_r) \int_V \mathbf{E}(\mathbf{r}') dV' \quad (3.1)$$

$$\mathbf{m} = \frac{i\omega\varepsilon_0(1 - \varepsilon_r)}{2c} \int_V \mathbf{r} \times \mathbf{E}(\mathbf{r}') dV' \quad (3.2)$$

where,  $i$  denotes the imaginary part of the complex variable,  $\omega$  is the angular frequency,  $\varepsilon_0$  is the vacuum permittivity,  $\mathbf{r}$  is the observation point,  $\mathbf{r}'$  is the source point,  $c$  is the speed of light in vacuum and  $\varepsilon_r$  is the relative permittivity of the nanoparticle,  $\times$  denotes the vector product of position vector  $\mathbf{r}$  and electric field vector  $\mathbf{E}(\mathbf{r})$ . Calculations have been done in the vectorial field with the finite element method (FEM) based commercial software ‘Comsol Multiphysics’.

Now scattering cross section of the nanoparticle for both electric and magnetic dipoles has been calculated as

$$\sigma_{sca}^p = \frac{P_{sca,ED}}{I_0} \quad (3.3)$$

$$\sigma_{sca}^m = \frac{P_{sca,MD}}{I_0} \quad (3.4)$$

where,  $I_0$  is the incident power density,  $P_{sca,ED}$  and  $P_{sca,MD}$  are the power scattered by electric and magnetic dipole respectively which can be expressed as

$$P_{sca,ED} = \frac{c^2 k_0^4 z_0}{12\pi} |\mathbf{p}|^2 \quad (3.5)$$

$$P_{sca,MD} = \frac{c^2 k_0^4 z_0}{12\pi} |\mathbf{m}|^2 \quad (3.6)$$

where,  $c$  is the speed of light in vacuum,  $k_0$  and  $z_0$  are the free space wavenumber and free space impedance, respectively. Electric dipole moment ' $\mathbf{p}$ ' and magnetic dipole moment ' $\mathbf{m}$ ' have been calculated using the equations (3.1) and (3.2), respectively.

Further, the effect of orientation and rotation of the ellipsoidal nanoparticle on electric and magnetic dipole moments has been analyzed. Three distinct modes, one longitudinal mode (LM) and two transverse modes (TM) are excited at distinct combinations of incident angle and rotation angle. LM mode is excited when major axis is parallel to the incident electric field (E) or at  $\theta = 90^\circ$ . Two TM modes are excited when major axis is perpendicular to the incident electric field or at  $\theta = 0^\circ$ . One TM mode is excited when  $\phi = 0^\circ$  or  $b$ -axis is parallel to the incident electric field and another transverse mode is excited when  $\phi = 90^\circ$  or  $c$ -axis is parallel to the incident electric field.

Scattering cross section has been calculated using the equations (3.3) and (3.4). The variation of scattering cross-section of the ellipsoidal nanoparticle with wavelength for the incident electric field parallel to  $a$ -axis has been obtained as shown in figure 3.2 (a). Peaks in the scattering cross section, one at the wavelength 500 nm corresponds to electric dipole resonance and another at 650 nm corresponds to the magnetic dipole resonance as shown in figure 3.2 (a). Electric field distribution in the nanoparticle at the wavelengths  $\lambda_{ED} = 500$  nm and  $\lambda_{MD} = 650$  nm has been shown in figures 3.2 (b) and 3.2 (c) respectively. So, at  $\theta = 90^\circ$ , LM has been excited at the wavelengths  $\lambda_{ED}$  and  $\lambda_{MD}$ . Figure 3.2 (a) indicates that electric dipole and magnetic dipoles interfere at the wavelengths 607 nm and 680 nm. At these wavelengths electric and magnetic responses are equal.

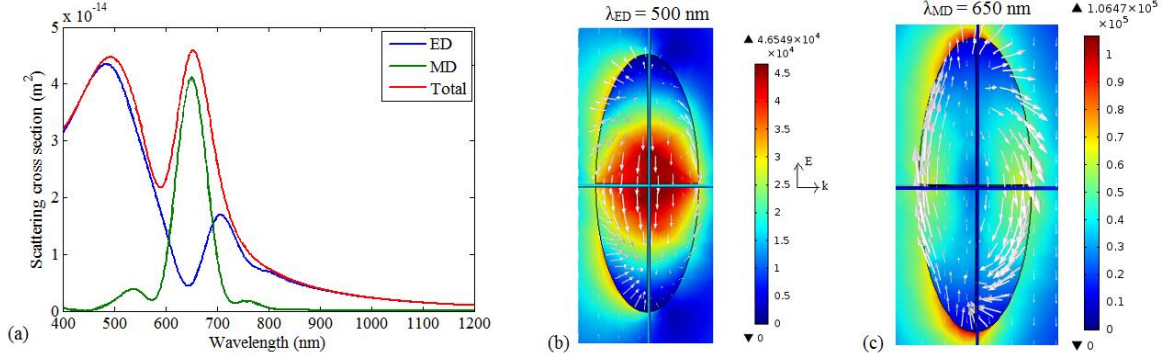


Figure 3.2 (a) Scattering cross-section of the ellipsoidal nanoparticle when  $E \parallel a$ -axis of the ellipsoid (b) - (c) Electric field inside the nanoparticle forming electric dipole and magnetic dipole. White arrows indicate electric lines of force.

Further, angle of orientation has been changed from  $\theta = 90^\circ$  to  $\theta = 0^\circ$ , major axis is now parallel to the direction of propagation and two minor axes have been taken to be parallel to the incident electric field one by one. Then two transverse modes are excited, one is called  $b$ -TM when  $\phi = 0^\circ$  and another is called  $c$ -TM when  $\phi = 90^\circ$ .

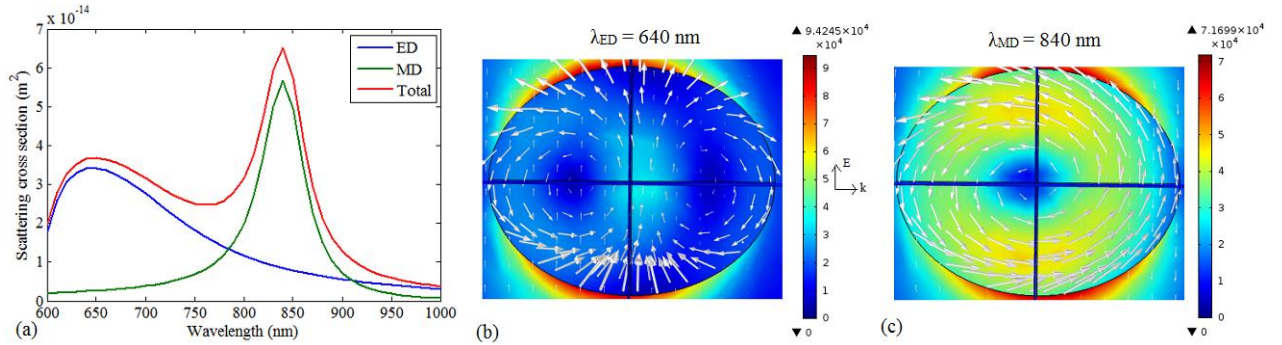


Figure 3.3 (a) Variation of scattering cross-section with wavelength when  $E \parallel b$ -axis of the ellipsoid (b) - (c) Electric field distribution patterns at the wavelengths where electric and dipoles are created.

First,  $b$ -axis has been taken to be parallel to the incident electric field, so  $b$ -TM mode has been excited. Scattering cross section has been calculated and has been plotted versus wavelength as shown in figure 3.3 (a). Peaks in the scattering spectra denote the electric and magnetic dipole resonances. Electric dipole and magnetic dipole are created at the wavelengths  $\lambda_{ED} = 640$  nm and  $\lambda_{MD} = 840$  nm, respectively as shown in the figure 3.3 (a). The electric field

distribution at  $\lambda_{ED} = 640$  nm and  $\lambda_{MD} = 840$  nm has been shown in the figures 3.3 (b) and 3.3 (c), respectively.

Now,  $c$ -axis has been taken to be parallel to the incident electric field, leading to the excitation of  $c$ -TM mode. The position of the electric dipole and magnetic dipole has been shifted to the wavelengths  $\lambda_{ED} = 560$  nm and  $\lambda_{MD} = 660$  nm as shown in figure 3.4(a). An electric field distribution at the wavelengths  $\lambda_{ED}$  and  $\lambda_{MD}$  has been shown in figures 3.4(b) and 3.4(c), respectively.

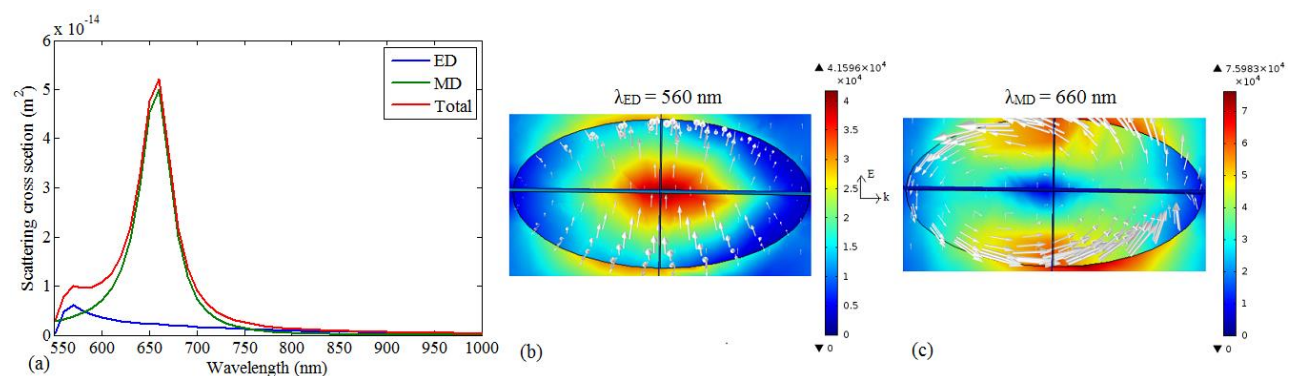


Figure 3.4 (a) Plot of scattering cross section with wavelength when  $E \parallel c$ -axis of the ellipsoidal nanoparticle. (b) - (c) Electric field distribution and direction of electric field shown by white lines.

Hence, electric and magnetic dipoles can be tuned at different wavelengths by changing the direction of the incident electric field.

### 3.4 Generalized Kerker's condition

Far field scattering pattern of pure electric and magnetic dipoles is symmetrically distributed in forward and backward directions, when there is no interference between the dipoles. In the case of interference of electric dipole and magnetic dipole, unidirectional scattering takes place. Positions of electric dipoles, magnetic dipoles and their interference have been shown in the figures 3.2 – 3.4 for longitudinal as well as transverse modes. Further, to discriminate whether there is forward scattering or backward scattering, electric polarizability and magnetic



polarizability has been calculated and generalized Kerker's conditions have been applied [40, 41]. Electric polarizability  $\alpha_e$  and magnetic polarizability  $\alpha_m$  can be expressed as

$$\alpha_e = \alpha_{ee}^{yy} = \frac{p_y}{\epsilon_0 |E_0|} \quad (3.7)$$

$$\alpha_m = \alpha_{ee}^{xx} = \frac{m_x}{|H_0|} \quad (3.8)$$

where,  $E_0$  and  $H_0$  are the electric and magnetic fields of the incident plane wave fallen on the nanoparticle,  $p_y$  and  $m_x$  are the electric dipole moment along  $y$ -axis and magnetic dipole moment along  $x$ -axis respectively.

According to first GK condition, unidirectional forward scattering takes place, when

$$\frac{\alpha_e}{\epsilon_s} = \mu_s \alpha_m \quad (3.9)$$

which results in backward scattering zero or

$$\frac{d\sigma_{sca}}{d\Omega}(180^\circ) = 0 \quad (3.10)$$

where,  $\epsilon_s$  and  $\mu_s$  are the relative permittivity and permeability of the surrounding medium. In our case, surrounding medium is air, so  $\epsilon_s = \mu_s = 1$ .

Further, according to second GK condition, backward scattering takes place when

$$\text{Re}\left(\frac{\alpha_e}{\epsilon_s}\right) = -\text{Re}(\mu_s \alpha_m) \quad (3.11)$$

$$\text{Im}\left(\frac{\alpha_e}{\epsilon_s}\right) = \text{Im}(\mu_s \alpha_m) \quad (3.12)$$

Forward scattering is not zero in this case and has a value equal to

$$\frac{d\sigma_{sca}}{d\Omega}(0^\circ) = \frac{16k_0^{10}}{9} |\alpha_e / \epsilon_s|^4 \quad (3.13)$$

In this case, as medium is taken to be air, so  $\epsilon_s = \mu_s = 1$ , so that real part of the electric polarizability is equal to negative of the real part of the magnetic polarizability as shown in equation (3.11). Also, imaginary parts of the electric and magnetic polarizabilities are equal as shown in equation (3.12). In case of backward scattering there is a very small lobe in the forward direction. Thus, forward scattering is not completely suppressed in this case, value of scattered intensity in the forward direction is given by the equation (3.13).

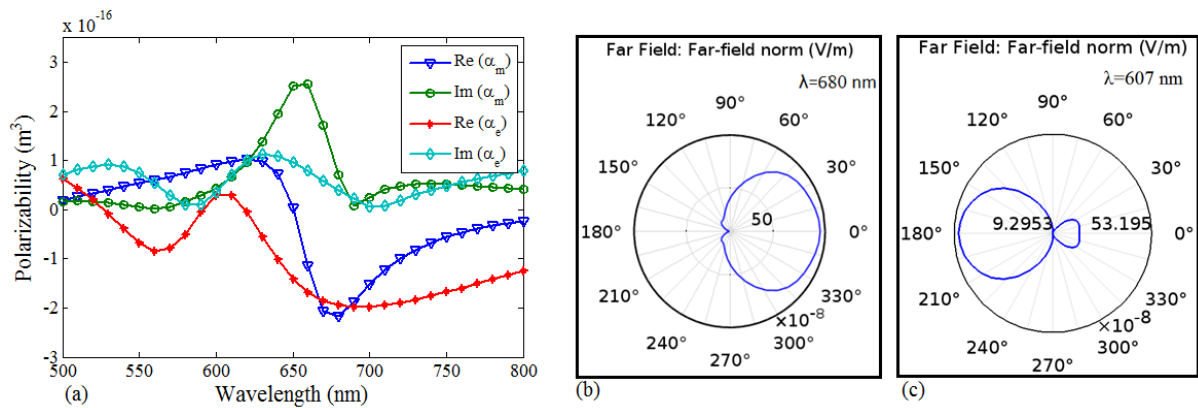


Figure 3.5 (a) Plot of real and imaginary parts of electric and magnetic polarizabilities of the nanoparticle with wavelength when  $E \parallel a$ -axis. (b) - (c) Far field scattering patterns show forward scattering at wavelength 680 nm and backward scattering at 607 nm.

Now, real and imaginary parts of the electric and magnetic polarizabilities of the nanoparticle have been calculated using equations (3.7) and (3.8) and variations have been plotted with respect to the wavelength for all the three distinct modes to analyze the GK conditions of forward scattering and backward scattering as shown in figures 3.5 (a) – 3.7 (a). Real and imaginary parts of electric and magnetic polarizabilities have been plotted in the figure 3.5 (a) for the longitudinal mode when incident electric field is parallel to the  $a$ -axis or semi-major axis. First generalized Kerker's condition is satisfied at the wavelength 680 nm leading to forward scattering at 680 nm. Far field scattering pattern is shown in figure 3.5 (b). At this wavelength, no backward scattering has been obtained, further verified this fact. At the wavelength 607 nm, second GK condition is satisfied, thus backward scattering takes place

with a small lobe in the forward direction. Far field scattering pattern at this wavelength is shown in figure 3.5 (c).

Further, electric and magnetic polarizabilities have been calculated for the transverse mode when incident electric field is along the  $b$ -axis of the nanoparticle. Here, real and imaginary parts of electric and magnetic polarizabilities are equal at 912 nm as shown in figure 3.6 (a). Hence, first GK condition is satisfied at this wavelength. Far-field scattering pattern at this wavelength indicates forward scattering shown in figure 3.6 (b). Second GK condition is satisfied at the wavelength 784 nm. So, there is backward scattering at this wavelength which is also shown by far field scattering pattern in the figure 3.6 (c).

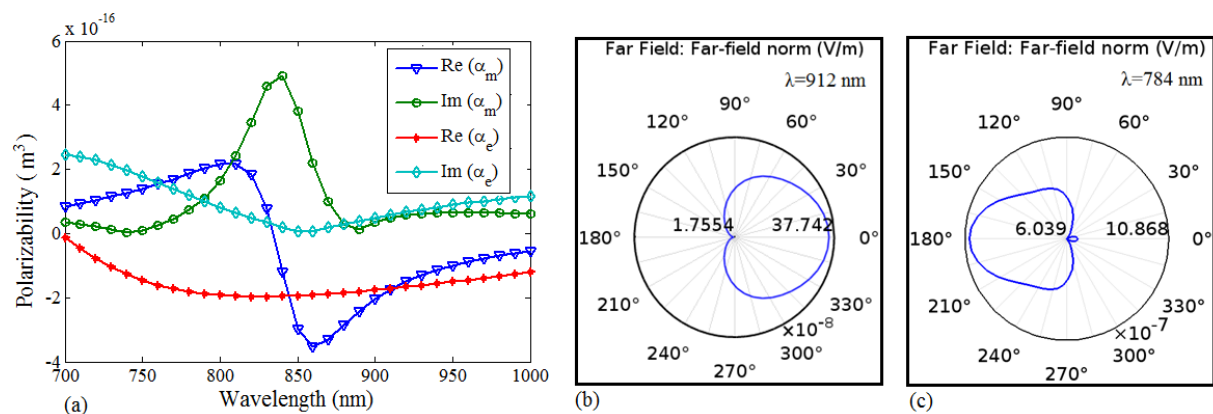


Figure 3.6 (a) Variation of electric and magnetic polarizabilities of the nanoparticle with wavelength when  $E \parallel b$ -axis. (b) - (c) Far field scattering patterns show forward scattering at wavelength 912 nm and backward scattering at 784 nm.

Finally, polarizabilities have been calculated and plotted versus wavelength in the figure 3.7 (a) for the second transverse mode in which incident electric field has been taken along  $c$ -axis i.e. smallest axis of the nanoparticle. In this case, first generalized condition is satisfied at the wavelength  $\lambda = 778 \text{ nm}$ . Hence, at this wavelength scattering takes place in forward direction which is also verified by far field scattering pattern in the figure 3.7 (b) and backward scattering takes place at the wavelength 585 nm as shown in the figure 3.7 (c), where far field scattering patterns has been calculated using finite element method. Thereby, ellipsoidal nanoparticles are the suitable candidates for tunable unidirectional applications.

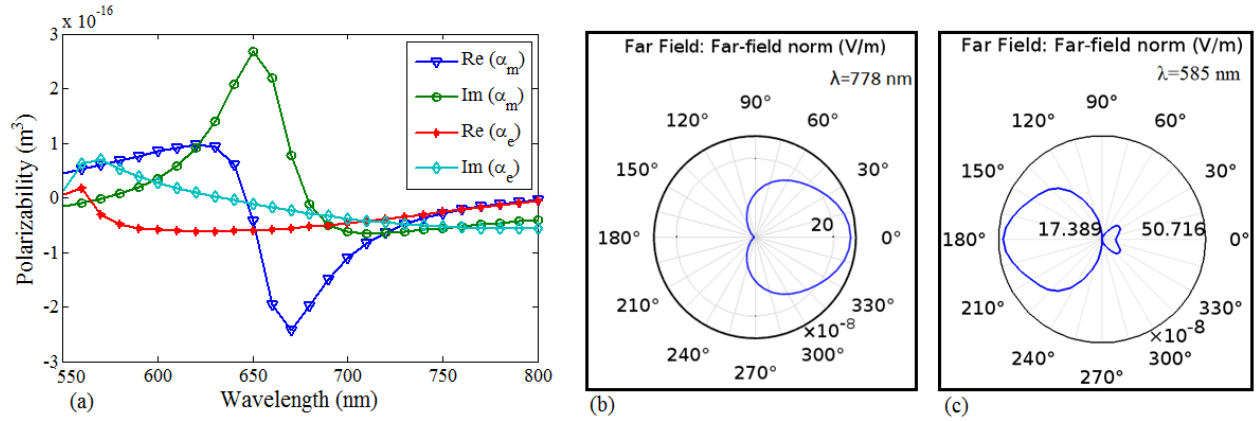


Figure 3.7 (a) Wavelength dependence of real and imaginary parts of electric and magnetic polarizabilities of the nanoparticle when  $E \parallel c$ -axis. (b) - (c) Far field scattering patterns show forward scattering at wavelength 778 nm and backward scattering at 585 nm.

### 3.5 Conclusion

In this chapter, tunable and azimuthally symmetric unidirectional scattering of ellipsoidal dielectric meta-atom has been analyzed. Electric and magnetic dipoles have been optically induced in the ellipsoidal nanoparticle at the resonance wavelengths, where peaks of the scattering spectra denote the positions of resonance. Due to three-fold symmetry, ellipsoidal nanoparticle exhibits three types of resonant modes, one longitudinal mode and two transverse modes. Due to the three types of longitudinal and transverse modes, complete forward unidirectional scattering takes place in the visible and near infrared region at three wavelengths 680 nm, 912 nm and 778 nm just by changing the direction of incident electric field, satisfying the generalized Kerker's condition. Thus, ellipsoidal nanoparticles can be used to achieve tunable unidirectional scattering. Tunable unidirectional properties exhibited by these nanoparticles can lead to a large number of applications for the development of low loss and ultra-compact optical nanoantennas, nanolasers, spectroscopy, high resolution near field microscopy, optical imaging and sensing.

## References

- [1] F. Monticone and A. Alu. “Metamaterial, plasmonic and nanophotonic devices” *Reports on Progress in Physics*, 80(3), 036401 (2017).
- [2] S. Mühlig, C. Menzel, C. Rockstuhl and F. Lederer, “Multipole analysis of meta-atoms” *Metamaterials*, 5(2-3), 64-73 (2011).
- [3] C. Rockstuhl, C. Menzel, S. Mühlig, J. Petschulat, C. Helgert, C. Etrich, A. Chipouline, T. Pertsch and F. Lederer, “Scattering properties of meta-atoms” *Physical Review B*, 83(24), 245119 (2011).
- [4] C. Enkrich, M. Wegener, S. Linden, S. Burger, L. Zschiedrich, F. Schmidt, J. F. Zhou, T. Koschny and C. M. Soukoulis, “Magnetic metamaterials at telecommunication and visible frequencies” *Physical Review letters*, 95(20), 203901 (2005).
- [5] S. A. Ramakrishna, “Physics of negative refractive index materials” *Reports on Progress in Physics*, 68, 449–521 (2005).
- [6] J. B. Pendry, A. J. Holden, D. J. Robbins and W. J. Stewart, “Magnetism from conductors and enhanced nonlinear phenomena” *IEEE Transactions on Microwave Theory and Techniques*, 47(11), 2075-2084 (1999).
- [7] V. G. Veselago, “Electrodynamics of substances with simultaneously negative  $\epsilon$  and  $\mu$ ” *Uspekhi Fizicheskikh Nauk*, 92, 517 (1967).
- [8] D. R. Smith, W. J. Padilla, D. C. Vier, S. C. Nemat-Nasser, and S. Schultz, “Composite medium with simultaneously negative permeability and permittivity” *Physical Review Letters*, 84, 4184–4187 (2000).
- [9] B. Lahiri, S. G. McMeekin, A. Z. Khokhar, M. Richard and N. P. Johnson, “Magnetic response of split ring resonators (SRRs) at visible frequencies” *Optics Express*, 18(3), 3210-3218 (2010).
- [10] C. Rockstuhl, T. Zentgraf, H. Guo, N. Liu, C. Etrich, I. Loa, K. Syassen, J. Kuhl, F. Lederer and H. Giessen, “Resonances of split-ring resonator metamaterials in the near infrared” *Applied Physics B*, 84(1), 219-227, (2006).
- [11] S. Linden, C. Enkrich, M. Wegener, J. Zhou, T. Koschny and C. M. Soukoulis, “Magnetic response of metamaterials at 100 terahertz” *Science*, 306(5700), 1351-1353, (2004).
- [12] G. Dolling, M. Wegener, C. M. Soukoulis, and S. Linden, “Negative-index metamaterial at 780 nm wavelength” *Optics Letters*, 32(1), 53–55 (2007).

- [13] W. J. Padilla, A. J. Taylor, C. Highstrete, M. Lee, and R. D. Averitt, “Dynamical electric and magnetic metamaterial response at terahertz frequencies” *Physical Review letters*, 96(10), 107401 (2006).
- [14] V. M. Shalaev, “Optical negative-index metamaterials” *Nature Photonics*, 1, 41–48 (2007).
- [15] S. Zhang, W. Fan, K. J. Malloy and S. R. J. Brueck, “Near-infrared double negative metamaterials” *Optics Express*, 13(13), 4922 (2005).
- [16] J. B. Pendry, “Negative refraction makes a perfect lens” *Physical Review letters*, 85(18), 3966 (2000).
- [17] A. O. Bak, E. O. Yoxall, P. Sarriugarte, V. Giannini, S.A. Maier, R. Hillenbrand, J.B. Pendry and C.C. Phillips, “Harnessing a quantum design approach for making low-loss superlenses” *Nano Letters*, 16 (3), 1609-1613 (2016).
- [18] K. Lindfors, D. Dregely, M. Lippitz, N. Engheta, M. Totzeck and H. Giessen, “Imaging and steering unidirectional emission from nanoantenna array metasurfaces” *ACS Photonics*, 3 (2), 286-292 (2016).
- [19] J. Yan, M. Churong, L. Pu, W. Chengxin and Y. Guowei, “Electrically controlled scattering in a hybrid dielectric-plasmonic nanoantenna” *Nano Letters*, 17 (8), 4793-4800 (2017).
- [20] Y. Jin, “Engineering plasmonic gold nanostructures and metamaterials for biosensing and nanomedicine” *Advanced Materials*, 24 (38) 5153-5165 (2012).
- [21] D. Lee, H. Jeong and S. Lim, “Electronically switchable broadband metamaterial absorber” *Scientific Reports*, 7 (1) 4891 (2017).
- [22] W. Cai, U. K. Chettiar, A. V. Kildishev and V. M. Shalaev, “Optical cloaking with metamaterials” *Nature Photonics*, 1 (4) 224-227 (2007).
- [23] B. Popa and S. A. Cummer, “Compact Dielectric Particles as a Building Block for Low-Loss Magnetic Metamaterials” *Physical Review Letters*, 100, 207401 (2008).
- [24] S. Jahani and Z. Jacob, “All-dielectric metamaterial” *Nature Nanotechnology*, 11, (2016).
- [25] Q. Zhao, J. Zhou, F. Zhang, D. Lippens, “Mie resonance-based dielectric metamaterials” *Materials Today*, 12(12) (2009).
- [26] Z. Ma, S. M. Hanham, P. Albella, B. Ng, H. T. Lu, Y. Gong, S. A. Maier, and M. Hong, “Terahertz All-Dielectric Magnetic Mirror Metasurfaces” *ACS Photonics*, 3, 1010–1018 (2016).

- [27] A. I. Kuznetsov, A. E. Miroshnichenko, Y. H. Fu, J. B. Zhang and B. Luk'yanchuk, "Magnetic light" *Scientific Reports*, 2, 492 (2012).
- [28] M. Kerker, D.-S. Wang and C. L. Giles "Electromagnetic scattering by magnetic spheres" *Journal of Optical Society of America*, 73(6), (1983).
- [29] W Liu and Y. S. Kivshar, "Generalized Kerker effects in nanophotonics and meta-optics [Invited]" *Optics Express*, 26(10), (2018).
- [30] A. B. Evlyukhin, S. M. Novikov, U. Zywietz, R. L. Eriksen, C. Reinhardt, S. I. Bozhevolnyi and B. N. Chichkov, "Demonstration of Magnetic Dipole Resonances of Dielectric Nanospheres in the Visible Region" *Nano Letters*, 12, 3749–3755 (2012).
- [31] Y. Tsuchimoto, T. Yano, T. Hayashi, and M. Hara, "Fano resonant all-dielectric core/shell nanoparticles with ultrahigh scattering directionality in the visible region" *Optics Express*, 24(13), (2016).
- [32] M. Decker, I. Staude, M. Falkner, J. Dominguez, D.N. Neshev, I. Brener, T. Pertsch, and Y. S. Kivshar, "High-efficiency dielectric Huygens' surfaces" *Advanced Optical Materials*, 3(6), 813-820 (2015).
- [33] J. M. Geffrin, B. García-Cámara, R. Gómez-Medina, P. Albella, L.S.Froufe-Pérez, C. Eyraud, A. Litman, R. Vaillon, F. González, M. Nieto-Vesperinas and J. J. Sáenz, "Magnetic and electric coherence in forward-and back-scattered electromagnetic waves by a single dielectric subwavelength sphere" *Nature Communications*, 3(1), 1-8 (2012).
- [34] L. Novotony and B. Hecht, *Principles of Nano-Optics* (Cambridge University Press, 2012).
- [35] C. M. Soukoulis and M. Wegener, "Past achievement and future challenges in the development of three-dimensional photonic metamaterials" *Nature Photonics*, 5, 523-530 (2011).
- [36] D. Sikdar, I. D. Rukhlenko, W. Cheng and M. Premaratne, "Optimized gold nanoshell ensembles for biomedical applications" *Nanoscale Research Letters*, 8, 142-146 (2013).
- [37] L. Novotony and N. Van Hulst, "Antennas for light" *Nature Photonics*, 5, 83-90 (2011).
- [38] S. Lal, S. Link and N. J. Halas, "Nano-optics from sensing to wave-guiding" *Nature Photonics*, 1, 641-648 (2007).
- [39] A. E. Krasnok, I. S. Maksymov, A. I. Denisyuk, P. A. Belov, A. E. Miroshnichenko, C. R. Simovski and Y. S. Kivshar, "Optical nanoantennas" *Physics Uspekhi*, 56 (6), 539-564 (2013).

- [40] D. Sikdar, W. Cheng and M. Premaratne, “Optically resonant magneto-electric cubic nanoantennas for ultra-directional light scattering” *Journal of Applied Physics*, 117, 083101 (2015).
- [41] R. Gomez-Medina, B. Garcia-Camara, I. Suarez-Lacalle, F. Gonzalez, F. Moreno, M. Nieto-Vesperinas, and J. J. Saenz, “Electric and magnetic dipolar response of germanium nanospheres: Interference effects, scattering anisotropy and optical forces” *Journal of Nanophotonics*, 5, 053512 (2011).
- [42] Y. H. Fu, A. I. Kuznetsov, A. E. Miroshnichenko, Y. F. Yu and B. Lukyanchuk, “Directional visible light scattering by silicon nanoparticles” *Nature Communications*, 4, 1527 (2013).
- [43] T. Kalkbrenner, U. Håkanson and V. Sandoghdar, “Tomographic plasmon spectroscopy of a single gold nanoparticle” *Nano Letters*, 4 (12), 2309-2314 (2004).
- [44] H. H. Li, “Refractive index of Silicon and Germanium and its wavelength and temperature derivatives” *Journal of Physical Chemistry Reference Data*, 9, 561 (1980).



# **CHAPTER-4**



---

## CHAPTER-4

---

### ELLIPSOIDAL ALL-DIELECTRIC FANO RESONANT CORE-SHELL METAMATERIALS \*

---

#### 4.1 Introduction

In the last chapter, unidirectional scattering has been achieved in the dielectric meta-atom using the Generalized Kerker's condition for the nanoantenna applications. In this chapter, different approach of exciting Fano resonance in the dielectric metamaterial has been utilized to obtain unidirectional scattering which helps to increase directivity of the metamaterial based nanoantenna. Recent advances in the field of metamaterials have revolutionized the emerging field of nano-photonics by manipulating light at the subwavelength scales. This astonishing property of metamaterials is underpinning a lot of applications in nanoantennas, photovoltaics, super lens, cloaking and biomedicine [1 - 10].

---

\***R. Reena**, Y. Kalra, and A. Kumar, "Ellipsoidal all-dielectric Fano resonant core-shell metamaterials," *Superlattices and Microstructures* 118, 205 - 212 (2018).

---

All-dielectric resonators support electric as well as strong magnetic resonance even in the visible region [11, 23]. In the dielectric nanoparticles, magnetic resonance takes place by circular displacement current and in the metallic SRRs, resonance occurs due to conduction current. At magnetic resonance, in both the structures, electric field revolves around the resonator and magnetic field oscillates up and down in the middle of the resonator. First experimental demonstration of magnetic resonance in the dielectric resonators has been done in the GHz region, where it has been proved that dielectric resonators have three times higher quality factor than that of metallic SRRs [12]. Now, magnetic resonance has also been achieved in the visible region in all-dielectric nanoparticles [17, 18]. Dielectric nanostructures deliver another striking phenomenon of directional scattering which is well explained using Kerker's type scattering [24 - 26]. But the Kerker's type scattering takes place away from the resonance. In order to improve the directional scattering, Fano resonance has been achieved in the dielectric nanoparticles [27 - 29]. Fano resonance has asymmetric line profile in contrast to usual resonance profile or Lorentzian resonance profile [30, 31]. It is the constructive and destructive interference of discrete and continuum states of a system. In dielectric nanoparticles, broad electric dipole and narrow magnetic dipole resonances interfere to yield a Fano dip in the backward scattering.

In this chapter, ellipsoidal core/shell (Si/SiO<sub>2</sub>) nanoparticle has been considered in order to enhance directivity as compared to the Kerker's type scattering and spherical nanoparticles. In the design, core is made up of Silicon (Si) and shell is made up of Silica (SiO<sub>2</sub>). As the length of the semi-axis of the ellipsoidal nanoparticle along the electric field is decreased, it has been observed that two Fano resonances are excited, which is not possible in spherical nanoparticles. First Fano resonance is due to the interaction of dipolar moments and another Fano resonance is attributed to interaction of quadrupolar moments created at the lower wavelengths.

Fabrication of these ellipsoidal nanoparticles can be done using femtosecond laser ablation [32] and then silica layer can be formed by thermally oxidized the nanoparticles in dry air [27].

## 4.2 Design and analysis

The design has been proposed as ellipsoidal nanoparticle having core of Si and shell made up of SiO<sub>2</sub>. Refractive index of SiO<sub>2</sub> has been taken to be 1.45 and dispersion curve of refractive index with wavelength has been used for Si from Palik [33]. Core of the ellipsoidal nanoparticle has dimensions,  $a = 35$  nm,  $b = 70$  nm and  $c = 150$  nm, where,  $a$ ,  $b$  and  $c$  are the semi-axes of the ellipsoidal nanoparticle. Thicknesses of the shell of the ellipsoid are taken to be  $a_1 = 45$  nm,  $b_1 = 80$  nm,  $c_1 = 160$  nm i.e. 10 nm more than the length of core in all semi-axes as shown in figure 4.1.

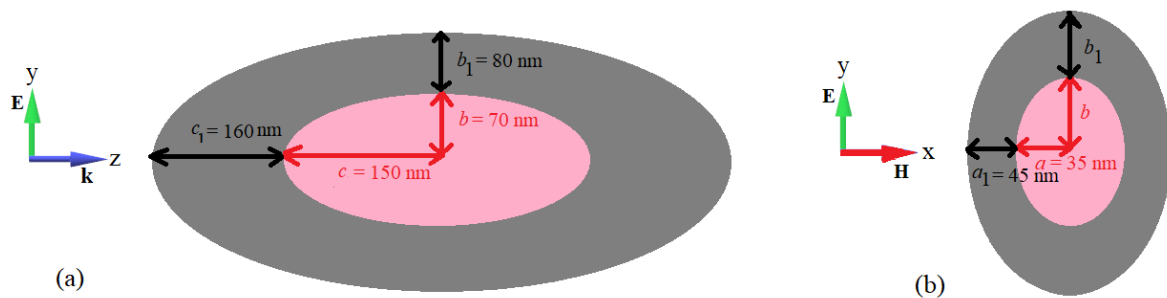


Figure 4.1 Schematic diagram of ellipsoidal nanoparticle (a) in the y-z plane and (b) in the x-y plane.

Magnetic dipoles can be induced in the high dielectric nanoparticles when they interact with the light of wavelength comparable to their size. Then electric dipole and other higher order modes are formed at the lower wavelengths. Induced multipoles in the nanoparticle i.e. electric dipole  $\mathbf{p}$ , magnetic dipole  $\mathbf{m}$ , electric quadrupole tensor  $Q_{\alpha\beta}$  and magnetic quadrupole tensor  $M_{\alpha\beta}$  are given by [25]

$$\mathbf{p} = \epsilon_0 (1 - \epsilon_{\text{eff}}) \int_V \mathbf{E}(\mathbf{r}) dV \quad (4.1)$$

$$\mathbf{m} = \frac{i\omega \epsilon_0 (1 - \epsilon_{\text{eff}})}{2c} \int_V [\mathbf{r} \times \mathbf{E}(\mathbf{r})] dV \quad (4.2)$$

$$Q_{\alpha\beta} = \frac{\epsilon_0 (1 - \epsilon_{\text{eff}})}{2} \int_V \left[ r_\alpha E_\beta + r_\beta E_\alpha - \frac{2}{3} (\mathbf{r} \cdot \mathbf{E}(\mathbf{r})) \delta_{\alpha\beta} \right] dV \quad (4.3)$$

$$M_{\alpha\beta} = \frac{i\omega \epsilon_0 (1 - \epsilon_{\text{eff}})}{3c} \int_V \left[ (\mathbf{r} \times \mathbf{E}(\mathbf{r}))_\alpha r_\beta + (\mathbf{r} \times \mathbf{E}(\mathbf{r}))_\beta r_\alpha \right] dV \quad (4.4)$$

where,  $c$ ,  $k_0 = \omega/c$  and  $z_0 = 1/\epsilon_0 c$  are the speed of light in vacuum, free space wavenumber and impedance, respectively, and  $\epsilon_0$  and  $\epsilon_{\text{eff}}$  are the vacuum permittivity and effective permittivity of the core-shell meta atom, respectively,  $\omega$  is the angular frequency,  $\mathbf{E}(\mathbf{r})$  is the electric field confined in the nanoparticle of volume  $V$  and  $\alpha$  and  $\beta$  are the cartesian components.  $\mathbf{E}(\mathbf{r})$  has been calculated using COMSOL Multiphysics commercial FEM based software and dipoles and quadrupoles has been calculated using Matlab. Effective permittivity  $\epsilon_{\text{eff}}$  has been calculated by the Maxwell Garnett formula as follows [34]

$$\epsilon_{\text{eff}} = \epsilon_s + \frac{\frac{1}{3} f_c (\epsilon_c - \epsilon_s) \sum_{k=1}^3 \frac{\epsilon_s}{\epsilon_s + N_k (\epsilon_c - \epsilon_s)}}{1 - \frac{1}{3} f_c (\epsilon_c - \epsilon_s) \sum_{k=1}^3 \frac{N_k}{\epsilon_s + N_k (\epsilon_c - \epsilon_s)}} \quad (4.5)$$

where  $\epsilon_s$  is the relative permittivity of shell,  $\epsilon_c$  is the relative permittivity of core,  $f_c$  is the volume fraction occupied by the core,  $N_k$  is the depolarization factor of the ellipsoidal nanoparticle whose definition and formula can be found in [35] and the index  $k = 1, 2, 3$  represents  $x, y$  and  $z$  cartesian coordinates.

Total scattered power is the sum of the power scattered by each multipole given by

$$P_{\text{scat}} = \frac{c^2 k_0^4 z_0}{12\pi} |\mathbf{p}|^2 + \frac{c^2 k_0^4 z_0}{12\pi} |\mathbf{m}|^2 + \frac{c^2 k_0^6 z_0}{40\pi} \sum |Q_{\alpha\beta}|^2 + \frac{c^2 k_0^6 z_0}{160\pi} \sum |M_{\alpha\beta}|^2 \quad (4.6)$$

Then total scattering cross section of each multipole has been calculated from scattered power in equation (4.6) using the equation

$$\sigma_{\text{scat}} = \frac{P_{\text{scat}}^p + P_{\text{scat}}^m + P_{\text{scat}}^Q + P_{\text{scat}}^M}{I_0} \quad (4.7)$$

where,  $P_{\text{scat}}^p$ ,  $P_{\text{scat}}^m$ ,  $P_{\text{scat}}^Q$  and  $P_{\text{scat}}^M$  are the scattered powers by electric dipole, magnetic dipole, electric quadrupole and magnetic quadrupole, respectively.  $I_0$  denotes the incident power density.

Directivity of the radiation pattern is the ratio of the radiation intensity in a given direction (in our case, it is forward direction) to the radiation intensity averaged over all directions. It is represented by  $D$  and it is dimensionless quantity which can be written in the mathematical form as [36]

$$D = \frac{4\pi U}{P_{\text{rad}}} \quad (4.8)$$

where,  $U$  is the radiation intensity in the particular direction and  $P_{\text{rad}}$  is total radiated power radiated in all directions.

### 4.3 Results and discussion

First of all, scattering spectra of the considered core-shell nanoparticle has been analyzed. It has been observed that magnetic dipole resonance is obtained at the wavelength of 640 nm and electric dipole has a broad spectrum having very small peak at 550 nm as shown in figure 4.2.

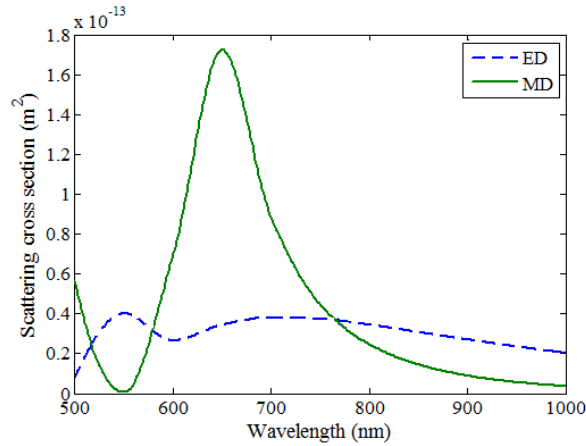


Figure 4.2. Scattering cross section of the nanoparticle representing broad electric dipole (ED) spectra and narrow magnetic dipole (MD) resonance.

In order to understand Fano resonance in the core-shell nanoparticle, scattering spectra has been analyzed distinctly for electric dipole and induced magnetic dipole. Due to the interference between narrow magnetic dipole resonance and broad electric dipole spectrum, Fano dip has been observed in the backward scattering at the wavelength of magnetic dipole i.e. 640 nm as shown in figure 4.3. At the same wavelength, forward scattering gets enhanced. At this wavelength, Kerker's first condition is not satisfied, according to which forward scattering takes place at the wavelength of interference of electric and magnetic dipoles [24], still there is suppression of backward scattering with enhancement of forward scattering. Hence, this can be completely attributed to the directional Fano resonance exhibited by the ellipsoidal nanoparticle. Fano resonance occurs in the vicinity of the wavelength of narrow spectra [37]. In our case, magnetic dipole and magnetic quadrupole have narrow spectrum as compared to the spectrum of electric dipole and electric quadrupole. So, Fano resonance occurs at the wavelengths of dipolar and quadrupolar magnetic resonances as shown in Fig. 4.3 (a) and (b). Further, at the wavelength of Fano resonance, on-resonant (at the wavelength of magnetic resonance) scattering takes place whereas the wavelength at which the Kerker's condition is satisfied, off-resonant scattering takes place. Thereby leading to the higher directivity at the wavelength of Fano resonance as compared to the directivity observed at the wavelength at which the Kerker's condition is satisfied [27].

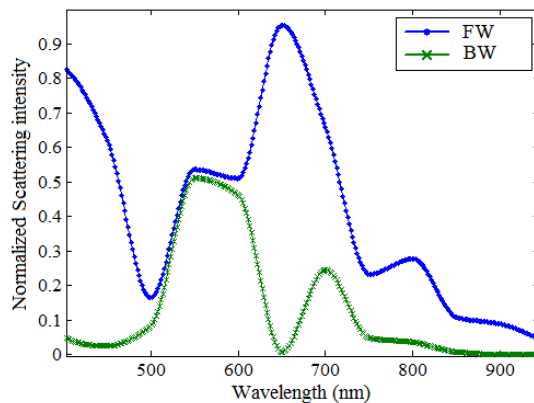


Figure 4.3 Normalized forward (FW) and backward (BW) scattering intensity showing Fano dip of backward scattering at  $\lambda = 640$  nm and enhancement of forward scattering at the same wavelength.



To study the variation in the Fano resonance, length of the ellipsoidal nanoparticle along its semi-axis  $b$  has been varied which is in the direction of the electric field. It has been observed that as the length of the ellipsoidal nanoparticle along semi-axis  $b$  is decreased and made equal to the length of the nanoparticle along semi-axis  $a$  i.e. 35 nm, two Fano resonances are exhibited. One of the Fano resonances is due to the interaction of narrow magnetic dipole resonance with comparatively broad electric dipole resonance as shown figure 4.4 (a).

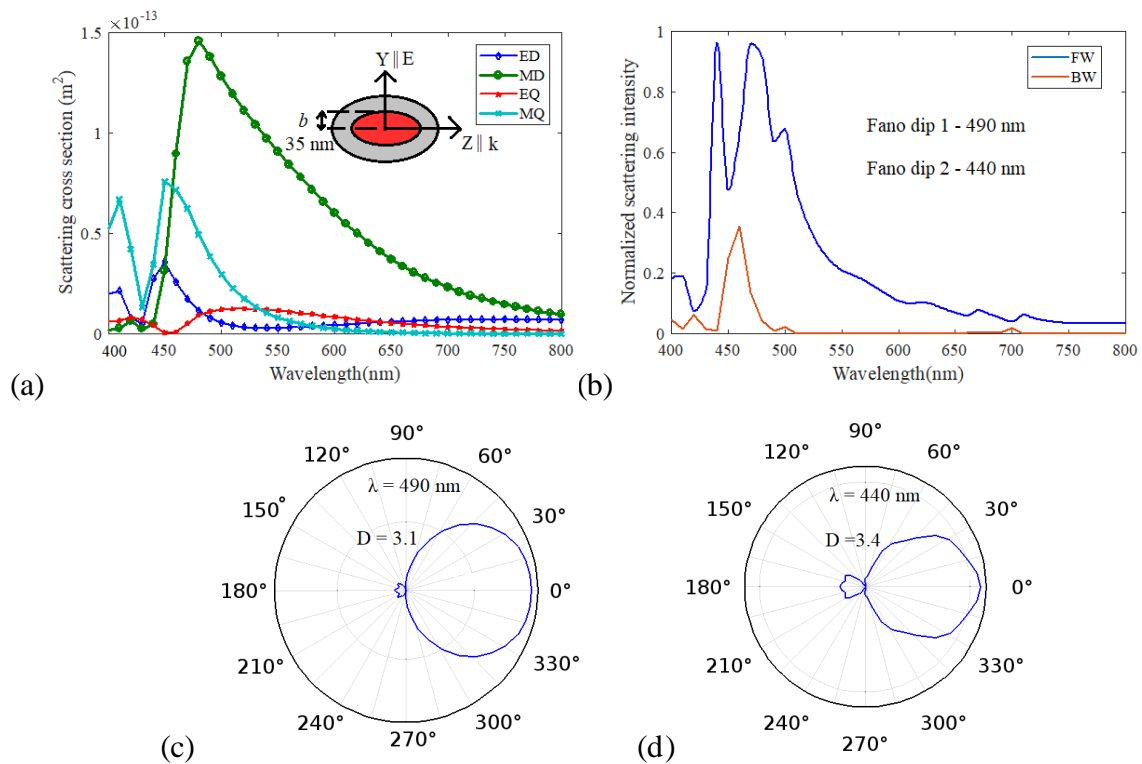


Figure 4.4 (a) Scattering spectra of ellipsoidal nanoparticle depicting distinct curves of dipoles and quadrupoles for core radius  $b = 35$  nm. (b) Forward and backward normalized scattering intensity showing Fano dips in the backward scattering at the wavelengths 490 nm and 440 nm due to dipole and quadrupole moments respectively. (c) – (d) Far-field scattering patterns at the Fano dip wavelengths.

Then Fano resonance dip in the backward scattering occurs at the wavelength of 490 nm followed by a peak in the forward scattering at the same wavelength as shown in the figure 4.4 (b). Another Fano resonance occurs due to the interference of electric and magnetic quadrupole moments, where magnetic quadrupole is narrow and electric quadrupole is broad as shown in figure 4.4 (a). This Fano dip in the backward scattering is obtained at the wavelength of 440

nm as shown in figure 4.4 (b). Far-field scattering patterns at these wavelengths of Fano resonance i.e. 490 nm and 440 nm have been shown in the figures 4.4 (c) and 4.4 (d), respectively. Directivities at the wavelengths 490 nm and 440 nm are obtained to be 3.1 and 3.4, respectively, calculated from equation (4.8). But, back lobe is more pronounced at 440 nm as shown in figure 4.4 (d).

Now, length of the nanoparticle along semi-axis  $b$  has been increased to 55 nm which red shifts the dipole and quadrupole moments and hence the Fano resonance wavelengths as shown in figure 4.5 (a). First Fano dip is obtained at the wavelength of 600 nm due to dipole moments and second Fano dip is obtained at the wavelength of 540 nm due to quadrupole moments as shown in figure 4.5 (b). Far field scattering patterns at the wavelengths of 600 nm with directivity 2.55 and 540 nm having directivity 2.64 have been shown in the figures 4.5 (c) and 4.5 (d), respectively.

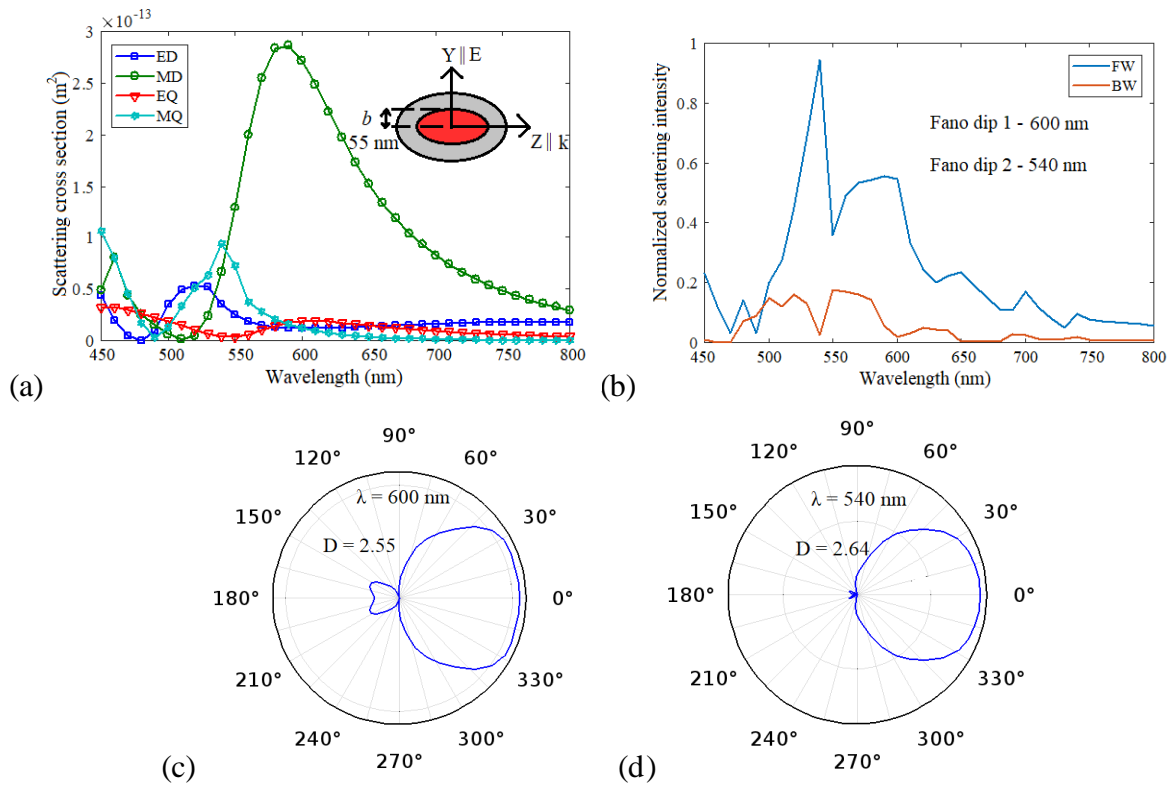


Figure 4.5 (a) Scattering spectra of the ellipsoidal nanoparticle at  $b = 55$  nm. (b) Forward and backward normalized scattering intensity showing Fano dips in the backward scattering at the wavelengths 600 nm and 540 nm. (c) – (d) Far-field scattering patterns at the Fano dip wavelengths.

Further, the length of the nanoparticle along semi-axis  $b$  has been increased to 75 nm. It has been observed that this time only one Fano resonance takes place at the wavelength of 650 nm. This Fano resonance is due to dipole moments. Scattering cross-section profile due to magnetic quadrupole becomes broader as we increase the size of the ellipsoidal nanoparticle along  $b$ -axis, as shown in figure 4.6 (a). Thus, there is no Fano resonance due to the interaction of quadrupolar moments as shown in figure 4.6 (b).

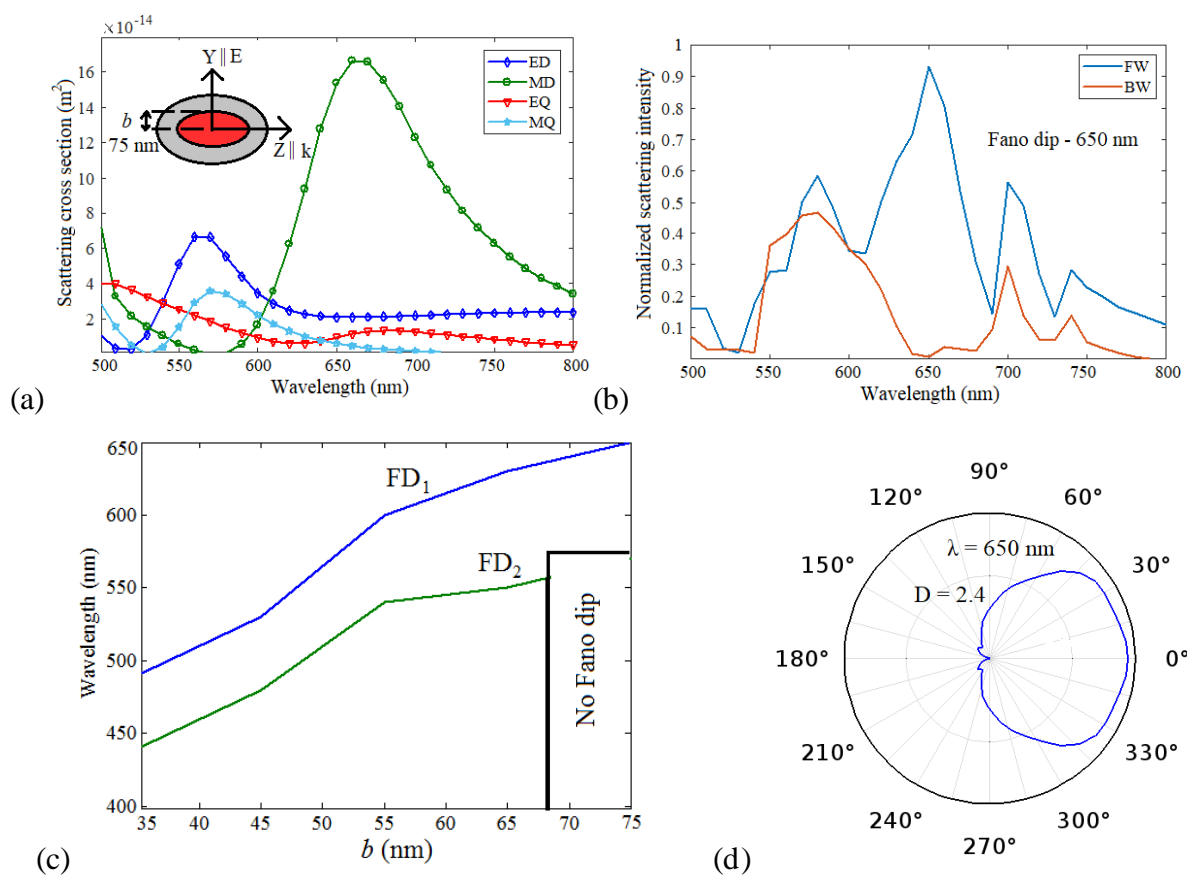


Figure 4.6 (a) Scattering spectra of the ellipsoidal nanoparticle at  $b = 75$  nm. (b) Forward and backward normalized scattering intensity showing Fano dip in the backward scattering at the wavelength 650 nm due to dipole moments only. (c) Variation of wavelength of Fano dips, FD<sub>1</sub> and FD<sub>2</sub> with length of semi-axis of ellipsoidal nanoparticle along electric field. (d) Far field scattering pattern at 650 nm.

In figure 4.6 (c), it has been shown that wavelength of Fano dip 1 (FD<sub>1</sub>) and Fano dip 2 (FD<sub>2</sub>) increase with the length of  $b$ -axis. But, as the length of the  $b$ -axis increases after 68 nm, appearance of the FD<sub>2</sub> vanishes. Far-field scattering pattern at the wavelength of Fano dip i.e. 650 nm has been shown in figure 4.6 (d). From the far-field pattern, it has been observed that

back-scattering is completely suppressed; however, there is small decrease in directivity due to enlarged beam- width of the lobe by increasing the length of nanoparticle along semi-axis  $b$ .

However, the length of the ellipsoidal nanoparticle along semi-axis  $a$  and  $c$  are kept constant i.e.  $a = 35$  nm and  $c = 150$  nm, because by increasing the length along semi-axis  $a$  or by decreasing the length along semi-axis  $b$ , ellipsoid approaches to sphere which results in diminishing of quadrupoles. In order to compare the results of ellipsoid and sphere, scattering cross section has been plotted in figure 4.7 (a) for sphere having core radius 70 nm and shell thickness 80 nm.

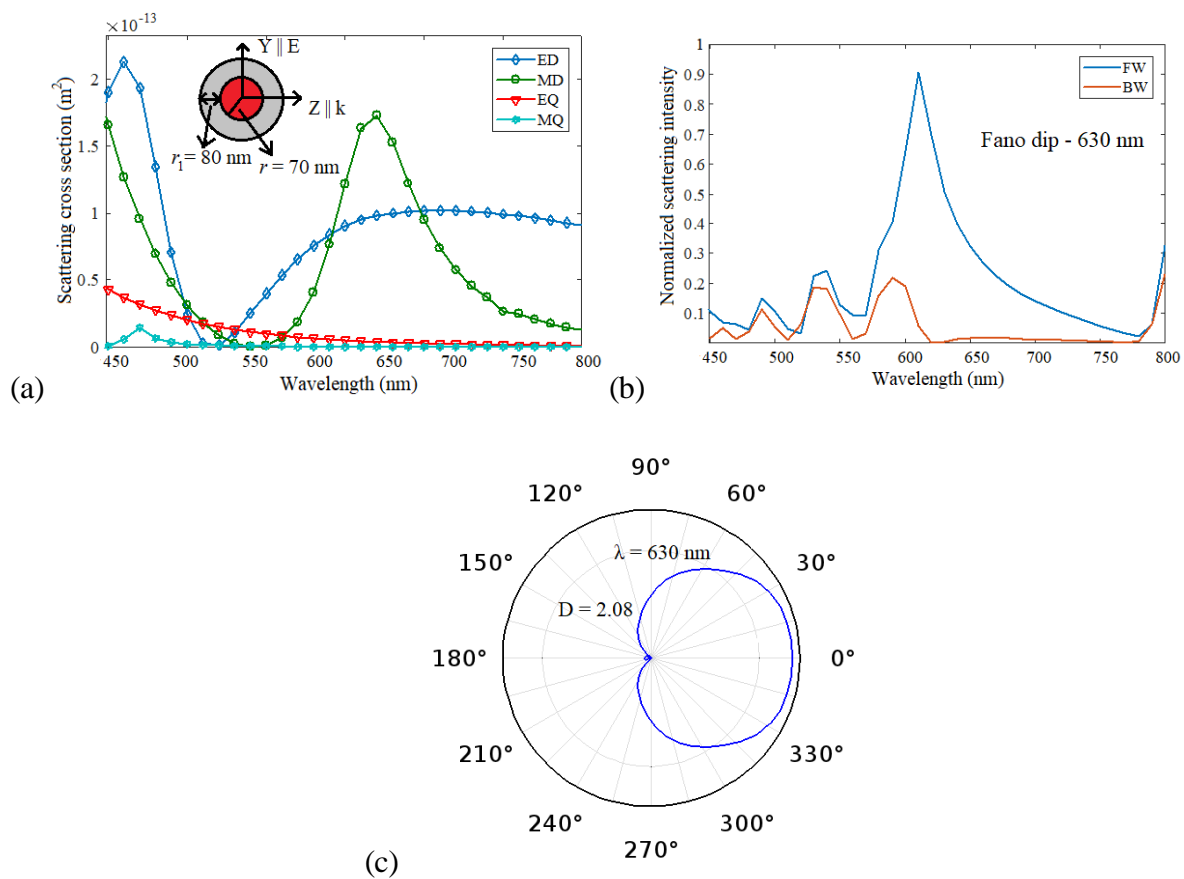


Figure 4.7 (a) Scattering spectra of the spherical nanoparticle of core radius 70 nm and shell thickness 80 nm. (b) Forward and backward normalized scattering intensity showing Fano dip in the backward scattering at the wavelength 630 nm due to dipole moments only. (c) Far field scattering pattern at 630 nm.

It has been observed that there is only one Fano dip at 630 nm due to narrow magnetic dipole and broad electric dipole as shown in figure 4.7 (b). But there is no Fano dip due to quadrupoles

because magnetic quadrupole is very small in case of sphere as compared to ellipsoid. Directivity is also decreased in case of spherical nanoparticle as shown in figure 4.7 (c).

#### **4.4 Conclusion**

In this chapter, ellipsoidal core-shell nanoparticle has been considered in which magnetic dipole has been optically induced. Electric dipole and higher order multipoles are created at lower wavelength side. Fano resonance has been observed at the wavelength of magnetic dipole due to the interaction of broad electric dipole and narrow magnetic dipole. When length of the semi-axis has been decreased which is along the electric field, double Fano resonance has been observed, one is due to the dipole moments and another is attributed to the interaction of broad electric quadrupole and narrow magnetic quadrupole. At these wavelengths of Fano resonance, directivity enhancement takes place which makes these ellipsoidal core-shell metamaterials promising candidate for nanoantenna applications.

## References

- [1] K. Lindfors, D. Dregely, M. Lippitz, N. Engheta, M. Totzeck and H. Giessen, “Imaging and steering unidirectional emission from nanoantenna array metasurfaces” *ACS Photonics*, 3 (2), 286-292 (2016).
- [2] J. Yan, M. Churong, L. Pu, W. Chengxin and Y. Guowei, “Electrically controlled scattering in a hybrid dielectric-plasmonic nanoantenna” *Nano Letters*, 17 (8), 4793-4800 (2017).
- [3] Y. Pang, J. Wang, Q. Cheng, S. Xia, X.Y. Zhou, Z. Xu, T.J. Cui and S. Qu, “Thermally tunable water-substrate broadband metamaterial absorbers” *Applied Physics Letters*, 110 (10), 104103 (2017).
- [4] D. Lee, H. Jeong and S. Lim, “Electronically switchable broadband metamaterial absorber” *Scientific Reports*, 7 (1), 4891 (2017).
- [5] G. Lipworth, J. Ensworth, K. Seetharam, D. Huang, J.S. Lee, P. Schmalenberg, T. Nomura, M. S. Reynolds, D. R. Smith and V. Urzhumov, “Magnetic metamaterial superlens for increased range wireless power transfer” *Scientific Reports*, 4, 3642 (2014).
- [6] A. O. Bak, E. O. Yoxall, P. Sarrigurea, V. Giannini, S. A. Maier, R. Hillenbrand, J. B. Pendry and C.C. Phillips, “Harnessing a quantum design approach for making low-loss superlenses” *Nano Letters*, 16 (3), 1609-1613 (2016).
- [7] Z. J. Wong, W. Yuan, O'Brien Kevin, R. Junsuk, Y. Xiaobo, Z. Shuang, F. Nicholas, Y. Ta-Jen and Z. Xiang, “Optical and acoustic metamaterials: superlens, negative refractive index and invisibility cloak” *Journal of Optics*, 19 (8), 084007 (2017).
- [8] D. Shin, Y. Urzhumov, Y. Jung, G. Kang, S. Baek, M. Choi, H. Park, K. Kim and D. R. Smith, “Broadband electromagnetic cloaking with smart metamaterials” *Nature Communications*, 3, 1213 (2012).
- [9] W. Cai, U.K. Chettiar, A.V. Kildishev and V.M. Shalaev, “Optical cloaking with metamaterials” *Nature Photonics*, 1 (4), 224-227 (2007).
- [10] Y. Jin, “Engineering plasmonic gold nanostructures and metamaterials for biosensing and nanomedicine” *Advanced Materials*, 24 (38), 5153-5165 (2012).
- [11] S. Jahani and Z. Jacob, “All-dielectric metamaterials” *Nature Nanotechnology*, 11 (1) 23-36 (2016).
- [12] B.I. Popa and S.A. Cummer, “Compact dielectric particles as a building block for low-loss magnetic metamaterials” *Physical Review Letters*, 100 (20), 207401 (2008).

- [13] Q. Zhao, J. Zhou, F. Zhang and D. Lippens, “Mie resonance-based dielectric metamaterials” *Materials Today*, 12 (12), 60-69 (2009).
- [14] Y. Yang, A.E. Miroshnichenko, S.V. Kostinski, M. Odit, P. Kapitanova, M. Qiu and Y.S. Kivshar, “Multimode directionality in all-dielectric metasurfaces” *Physical Review B*, 95 (16), 165426 (2017).
- [15] A. Ahmadi and H. Mosallaei, “Physical configuration and performance modeling of all-dielectric metamaterials” *Physical Review B*, 77 (4), 045104 (2008).
- [16] D.A. Powell, “Interference between the modes of an all-dielectric meta-atom” *Physical Review Applied*, 7 (3), 034006 (2017).
- [17] A. I. Kuznetsov, A. E. Miroshnichenko, Y. H. Fu, J. B. Zhang and B. Luk’yanchuk, “Magnetic light” *Scientific Reports*, 2, 492 (2012).
- [18] A. B. Evlyukhin, S. M. Novikov, U. Zywietz, R. L. Eriksen, C. Reinhardt, S. I. Bozhevolnyi and B. N. Chichkov, “Demonstration of magnetic dipole resonances of dielectric nanospheres in the visible region” *Nano Letters*, 12 (7), 3749-3755 (2012).
- [19] N. A. Butakov and J. A. Schuller, “Designing multipolar resonances in dielectric metamaterials” *Scientific Reports*, 6, 38487 (2016).
- [20] N. Shankhwar, R. K. Sinha, Y. Kalra, S. Makarov, A. Krasnok and P. Belov, “High-quality laser cavity based on all-dielectric metasurfaces” *Photonics and Nanostructures - Fundamentals and Applications*, 24, 18-23 (2017).
- [21] P. Moitra, B. A. Slovick, W. Li, I. I. Kravchenko, D. P. Briggs, S. Krishnamurthy and J. Valentine, “Large-scale all-dielectric metamaterial perfect reflectors” *ACS Photonics*, 2 (6) 692-698 (2015).
- [22] F. Zhang, L. Kang, Q. Zhao, J. Zhou and D. Lippens, “Magnetic and electric coupling effects of dielectric metamaterial” *New Journal of Physics*, 14 (3), 033031 (2012).
- [23] R. Gomez-Medina, B. Garcia-Camara, I. Suarez-Lacalle, F. Gonzalez, F. Moreno, M. Nieto-Vesperinas and J.J. Saenz, “Electric and magnetic dipolar response of germanium nanospheres: interference effects, scattering anisotropy, and optical forces” *Journal of Nanophotonics*, 5 (1), 053512 (2011).
- [24] Reena, Y. Kalra, A. Kumar and R.K. Sinha, “Tunable unidirectional scattering of ellipsoidal single nanoparticle,” *Journal of Applied Physics* 119 (24), 243102 (2016).
- [25] D. Sikdar, W. Cheng and M. Premaratne, “Optically resonant magneto-electric cubic nanoantennas for ultra-directional light scattering,” *Journal of Applied Physics*, 117 (8), 083101 (2015).

- [26] I. Devi, R. Dalal, Y. Kalra and R.K. Sinha, “Modeling and design of all-dielectric cylindrical nanoantennas” *Journal of Nanophotonics*, 10 (4), 046011 (2016).
- [27] Y. Tsuchimoto, T. Yano, T. Hayashi and M. Hara, “Fano resonant all-dielectric core/shell nanoparticles with ultrahigh scattering directionality in the visible region” *Optics Express*, 24 (13), 14451-14462 (2016).
- [28] A. E. Miroshnichenko and Y. S. Kivshar, “Fano resonances in all-dielectric oligomers” *Nano Letters*, 12 (12) 6459-6463 (2012).
- [29] J. Yan, P. Liu, Z. Lin, H. Wang, H. Chen, C. Wang and G. Yang, “Directional Fano resonance in a silicon nanosphere dimer” *ACS Nano*, 9 (3) 2968-2980 (2015).
- [30] A.E. Miroshnichenko, S. Flach and Y.S. Kivshar, “Fano resonances in nanoscale structures,” *Reviews of Modern Physics*, 82 (3) 2257 (2010).
- [31] B. Luk’yanchuk, N.I. Zheludev, S.A. Maier, N.J. Halas, P. Nordlander, H. Giessen and C.T. Chong, “The Fano resonance in plasmonic nanostructures and metamaterials” *Nature Materials*, 9 (9) 707-715 (2010).
- [32] P. A. Dmitriev, S. V. Makarov, V. A. Milichko, I. S. Mukhin, A. S. Gudovskikh, A. A. Sitnikova, A. K. Samusev, A. E. Krasnok and P. A. Belov, “Laser fabrication of crystalline silicon nanoresonators from an amorphous film for low-loss all-dielectric nanophotonics” *Nanoscale*, 8 (9), 5043-5048 (2016).
- [33] E.D. Palik, in: E.D. Palik (Ed.), *Handbook of Optical Constants of Solids*, (Academic Press, Orlando, Florida, U.S, 1985).
- [34] M. Y. Koledintseva, R. E. DuBroff and R. W. Schwartz, “A Maxwell Garnett model for dielectric mixtures containing conducting particles at optical frequencies” *Progress In Electromagnetics Research B*, 63, 223-242 (2006).
- [35] C. F. Bohren and D. R. Huffman, *Absorption and Scattering of Light by Small Particles*, (John Wiley & Sons, 2008).
- [36] C. A. Balanis, *Antenna Theory: Analysis and Design*, third ed., (John Wiley & Sons, Hoboken, New Jersey, U.S, 2005).
- [37] B. S. Luk’yanchuk, A. E. Miroshnichenko and Y. S. Kivshar, “Fano resonances and topological optics: an interplay of far- and near-field interference phenomena” *Journal of Optics*, 15 (7), 073001 (2013).



# **CHAPTER-5**



---

## CHAPTER-5

---

### FANO RESONANT CUBOIDAL DIELECTRIC METAMATERIAL NANOANTENNAS \*

---

#### 5.1 Introduction

Metamaterial nanoantennas are the subwavelength nanoparticles which can convert free propagating radiation into localized near field and vice versa in the visible or near infrared range [1 - 4]. Recently, nanoantennas are seeking attention due to their potential applications in sensors, spectroscopy, microscopy, optical communication, solar cells, and optical tweezers [5 - 16]. Metallic nanoparticles like split ring resonators have been used for more than a decade to design the nanoantennas because earlier they were the only devices which can interact with the electric as well as magnetic part of the light efficiently [17, 18]. But in the visible region, losses in metals take place due to the free electrons in the conduction band leads to low radiation efficiency in the visible region.

---

\***R. Reena**, Y. Kalra and A. Kumar, "Fano Resonant Cuboidal Dielectric Nanoantennas," Optics and Spectroscopy 127, 1122-1127 (2019).

---

High index dielectric nanoparticles provide an alternative to the metallic nanoantennas. These high index dielectric nano structures also exhibit magnetic resonance like metallic split ring resonator (SRR) structures as discussed in the previous chapters. Dielectric resonators support both electric and magnetic resonances in the visible region and the resonant wavelength can be tuned by varying the size of the nanoparticle.

To improve the forward scattering, Fano resonance has been introduced in the dielectric nanoparticles where on-resonance forward scattering takes place at the wavelength of either electric or magnetic resonance [19]. But in symmetric dielectric resonators, electric and magnetic dipoles are formed at different wavelengths which make them less suitable for the applications like highly directional nanoantennas. To utilize these dielectric nanoparticles efficiently, it is required to bring electric and magnetic dipoles closer to each other. Earlier, electric and magnetic resonances have been tuned using various methods to spectrally overlap the resonances, but they are confined only to infrared region [20, 21].

In this chapter, highly directional properties have been achieved in silicon (Si) cuboidal nanoparticles in the visible region. The spectral positions of electric and magnetic dipoles have been tuned by adjusting the aspect ratio of cuboidal nanoparticles. This leads to the interaction of broad electric dipole resonance and narrow magnetic dipole resonance that results in Fano resonance. This paves the way for enhanced forward to backward scattering ratio, directivity and radiation efficiency which is applicable in highly directional nanoantennas.

## **5.2 Design and analysis**

The cuboidal Silicon nanoparticles have been considered which have been elongated along either the x or the z directions so that they can be transformed into the cuboidal nanodisks and cuboidal nanorods respectively of finite length. The optical properties of Silicon have been taken from the derived values of refractive index and absorption coefficient by Kramers Kronig

relation using experimental reflectance data [22]. The dimensions of the nanoparticle have been taken to be ‘ $a$ ’, ‘ $b$ ’ and ‘ $c$ ’ where  $a$  and  $b$  are the length and breadth and  $c$  is the height of the nanoparticle. In the cuboidal Si nanodisk, plane wave has been made incident on the nanoparticle along x-axis and direction of polarization is along z-axis as shown in figure 5.1 (a). In the cuboidal Si nanorod, direction of propagation and polarization is along z-axis and y-axis respectively as shown in figure 5.1 (b). In the cuboidal Si nanodisk, dimensions are taken such that  $a = b > c$  and in case of cuboidal Si nanorod,  $a = b < c$ .

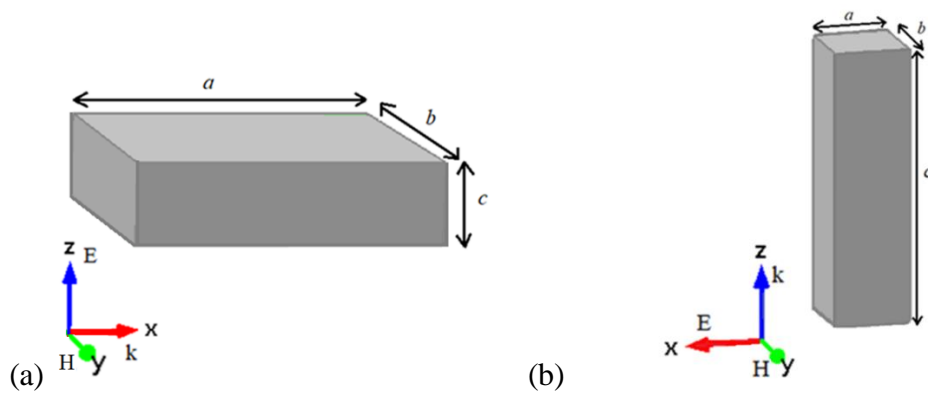


Figure 5.1. Schematic diagram of plane wave incident on cuboidal silicon nanoparticles transformed into the shape of (a) disk and (b) rod.

When the plane wave having propagation vector  $\mathbf{k}$  is incident on the nanoparticle, it polarizes the nanoparticle with polarization current density,  $\mathbf{J} = -i\omega\mathbf{P}$ , where  $\omega$  and  $\mathbf{P}$  are the angular frequency and polarization vector respectively. If the nanoparticle is kept in a non-magnetic and non-absorbing surrounding medium, time-averaged extinction power  $P_{\text{ext}}$  can be described by Poynting theorem as [23]

$$P_{\text{ext}} = \text{Im} \left( \frac{\omega}{2} \int_V \mathbf{E}_0^*(\mathbf{r}) \cdot \mathbf{P}(\mathbf{r}) dV' \right) \quad (5.1)$$

where  $\mathbf{E}_0(\mathbf{r})$  and  $\mathbf{r}$  denotes the electric field of the incident wave and position vector respectively. Polarization vector can be written as  $\mathbf{P}(\mathbf{r}) = \epsilon_0(\epsilon_r - 1)\mathbf{E}(\mathbf{r})$  where  $\epsilon_0$  and  $\epsilon_r$  represent vacuum permittivity and relative permittivity of the nanoparticle respectively.

For the non-absorbing nanoparticle,  $P_{\text{abs}} = 0$ . Hence, extinction power becomes equal to scattered power i.e.  $P_{\text{ext}} = P_{\text{scat}}$ . As the polarization vector  $\mathbf{P}(\mathbf{r})$  is decomposed into multipolar terms, scattered power  $P_{\text{scat}}$  also gets decomposed into electric dipole, magnetic dipole, electric quadrupole and magnetic quadrupole terms as

$$P_{\text{scat}} = P_{\text{scat}}^{\text{P}} + P_{\text{scat}}^{\text{m}} + P_{\text{scat}}^{\text{Q}} + P_{\text{scat}}^{\text{M}} + \text{higher order terms} \quad (5.2)$$

Here, only electric dipole and magnetic dipole terms have been considered and other higher order terms have been neglected as they are very small as compared to dipoles and also, they are not formed in the visible region. Hence, the scattered power  $P_{\text{scat}}$  for dipoles only can be written as

$$P_{\text{scat}} \approx \frac{c^2 k_0^4 z_0}{12\pi} |\mathbf{p}|^2 + \frac{c^2 k_0^4 z_0}{12\pi} |\mathbf{m}|^2 \quad (5.3)$$

where first term and second term are the scattered fields due to electric dipole and magnetic dipole respectively,  $c$  is the speed of light in vacuum,  $k_0 = \omega/c$  and  $z_0 = 1/(\epsilon_0 c)$  represent the free space wavenumber and free space impedance respectively;  $\mathbf{p}$  and  $\mathbf{m}$  are the electric and magnetic dipole moments having the values

$$\mathbf{p} = \epsilon_0 (1 - \epsilon_r) \int_V \mathbf{E}(\mathbf{r}') dV' \quad (5.4)$$

$$\mathbf{m} = \frac{i\omega\epsilon_0 (1 - \epsilon_r)}{2c} \int_V [\mathbf{r} \times \mathbf{E}(\mathbf{r}')] dV' \quad (5.5)$$

where  $\mathbf{E}(\mathbf{r}')$  has been calculated using finite element method based Comsol Multiphysics. Now, scattering cross section  $\sigma_{\text{scat}}$  can be easily calculated by normalizing scattered power  $P_{\text{scat}}$  with the incident power density  $I_0$  given by

$$\sigma_{\text{scat}}^{\text{P}} = \frac{P_{\text{scat}}^{\text{P}}}{I_0} \quad (5.6)$$

$$\sigma_{\text{scat}}^m = \frac{P_{\text{scat}}^m}{I_0} \quad (5.7)$$

where  $\sigma_{\text{scat}}^p$  and  $\sigma_{\text{scat}}^m$  are the scattering cross section due to electric dipole and magnetic dipole respectively. Total scattering cross section  $\sigma_{\text{scat}}$  is the sum of the scattering cross section due to electric dipole and magnetic dipole i.e.

$$\sigma_{\text{scat}} = \sigma_{\text{scat}}^p + \sigma_{\text{scat}}^m \quad (5.8)$$

## 5.3 Results and discussion

### 5.3.1 Forward and backward scattering intensity

In this section, the variation of forward and backward scattering intensity with the position of the electric dipole (ED) and magnetic dipole (MD) has been analyzed.

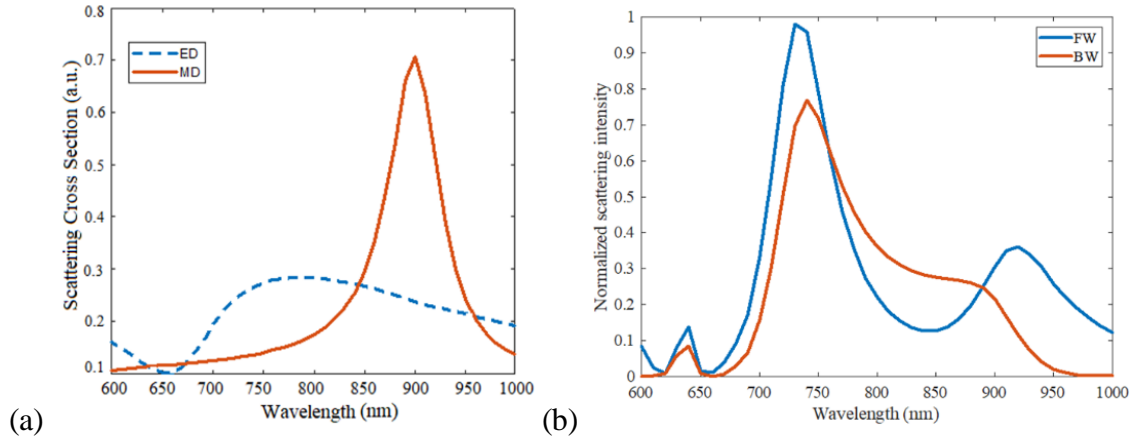


Figure 5.2 (a) Scattering cross section spectra of cube having length 200 nm corresponding to electric dipole (ED) and magnetic dipole (MD). (b) Normalized forward (FW) and backward (BW) scattering.

To compare the results with our design of cuboidal nanoparticles, first of all symmetric cubic nanoparticles has been discussed. For the Si cubic nanoparticle of length 200 nm, electric dipole and magnetic dipole resonances take place at 760 nm and 890 nm respectively, as shown in figure 5.2 (a). Normalized forward (FW) and backward (BW) scattering intensity has been shown in figure 5.2 (b) which shows that at the position of electric and magnetic dipole

resonance i.e. at 760 nm and 890 nm, forward and backward scattering are equal. Electric dipole and magnetic dipole scattering cross-section interfere at 844 nm and 958 nm. Forward scattering takes place at 958 nm, backward scattering is zero at this wavelength but at 844 nm, backward scattering is more than the forward scattering. This is due to the fact that electric and magnetic dipoles are in phase (first Kerker's condition) at 958 nm and they are out of phase (second Kerker's condition) at 844 nm. But in this type of symmetric structures, forward scattering is not so pronounced to make them suitable for highly directional nanoantennas because electric and magnetic resonances take place at different wavelengths. To get forward scattering with enhanced directivity, it is necessary to bring electric and magnetic resonances closer to each other.

To achieve this goal, symmetrical cubic nanoparticle has been converted into cuboidal nanodisk and nanorod. First we discuss about cuboidal nanodisk as shown in figure 5.1 (a). Length ' $a$ ' and breadth ' $b$ ' of the nanodisk are kept constant and optimized to be equal to 200 nm. Scattering cross section has been calculated using equations (5.3) – (5.8) and its spectra has been plotted in the figures 5.3 (a) – 5.3 (d) by varying the height  $c$  of the nanoparticle from 50 nm to 80 nm. It can be analyzed from the figures 5.3 (a) and 5.3 (b) that electric and magnetic dipole resonances overlap spectrally up to the height  $c = 60$  nm after that as we go on increasing the height of the nanoparticle shown in the figures 5.3 (c) and 5.3 (d), spectral positions of electric and magnetic dipole moment get separated from each other. Also, spectral positions of electric and magnetic dipoles are red shifted by increasing the height of the nanoparticle. Figures 5.3 (e) – 5.3 (h) represent normalized forward (FW) and backward (BW) scattering intensity for different heights ranging from  $c = 50$  nm to  $c = 80$  nm. Further, it can be analyzed from figure 5.3 (a) that electric and magnetic dipole resonances spectrally overlap at wavelength 440 nm and it can be observed from the figure 5.3 (e) that enhancement of forward scattering and suppression of backward scattering takes place at the same wavelength of 440



nm. The cause for the suppression of backward scattering is the Fano dip at the wavelength of 440 nm which is the consequence of the interaction of narrow magnetic dipole and broad electric dipole mode which acts as dark mode and bright mode respectively as shown in figure 5.3 (a).

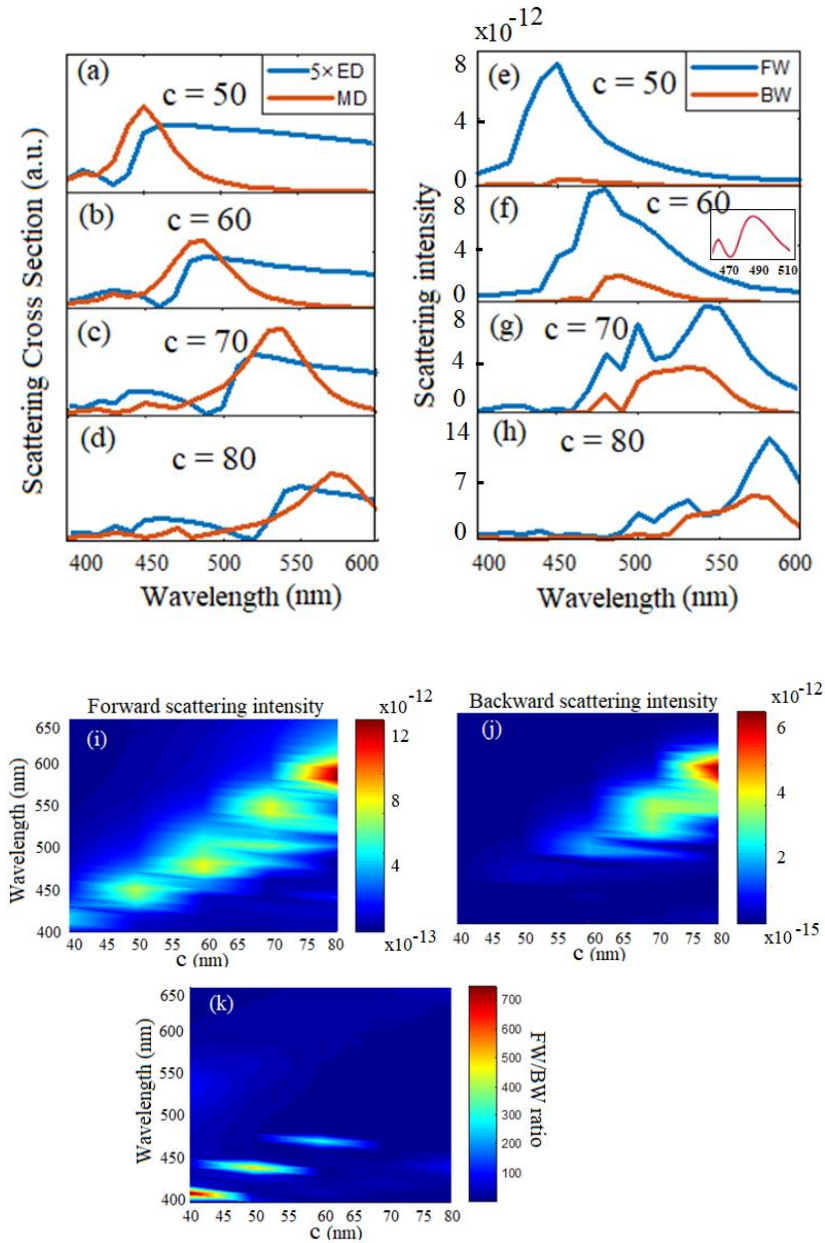


Figure 5.3. Scattering cross section spectra for the electric dipole moment (ED) and magnetic dipole moment (MD) of the cuboidal nanodisk having dimensions  $a = b = 200$  nm (a)  $c = 50$  nm (b)  $c = 60$  nm (c)  $c = 70$  nm and (d)  $c = 80$  nm (e)-(h) Corresponding normalized scattering intensity depicting forward and backward scattering for  $c = 50 - 80$  nm. Inset of the figure (f) shows Fano dip at the wavelength 470 nm. (i) Forward scattering intensity (j) backward scattering intensity of the cuboidal nanodisk with respect to wavelength and dimension of the nanodisk. (k) Forward to backward intensity ratio.

Similarly, a Fano dip can be observed at 470 nm in the figure 5.3 (f) for the Si cuboidal nanodisk of height 60 nm due to the interference of spectrally overlapped broad electric and narrow magnetic dipole modes at 470 nm as shown in figure 5.3 (b). However, for the heights 70 nm and 80 nm, electric and magnetic resonances do not spectrally overlap, therefore forward and backward scattering takes place at the same wavelength which is not appropriate for highly directional nanoantennas.

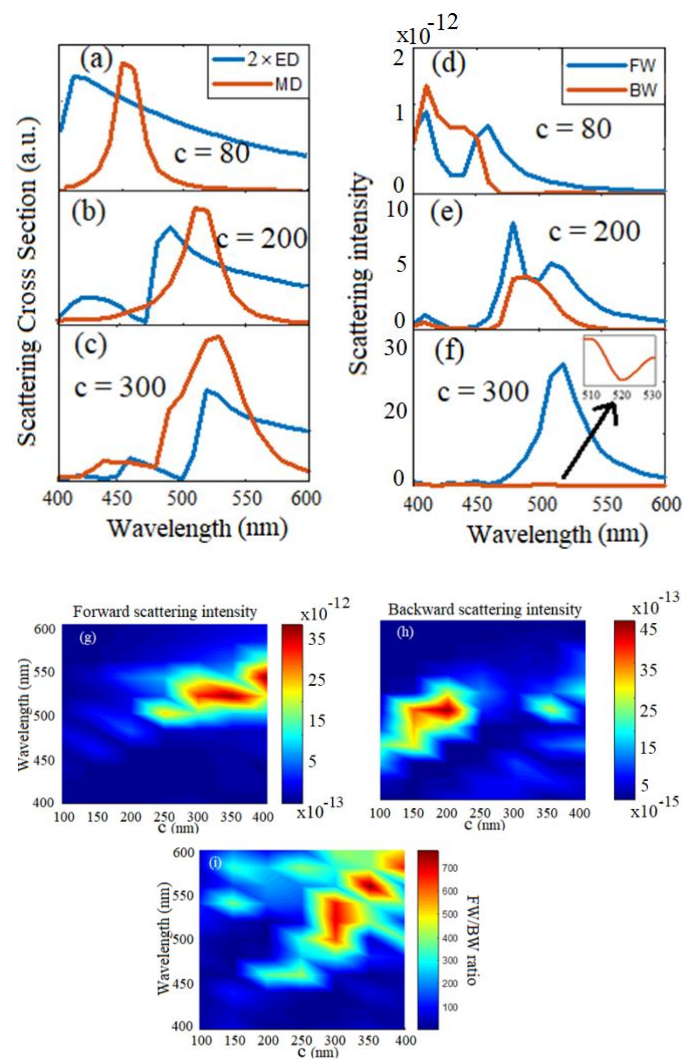


Figure 5.4. Scattering cross section spectra for the electric dipole moment (ED) and magnetic dipole moment (MD) of the cuboidal nanorod having dimensions  $a = b = 80$  nm (a)  $c = 80$  nm (b)  $c = 200$  nm and (c)  $c = 300$  nm (d)-(f) Corresponding normalized scattering intensity depicting forward and backward scattering for  $c = 80 - 300$  nm. Inset of the figure (f) shows Fano dip at the wavelength 520 m. (g) forward scattering intensity (h) backward scattering intensity of the cuboidal nanodisk with respect to wavelength and dimension of the nanodisk. (i) Forward to backward (FW/BW) intensity ratio.

Surface plots for the forward scattering intensity, backward scattering intensity and forward to backward ratio as a function of wavelength and height of the nanodisk  $c$  have been shown in figures 5.3 (i) – 5.3 (k). It can be analyzed from the figures 5.3 (i) and 5.3 (j) that up to 60 nm, forward scattering is high but backward scattering is negligible but after 60 nm height, backward scattering starts increasing which affects the forward to backward ratio as shown in figure 5.3 (k).

Further, symmetrical cubic nanoparticle has been converted into cuboidal nanorod. Length  $a$  and breadth  $b$  are optimized and taken to be  $a = b = 80$  nm. The scattering spectra has been plotted in the figures 5.4 (a) – (c) for different heights of the nanorod  $c = 80$  nm, 200 nm and 300 nm. For  $c = 80$  nm, cubic nanoparticle is symmetric, so electric and magnetic dipole resonances occur at different wavelengths as shown in figure 5.4 (a). By increasing the height of the nanorod, electric and magnetic dipole resonances come closer and they spectrally overlap for the nanorod of height 300 nm at the wavelength of 520 nm.

Normalized forward (FW) and backward (BW) scattering has been plotted in the figures 5.4 (d) – (f). It has been analyzed that for the spectrally overlapping electric and magnetic dipole resonances, forward scattering is enhanced and backward scattering is suppressed as shown in the figure 5.4 (f). The reason for the enhancement of forward scattering is the on-resonance scattering that takes place for spectrally overlapping resonances. Due to the interaction of broad electric and narrow magnetic dipole resonances, Fano resonance takes place at their resonance position i.e. at the wavelength of 520 nm. Fano dip in the backward scattering occurs at the wavelength of 520 nm as shown in the inset of figure 5.4 (f). It is evident from the figure 5.4 (g) that forward scattering is high for the nanorods of height greater than 200 nm. Also, it can be seen in the figure 5.4 (h) that backward scattering is high for the nanorods with height less than 200 nm. Figure 5.4 (i) depicts that forward to backward (FW/BW) scattering ratio is high equal to 700 at the wavelength 520 nm for the nanorod of height 300 nm. Further by increasing

the height of the nanorod, wavelengths with high FW/BW ratio also increase. But, figure 5.4 (g) shows that wavelength with high forward scattering does not increase which indicates that the high FW/BW ratio is not due to high forward scattering but is due to low backward scattering. But a high forward scattering is a required condition for the design of highly directional nanoantenna.

### 5.3.2 Radiation efficiency

Radiation efficiency is also an important parameter for a nanoantenna to examine how much power has been radiated in the far field by the nanoantenna. Radiation efficiency  $\eta_{\text{rad}}$  and directivity  $D$  have been calculated as [24]

$$\eta_{\text{rad}} = \frac{P_{\text{rad}}}{P_{\text{input}}} \quad (5.9)$$

$$D = \frac{4\pi}{P_{\text{rad}}} \text{Max} [p(\theta, \varphi)] \quad (5.10)$$

where  $P_{\text{rad}}$  is the total power radiated by the antenna in the far field zone and  $P_{\text{input}}$  is the total power accepted by the antenna at its input terminals during radiation,  $\theta$  and  $\varphi$  are the angles of spherical coordinate system and  $p(\theta, \varphi)$  is the power radiated in the direction  $\theta$  and  $\varphi$ .

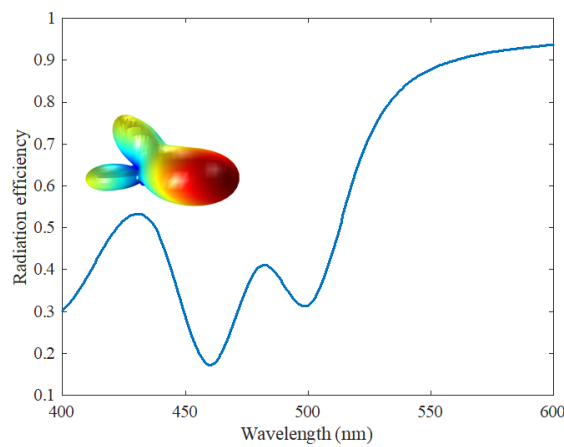


Figure 5.5. Radiation efficiency of the disk having dimensions  $a = b = 200$  nm and  $c = 50$  nm. The inset shows the three dimensional radiation pattern at the wavelength 440 nm with directivity 3.9 in the forward direction.

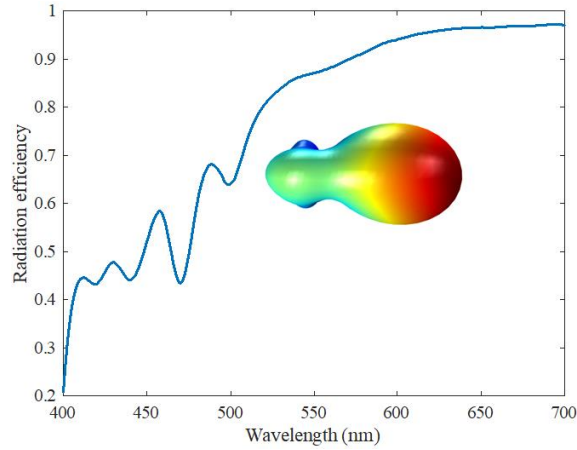


Figure 5.6. Radiation efficiency and of the rod having dimensions  $a = b = 80$  nm and  $c = 200$  nm. The inset shows the three dimensional radiation pattern at the wavelength 520 nm having directivity 4.2 in the forward direction.

Radiation efficiency with respect to wavelength for the Si cuboidal nanodisk has been plotted in the figure 5.5. It shows that the radiation efficiency is equal to 0.5 at 440 nm wavelength where forward scattering takes place for the optimized dimensions of the disk i.e.  $a = b = 200$  nm and  $c = 50$  nm with high forward to backward ratio which was shown in the figure 5.3. Radiation pattern has also been shown at the same wavelength which has directivity equal to 3.9 in the forward direction

Further, plot of radiation efficiency with respect to wavelength for the Si cuboidal nanorod has been shown in the figure 5.6. At 520 nm of wavelength, radiation efficiency is 0.8 for the optimized dimensions of the rod i.e.  $a = b = 80$  nm and  $c = 300$  nm where high forward to backward scattering takes place that has been shown in the figure 5.4. Radiation pattern has also been shown at the same wavelength which has directivity equal to 4.2 in the forward direction. It has been observed that in the case of cuboidal nanorod, radiation efficiency is high as compared to cuboidal nanodisk at their respective wavelengths. The reason behind the less radiation efficiency in case of cuboidal nanodisk is that losses become high in Silicon near this wavelength. The above analysis indicates that cuboidal nanodisk and nanorod are promising candidates that can be used as highly directional nanoantennas.

## 5.4 Conclusion

In this chapter, cuboidal silicon nanoparticles have been proposed to achieve unidirectional enhanced forward scattering in contrast to symmetrical cubic nanoparticles. Both variants of cuboidal nanoparticles i.e. the nanodisk and the nanorod type structures have been analyzed to get spectrally overlapping electric and magnetic dipole resonances. In the case of a cuboidal nanodisk, electric and magnetic dipole resonances come closer by decreasing the height of the nanoparticle in the direction of polarization of the incident plane wave. At a particular height of cuboidal nanodisk i.e. 50 nm, electric and magnetic resonances spectrally overlap and due to the broad electric and narrow magnetic dipole resonance, Fano dip takes place at the wavelength of 440 nm which results in enhanced forward scattering at that wavelength. Forward and backward scattering have also been calculated at other heights of nanodisk, to show the difference. In the case of nanorod, height of the nanoparticle has been increased in the direction of propagation. At the height of 300 nm, electric and magnetic dipole resonances spectrally overlap and Fano resonance takes place at the wavelength of 520 nm. Forward scattering is enhanced and backward scattering is suppressed at this height of the nanorod. Moreover, optimized cuboidal nanodisk and nanorod exhibit high value of radiation efficiency and directivity. Thus, these cuboidal nanodisk and nanorod act as highly directional nanoantennas.

## References

- [1] F. Monticone and A. Alu. “Metamaterial, plasmonic and nanophotonic devices” Reports on Progress in Physics, 80(3), 036401 (2017).
- [2] L. Novotny and N. V. Hulst “Antennas for light” Nature photonics, 5 (2), 83 (2011).
- [3] A. E. Krasnok, I. S. Maksymov, A. I. Denisyuk, P. A. Belov, A. E. Miroschnichenko, C. R. Simovski and Y. S. Kivshar, “Optical nanoantennas” Physics Uspekhi, 56 (6), 539-564 (2013).
- [4] A. E. Krasnok, A. E. Miroschnichenko, P. A. Belov and Y. S. Kivshar, “All-dielectric optical nanoantennas” Optics Express, 20(18), 20599-20604 (2012).
- [5] Y. Zhao, N. Engheta, and A. Andrea, “Effects of shape and loading of optical nanoantennas on their sensitivity and radiation properties” Journal of Optical Society of America, B, 28 (5), 1266-1274 (2011).
- [6] D. Rodrigo, A. Tittl, A. John-Herpin, O. Limaj and H. Altug, “Self-similar multiresonant nanoantenna arrays for sensing from near-to mid-infrared” ACS Photonics, 5(12) 4903-4911 (2018).
- [7] S. Law, L. Yu, A. Rosenberg and D. Wasserman, “All-semiconductor plasmonic nanoantennas for infrared sensing” Nano Letters, 13(9), 4569-4574 (2013).
- [8] A. Krasnok, M. Caldarola, N. Bonod, and A. Alú, “Spectroscopy and biosensing with optically resonant dielectric nanostructures” Advanced Optical Materials, 6 (5), (2018).
- [9] A. I. Barreda, J. M. Saiz, F. González, F. Moreno and P. Albella, “Recent advances in high refractive index dielectric nanoantennas: Basics and applications” AIP Advances, 9 (4), 040701 (2019).
- [10] P. Albella, R. A. de la Osa, F. Moreno and S. A. Maier, “Electric and magnetic field enhancement with ultralow heat radiation dielectric nanoantennas: Considerations for surface-enhanced spectroscopies” ACS Photonics, 1, 524–529 (2014).
- [11] T. Kalkbrenner, U. Håkanson, A. Schädle, S. Burger, C. Henkel and V. Sandoghdar, “Optical microscopy via spectral modifications of a nanoantenna” Physical Review Letters, 95, 200801 (2005).
- [12] J. H. Yan, Z. Y. Lin, P. Liu, and G. W. Yang, “A design of Si-based nanoplasmonic structure as an antenna and reception amplifier for visible light communication” Journal of Applied Physics, 116, (15), 154307 (2014).

- [13] C. Y. Yang, J. H. Yang, Z. Y. Yang, Z. X. Zhou, M.G. Sun, V. E. Babicheva, and K. P. Chen, “Nonradiating silicon nanoantenna metasurfaces as narrowband absorbers,” *ACS Photonics* 5, (7), 2596-2601 (2018).
- [14] Y. M. El-Toukhy, M. Hussein, M. F. O. Hameed, A. M. Heikal, M. M. Abd-Elrazzak, and S. S. A. Obayya, “Optimized tapered dipole nanoantenna as efficient energy harvester” *Optics Express*, 24, (14), A1107-A1122 (2016).
- [15] A. El Eter, N. M. Hameed, F. I. Baida, R. Salut, C. Filiatre, D. Nedeljkovic, A. Elie, B. Samuel, and T. Grosjean, “Fiber-integrated optical nano-tweezer based on a bowtie-aperture nano-antenna at the apex of a SNOM tip” *Optics Express*, 22, (8), 10072-10080 (2014).
- [16] M. Ploschner, M. Mazilu, T. F. Krauss, and K. Dholakia, “Optical forces near a nanoantenna” *Journal of Nanophotonics*, 4, (1), 041570 (2010).
- [17] Y. Liu, S. Palomba, Y. Park, T. Zentgraf, X. Yin, and X. Zhang, “Compact magnetic antennas for directional excitation of surface plasmons,” *Nano Letters*, 12, 4853–4858 (2012).
- [18] T. Kosako, Y. Kadoya, and H. F. Hofmann, “Directional control of light by a nano-optical Yagi–Uda antenna,” *Nature Photonics*, 4, 312–315 (2010).
- [19] Y. Tsuchimoto, T. Yano, T. Hayashi, and M. Hara, “Fano resonant all-dielectric core/shell nanoparticles with ultrahigh scattering directionality in the visible region” *Optics Express*, 24, 14451-14462 (2016).
- [20] S. Liu, A. Vaskin, S. Campione, O. Wolf, M. B. Sinclair, J. Reno, G. A. Keeler, I. Staude and I. Brener, “Huygens’ metasurfaces enabled by magnetic dipole resonance tuning in split dielectric nanoresonators” *Nano Letters*, 17, 4297-4303 (2017).
- [21] I. Staude, A. E. Miroshnichenko, M. Decker, N. T. Fofang, S. Liu, E. Gonzales, J. Dominguez, T. S. Luk, D. N. Neshev, I. Brener and Y. Kivshar, “Tailoring directional scattering through magnetic and electric resonances in subwavelength silicon nanodisks” *ACS Nano*, 7, 7824-7832 (2013).
- [22] M. A. Green, “Self-consistent optical parameters of intrinsic silicon at 300 K including temperature coefficients” *Solar Energy Materials and Solar Cells*, 92, 1305–1310 (2008).
- [23] L. Novotny and B. Hecht “Principles of nano-optics” (Cambridge University press, 2012).
- [24] C. A. Balanis, “Antenna theory: analysis and design” (John wiley & sons, 2016).



# **CHAPTER-6**



---

## CHAPTER-6

---

### ELECTROMAGNETICALLY INDUCED TRANSPARENCY IN METAL-DIELECTRIC METAMATERIAL \*

---

#### 6.1 Introduction

In the previous chapters, speciality optical fiber and metamaterials has been designed and their analysis has been done for various applications like fiber lasers and amplifiers, telecommunication and nanoantennas. In this chapter, electromagnetically induced transparency has been excited in the hybrid metal-dielectric metamaterial which has potential applications in optical buffers and sensing. Electromagnetically induced transparency is a quantum optical phenomenon used to make an opaque object transparent in a narrow spectral region by increasing the transmittance [1 - 3]. Earlier, EIT was observed in the atomic systems of gases only [1, 3]. Later, EIT was demonstrated in solid states of rare earth metals [4] and solid state system of ensemble based on quantum optics [5] for optical data storage.

---

\* **R. Reena**, Y. Kalra and A. Kumar, “Electromagnetically induced transparency-based metal dielectric metamaterial and its terahertz sensing application,” *Applied Optics*, 60(34), 10610-10616 (2021).

---

However, experimentally it is very difficult to set up such an EIT system due to its high sensitivity to temperature and inhomogeneous broadening [6]. Since Alzar et al. [7] demonstrated EIT in classical coupled oscillator, this topic has attracted huge attention.

Metamaterials are the subwavelength resonators whose unprecedented properties depend on the sizes and shapes of the resonance structures [8, 9]. Electromagnetically induced transparency was introduced in optical metamaterials, making it possible to get EIT in solid materials with greater stability [10 – 18]. Electromagnetically induced transparency has many applications like slow light, sensors, modulators, optical switching and optical storage [17 - 28]. Most of the EIT-like behaviors depend on the bright-dark modes interference creating steep dispersion in the group index which is useful for making slow light devices and sensors [10 - 24]. However, such a narrow band EIT cannot be employed to design signal process devices like band pass filters and optical buffers. Broadband, multi-band and tunable EIT has been achieved in various bright-dark-bright resonators and bright and multi-quasi-dark modes resonators [25 - 29]. Another approaches of making broadband EIT is to increase the number of resonators or by inducing asymmetry in the EIT structure [30 - 35]. But, increasing number of resonators makes the device bulky and difficult to fabricate. Asymmetry in the structure makes the device polarization sensitive. Due to which EIT could be lost by changing the angle of incidence of light. Recently, Polarization independent EIT metamaterial has been introduced with large delay bandwidth product by Bagci *et al.* [36]. Another ultra-broadband and polarization independent EIT metamaterial has been introduced by Hu *et al.* [37]. But they are in the gigahertz region. More recently, polarization independent dual band electromagnetically induced transparency has been achieved in hybrid metamaterial structure for the application of 6G wireless communication systems at 1 THz frequency [38].

Broadband EIT is required for getting large delay bandwidth product but for the sensing applications, high quality factor resonance is necessary. As EIT phenomenon is associated with Fano resonance, it is also characterized with high quality factor resonance. Out of the entire electromagnetic spectrum, terahertz sensing has utmost significance in the fields like biomedicine and atmospheric environment monitoring [39 - 41]. Metallic split ring resonators have been widely used to depict the unusual properties of metamaterials to control and confine the electromagnetic fields. However, the conventional split ring resonators (SRR) have low quality factor due to high radiative and non-radiative losses in the terahertz region which make them less suitable for sensing applications. In low quality factor sensors, it is difficult to detect shifts in the resonance frequency [42, 43]. The quality factor of SRR has been improved by introducing Fano resonance using asymmetrical split ring resonator structure [44, 45] or using c-shaped split ring resonator [46]. The quality factor can be enhanced using Graphene instead of metal in the metamaterial based sensors [47].

In this chapter, electromagnetically induced transparency has been achieved in the hybrid metal-dielectric metamaterial. Electric dipole produced by metal ring acts as bright mode while electric dipole and magnetic dipole produced in the dielectric resonator work as bright mode and quasi-dark mode. Magnetic dipole in the dielectric resonator is called quasi-dark mode due to its high quality factor as compared to bright modes. Two EIT windows have been obtained in the transmission spectrum, one of which has been obtained due to destructive interference of bright and quasi-dark mode and another EIT window has been obtained due to destructive interference of bright-bright modes. These two EIT bands can be merged into one broad EIT band by changing the length of the metal ring. Moreover, the structure is polarization independent due to the symmetry of the structure. Therefore, EIT is not affected by changing the angle of incidence. Phase delay of 5 picoseconds has been obtained in the EIT region from 1.8 THz to 2.2 THz so that delay bandwidth product of the unit cell of the metamaterial comes

out to be equal to 2. Such a high delay bandwidth product makes the proposed design appropriate for making optical buffers which are served as optical memories in computers. Moreover, at two dipole resonances, there are two high quality factor Fano dips which are useful for sensing applications.

## 6.2 Design parameters of the metamaterial

Figure 6.1 illustrates the design of the metamaterial consisting of dielectric cube at the top, Al metal ring at the bottom and there is a glass spacer of refractive index 1.6 between the two.

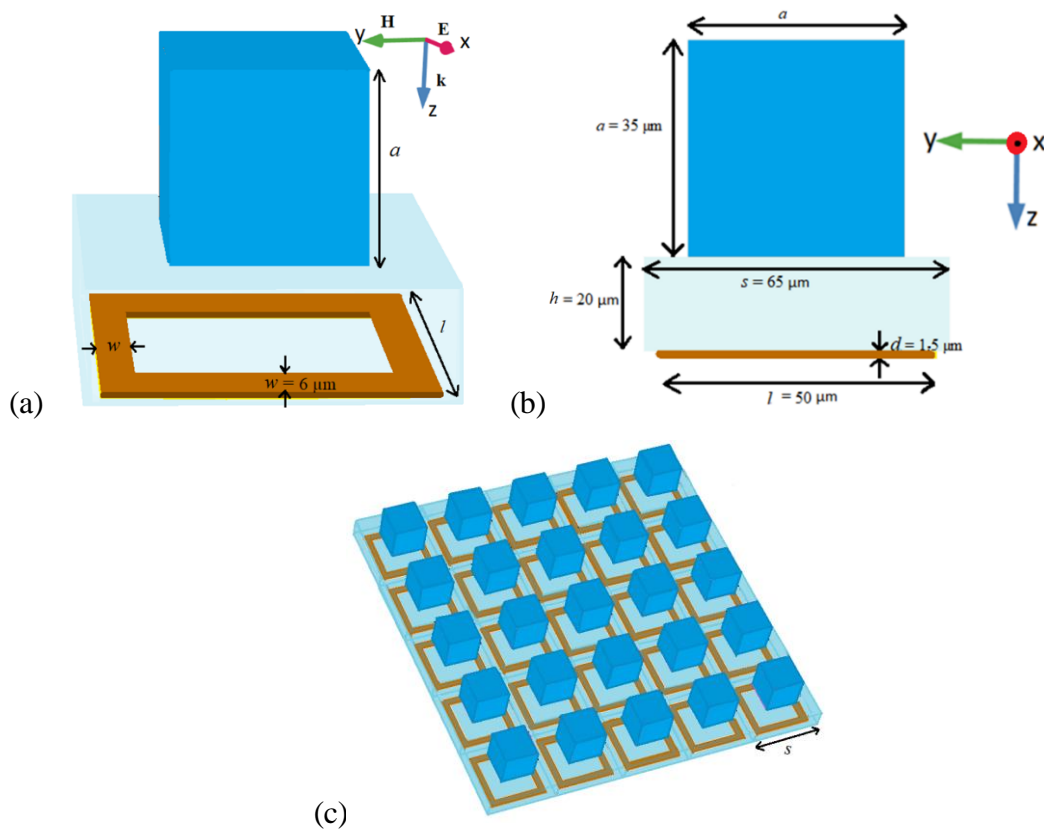


Figure 6.1. (a) 3-D and (b) 2-D view of the unit cell of the metamaterial along with dimensions showing normally incident excitation. In the geometry, at the top there is a dielectric cube of side  $a = 35 \mu\text{m}$ , in the bottom there is a metal ring of side  $l = 50 \mu\text{m}$ , width  $w = 6 \mu\text{m}$  and thickness  $d = 1.5 \mu\text{m}$ . Dielectric cube and metal ring are separated by a glass spacer of height  $h = 20 \mu\text{m}$ . (c) Periodic array of metamaterial with periodicity  $s = 65 \mu\text{m}$ .

Figures 6.1 (a) and 6.1 (b) describe the 3-D and 2-D view of the unit cell of the proposed design along with geometric parameters. The periodic array of the metamaterial has been shown in

the figure 6.1 (c). The dielectric cube of side  $a = 35 \mu\text{m}$  and metal ring of length  $l = 50 \mu\text{m}$ , width  $w = 6 \mu\text{m}$  and height  $d = 1.5 \mu\text{m}$  have been considered. The dielectric cube and metal ring have been separated by a spacer of length  $s = 65 \mu\text{m}$  and height  $h = 20 \mu\text{m}$ . The dimensions and material of the metamaterial are chosen such that the system operate in the THz region.

The transmission spectra and electromagnetic fields have been calculated using Comsol Mutiphysics based on finite element method. The electromagnetic waves are incident from top in the negative  $z$ -direction as shown in the figure 6.1 (a). The electric and magnetic fields are polarized in the  $x$  and  $y$  directions, respectively. A frequency domain solver is used with perfect electric and magnetic boundary conditions in the  $x$ - $y$  plane. Port boundary condition has been applied at top and bottom of the structure in the  $z$ - direction. Optical properties of aluminium as described by the Drude model

$$\epsilon_m = 1 - \omega_p^2 / (\omega^2 + i\omega\gamma) \quad (6.1)$$

where plasma frequency  $\omega_p = 2\pi \times 3606 \text{ THz}$  and collision frequency  $\omega_l = 2\pi \times 19.6 \text{ THz}$  [48] have been used. The dielectric GaTe has refractive index 4 from 1.5 THz to 2.5 THz [49]. Due to the same periodicity in the  $x$  and  $y$  directions and symmetric structure on both sides, proposed resonator is polarization independent.

### 6.3 Resonance properties

First of all, resonance properties of metal ring and dielectric cube have been studied separately. Transmission spectra of metal ring has been shown in the figure 6.2 (a) for different lengths of metal ring. Resonance transmission dips has been observed in the transmission spectra at different frequencies for different lengths of metal ring. There is a blue shift in the resonance frequency by decreasing the length of the ring because resonance frequency is inversely proportional to the size of the ring [50]. Electric field distribution and electric field directions illustrate the electric dipole resonance in the metal ring as shown in figure 6.2 (b). Hao *et al.*

has demonstrated electric and magnetic dipolar resonances in the single closed metal ring using the plasmon resonance [50]. The transmission spectra of metal ring are Lorentzian like lineshape. Therefore, it's quality factor can be calculated using Lorentzian lineshape formula

$$|S_{21}| = |1 - \text{Im}(K/(\omega^2 - \omega_0^2 + i\omega\gamma))| \quad (6.2)$$

where  $K$  is a constant,  $\omega_0$  is the resonance frequency and  $\gamma$  is the damping rate of the resonance [48]. Quality factor of resonance in the metal ring comes out to be  $Q = \omega_0/2\gamma \approx 2.4$  for  $l = 50 \mu\text{m}$ .

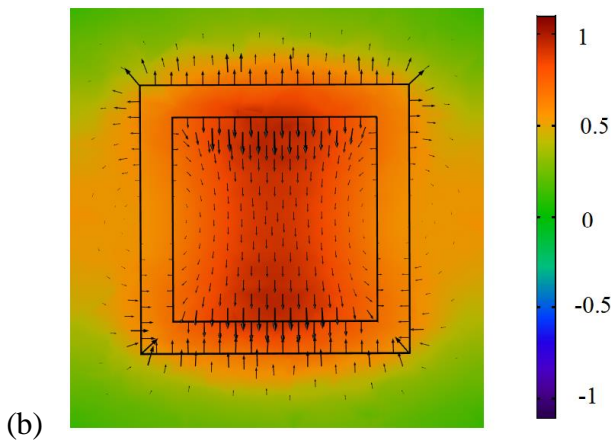
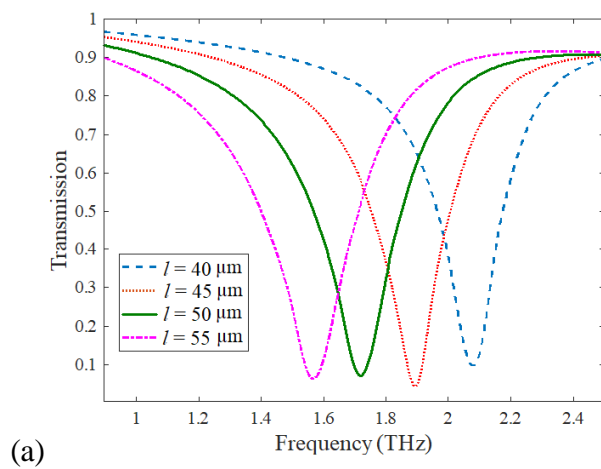


Figure 6.2 (a) Transmission spectra of metal ring with spacer by varying the length of the ring. (b) Electric field distribution in the metal ring on the top of the spacer at electric dipolar resonance frequency for  $l = 50 \mu\text{m}$  at 1.72 THz. Black arrows represent the direction of electric field.

Now transmission spectra of dielectric resonator have been analyzed which is shown in the figure 6.3 (a). Two resonance dips have been observed in the transmission spectra at the



frequency of 1.79 THz and 2.3 THz. These dips are due to the magnetic and electric dipole formation at the frequency of first dip and second dip, respectively. Electric field distribution and direction of electric field has been shown in the figure 6.3 (b) and figure 6.3 (c) at frequencies 1.79 THz and 2.3 THz, respectively shows Mie type resonance modes. The magnetic resonance dip in the figure 6.3 (a) has Fano-like lineshape profile. Therefore, quality factor of the magnetic resonance has been calculated using the Fano formula as

$$|S_{21}| = |a_1 + ia_2 + (b/(\omega - \omega_0 + i\omega\gamma))| \quad (6.3)$$

where,  $a_1$ ,  $a_2$  and  $b$  are constant real numbers,  $\omega_0$  is the resonance frequency and  $\gamma$  is the damping rate of the resonance [48]. Then quality factor of the magnetic resonance of the cube can be calculated as  $Q = \omega_0/2\gamma \approx 10.4$ . The electric resonance dip has the Lorentzian like profile.

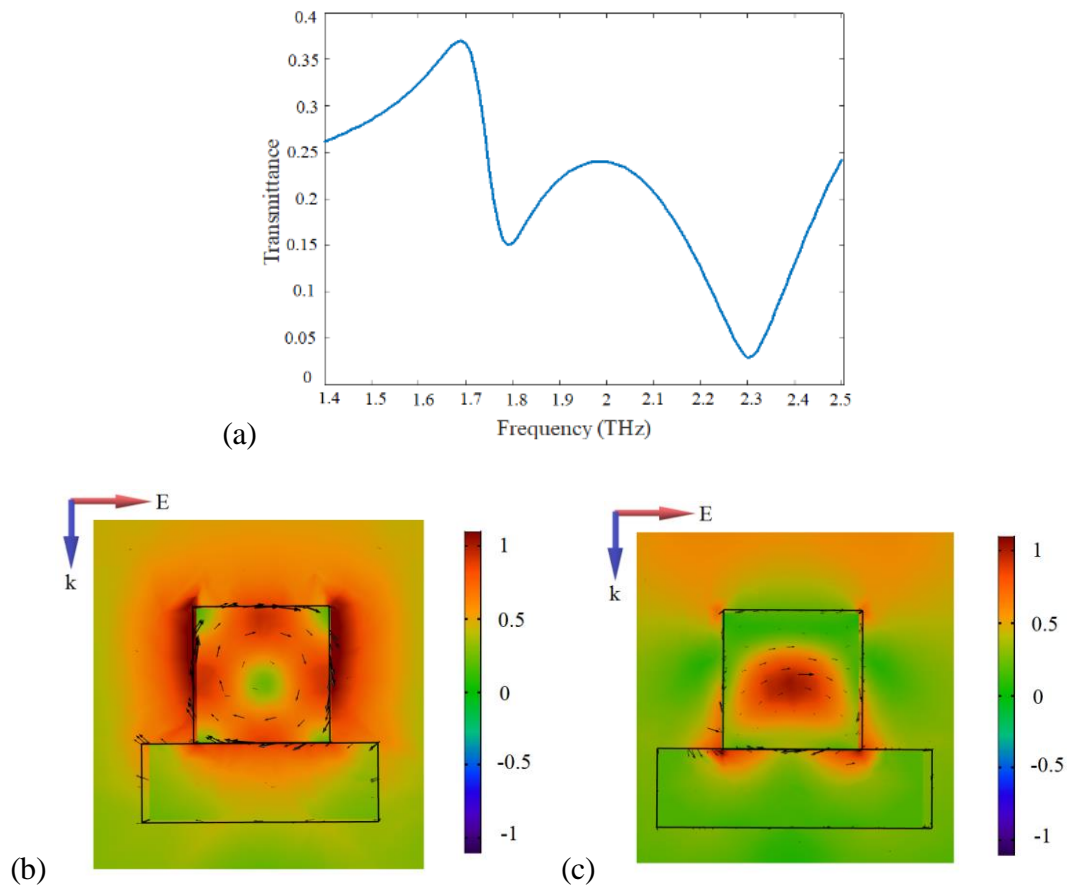


Figure 6.3 (a) Transmission spectra of the dielectric with spacer showing magnetic resonance at 1.79 THz and electric resonance at 2.3 THz. Electric field distribution of the dielectric at (b) magnetic resonance frequency and (c) electric resonance frequency. Black arrows in the figures (b) and (c) depict the directions of the electric field.

Therefore, its quality factor can be calculated using the Lorentzian formula which was used above. The quality factor of electric resonance of dielectric cube comes out to be  $Q \approx 4.8$ . The quality factor of magnetic resonance of dielectric cube is higher than the electric dipole resonances of metal ring and dielectric cube but could be excited by the incident field. Therefore, magnetic dipole of dielectric cube is called the quasi-dark mode and electric dipoles of metal ring and dielectric cube are called bright modes.

Next, we analyze the effect of combining the metal ring and dielectric cube on the transmittance spectra. Dielectric cube has been set up on the top, then spacer and metal ring has been kept in the bottom of the hybrid resonator and plane wave is incident from top of the resonator as shown in the figure 6.1. It has been observed that two EIT windows are created in the transmittance spectra of the hybrid metamaterial resonator for the length of metal ring,  $l = 40 \mu\text{m}$  as shown in the figure 6.4 by the blue curve. First EIT window is created due to destructive interference of the bright mode of the metal ring and the quasi-dark mode of the dielectric cube. While the second EIT window is emerged due to the destructive interference of bright modes of metal ring and dielectric cube. Further, as the length of metal ring is increased to  $l = 45 \mu\text{m}$ , the two EIT windows are merged into one and single broad EIT window has been obtained. It is due to the change in detuning of the resonance frequencies which is well explained in the reference [51]. As the length of the metal ring is further increased to  $l = 50 \mu\text{m}$ , the EIT window becomes broader with enhanced transmittance as shown by the black curve in figure 6.4. Furthermore, by increasing the length of the metal ring to  $l = 55 \mu\text{m}$ , makes the EIT window narrower with lower quality factors of the EIT dips as shown in the figure 6.4 by violet curve. Therefore,  $l = 50 \mu\text{m}$  is our optimized length of the metal ring.

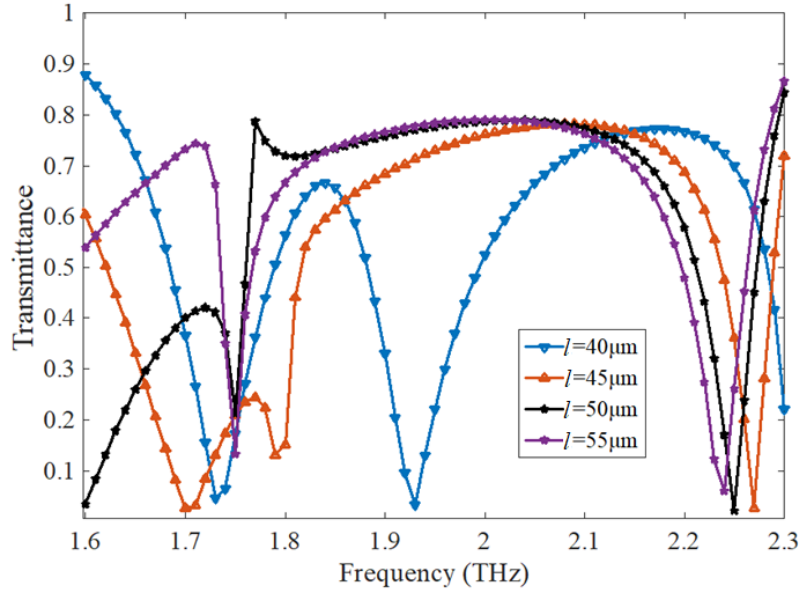


Figure 6.4. Transmission spectra of the EIT resonator with both dielectric and metal ring with glass spacer in between the both. Transmittance has been plotted for different length of the metal ring from  $l = 40 \mu\text{m}$  to  $l = 55 \mu\text{m}$ .

To get the better view of the transmittance for  $l = 50 \mu\text{m}$ , separate figure has been plotted in the figure 6.5 (a). A broad EIT window from 1.8 THz to 2.2 THz has been obtained with nearly 75% transmission. In order to better understand the EIT like response, electric field distributions along with directions of electric field have been plotted at different frequencies in the figures 6.5 (b) - (f). At the frequency of 1.6 THz, only metallic ring has been excited due to the incident field as shown in the figure 6.5 (b). The direction of electric field flowing in the spacer due to the electric dipole resonance of the metal ring is along the direction of the incident electric field which shows bright mode like behaviour [32]. At the frequency of 1.75 THz, magnetic dipole is also excited in the dielectric cube and electric field is flowing in the same direction at the interface of dielectric and spacer. At the EIT peak i.e. at 1.8 THz frequency, almost all the electric field is confined in the magnetic dipole of the dielectric cube. Also, the direction of electric field at the interface is in the opposite direction which cancels the induced electromagnetic field in the metamaterial structure and results in high transmission and causes EIT.

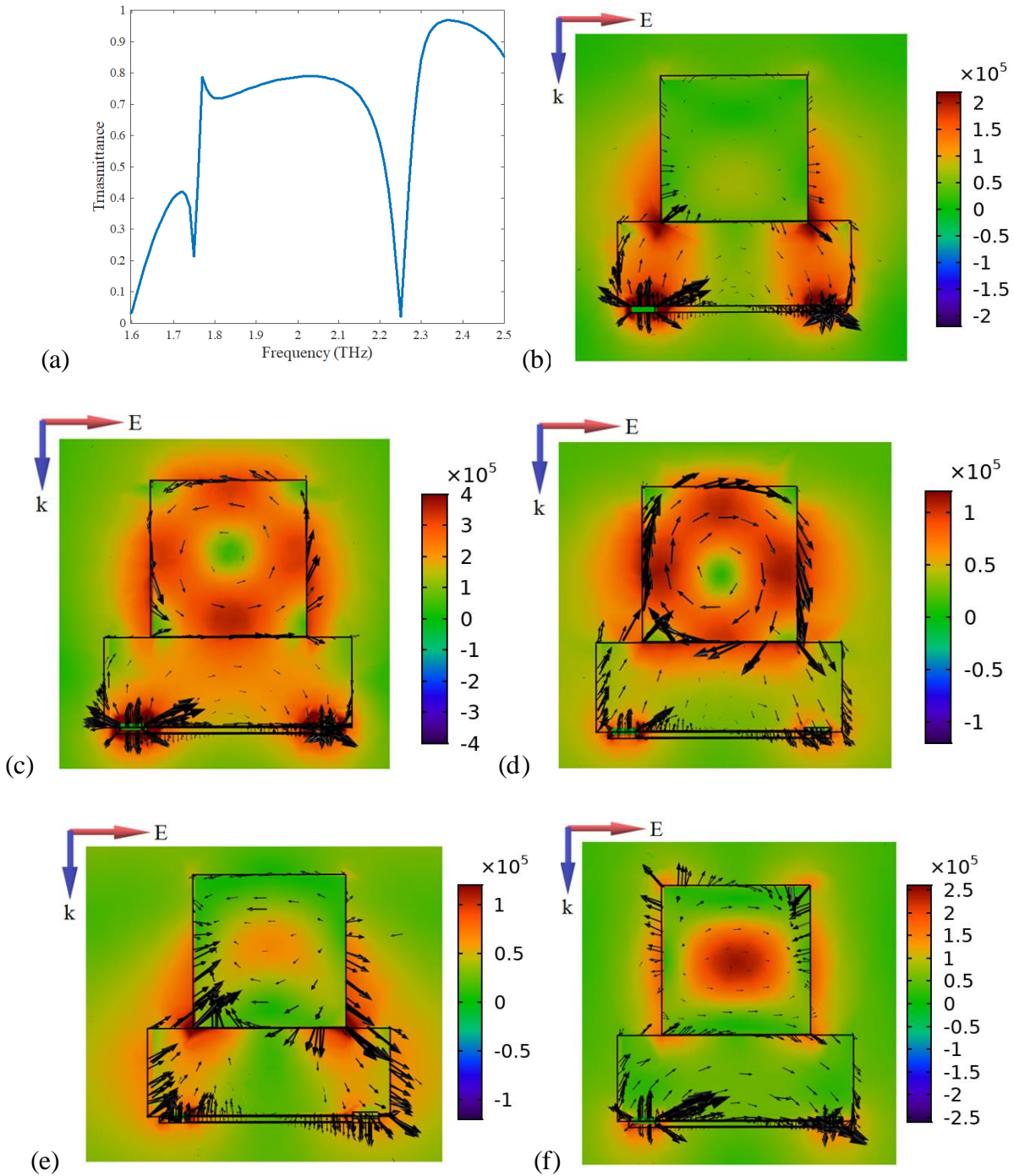


Figure 6.5 (a). Transmittance spectra of EIT resonator for length of the ring,  $l = 50 \mu\text{m}$ . Electric field distribution in the hybrid EIT resonator at (b) 1.6 THz (c) 1.75 THz (d) 1.8 THz (e) 2.1 THz (f) 2.25 THz frequencies. Black arrows in the figures (b) - (f) depict the directions of the electric field.

At 2.1 THz frequency, electric dipole is excited in the dielectric cube and EIT is continued due to the destructive interference of both the bright modes i.e. electric dipoles of metal ring and dielectric cube. The direction of the electric field is persisted in the opposite direction to maintain the EIT effect. At the frequency of 2.25 THz, most of the electric field is confined in

the electric dipole of the dielectric cube and the direction of both the dipoles in the metal ring as well as the dielectric cube are in the same direction confirming dip in the transmission spectra. The quality factors of the resonance dips at 1.75 THz and 2.25 THz have been calculated using the Fano resonance formula and comes out to be 89.5 and 23, respectively.

## 6.4 Delay bandwidth product

Figure 6.6 (a) depicts the transmission phase of the proposed EIT metamaterial structure. The transmission phase experiences a continuous steep change within the transmission window shown by the shadow region in figure 6.6 (a). This continuous steep change in transmission phase leads to the strong dispersion and results in high group delay as shown in the figure 6.6 (b). High group delay is associated with slow light. The slow light has many applications in the field of optical information technology. However, the applications of slow light are limited by small delay bandwidth product. The constant group delay and large bandwidth is a necessary condition for the application of optical buffers. Group delay is almost constant from 1.8 THz to 2.2 THz shown by shadow region in figure 6.6 (b). Due to the large bandwidth, delay bandwidth product comes to be  $\approx 2$ , which is a significant high value as compared to other structures. The group delay,  $\tau_g$  and delay bandwidth product, DBP has been calculated using the formulas [51]

$$\tau_g = -\frac{\partial\phi}{\partial\omega} \quad (6.4)$$

$$\text{DBP} = \tau_g \Delta f \quad (6.5)$$

where,  $\phi$  is the transmission phase in radians and  $\Delta f$  is the frequency bandwidth.

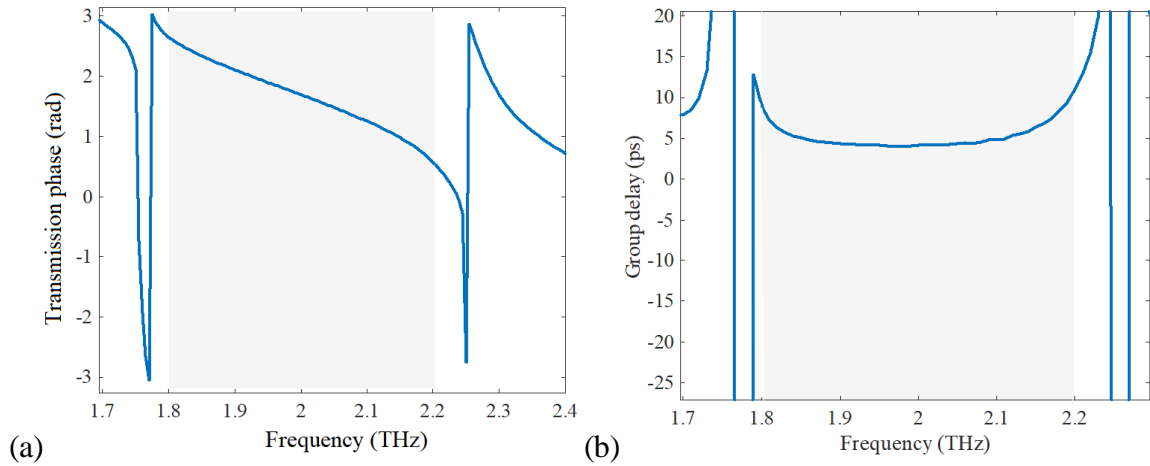


Figure 6.6 (a). Transmission phase in radians and (b) Group delay in picoseconds of the hybrid EIT metamaterial resonator.

## 6.5 Refractive index sensing

The proposed Fano resonator has been utilized to design a Fano resonator based thickness and refractive index sensor by placing the analyte on the top of the resonator as shown in the figure 6.7.

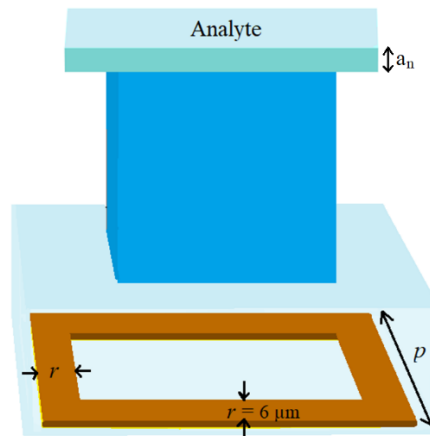


Figure 6.7. Fano resonator as a sensing device with analyte on the top of it.

Initially, while keeping the refractive index of the analyte constant and equal to 1.8, the analyte thickness has been varied. Frequencies of the first and second resonance Fano dips change with changing the thickness of the analyte as shown in the figures 6.8 (a) and 6.8 (b), respectively. Further, the transmission spectra for different refractive indices of the analyte have been shown in the figure 6.9. Here, thickness of the analyte has been taken to be fixed

equal to 5  $\mu\text{m}$ . Red shift has been observed by increasing the refractive index of the analyte for the first and second resonance dips as shown in the figures 6.9 (a) and 6.9 (b), respectively. Figure 6.10 (a) shows the variation in the resonance frequency shift for both first Fano dip ( $\text{FD}_1$ ) and second Fano dip ( $\text{FD}_2$ ) with respect to the analyte by keeping the refractive index fix. It has been observed that there is an increase in the frequency shift by increasing the thickness of the analyte but there is a saturation in frequency shift after 12  $\mu\text{m}$  and 14  $\mu\text{m}$  thickness for the first and second resonance dips, respectively.

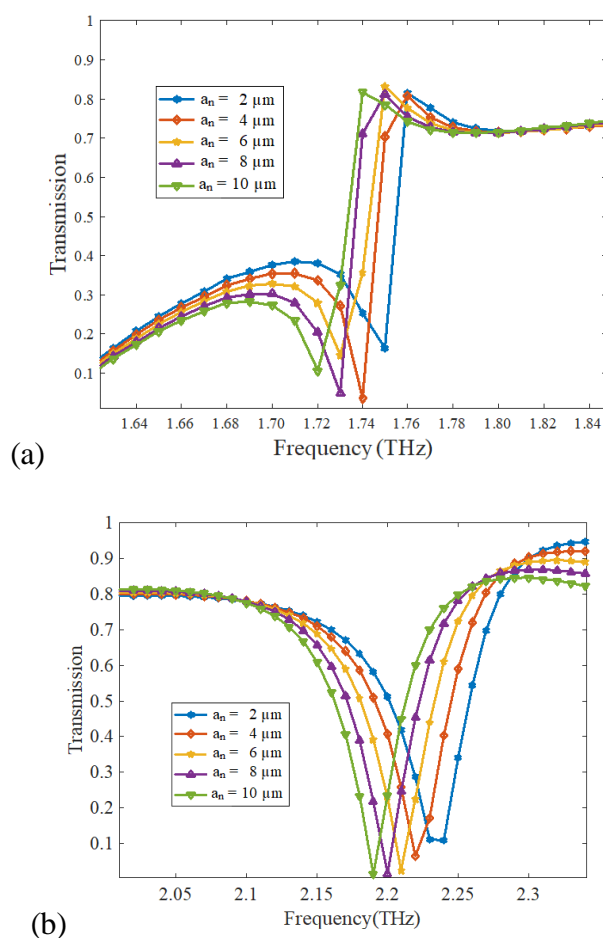


Figure 6.8. Transmission spectra of the Fano resonator for different analyte thicknesses with fixed refractive index of the analyte (a) for first Fano resonance dip and (b) second Fano dip.

Further, to calculate the sensitivity, frequency shift has been plotted with respect to refractive index of the analyte as shown the figure 6.10 (b) by taking the thickness of analyte fixed and equal to 5  $\mu\text{m}$ . The sensitivity  $S = \Delta f / \Delta n$  for first and second Fano dip can be approximated

as 25 GHz/RIU and 50 GHz/RIU, respectively where RIU is the refractive index unit.

Sensitivity in terms of wavelength can be calculated using the formula

$$S = |d\lambda/dn| = \frac{c}{f_0^2} \times \frac{df}{dn} \quad (6.6)$$

where,  $\lambda$  is the wavelength of light,  $n$  is the refractive index of the analyte,  $c$  is the speed of light in vacuum,  $f_0$  is the resonance frequency and  $f$  is the frequency of light. The sensitivities for 5  $\mu\text{m}$  thick analyte of the first and second resonant dips in terms of wavelength comes out to be  $1.4 \times 10^3 \text{ nm/RIU}$  and  $2.9 \times 10^3 \text{ nm/RIU}$ , respectively.

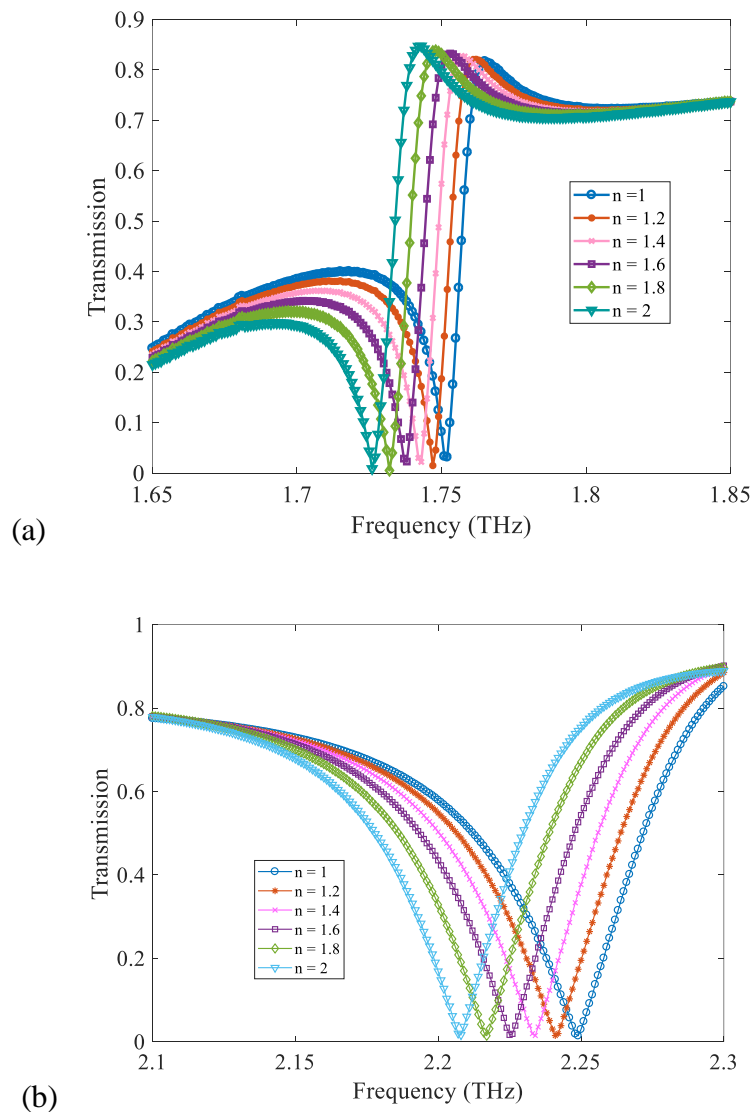


Figure 6.9. Transmission spectra of the Fano resonator for different refractive index of an analyte with fixed thickness of the analyte (a) for first Fano resonance dip and (b) second Fano resonance dip.



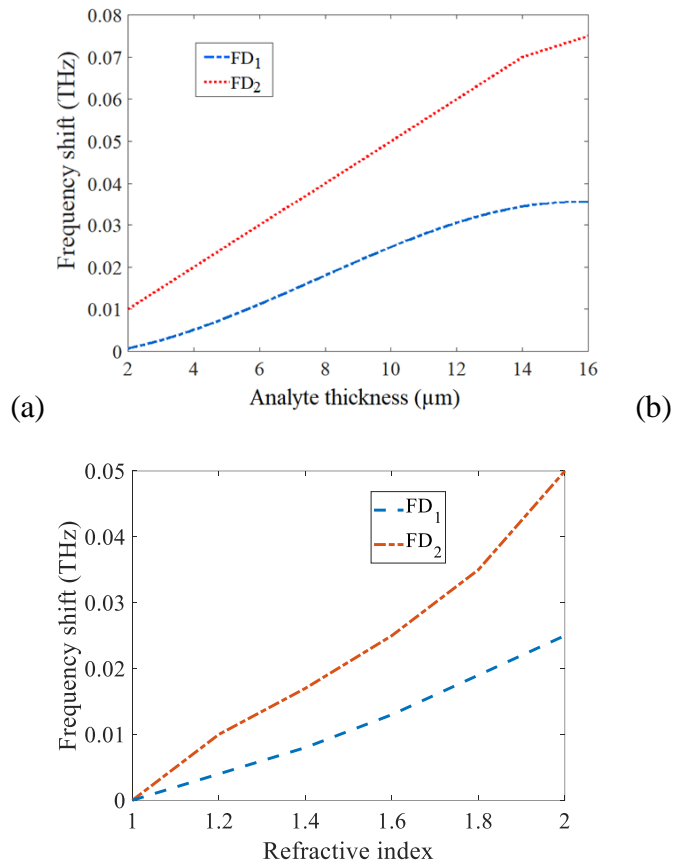


Figure 6.10. Frequency shift with respect to (a) analyte thickness and (b) refractive index of the analyte.

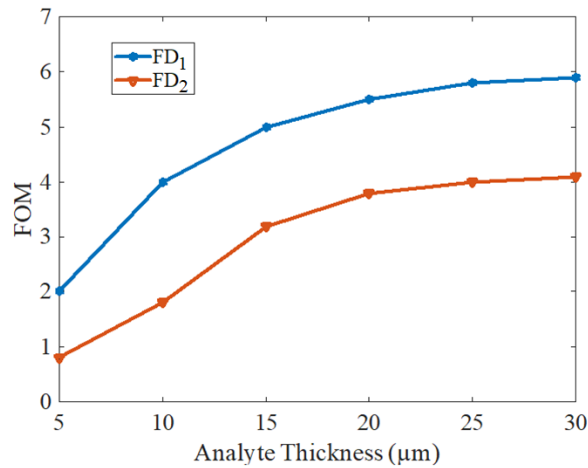


Figure 6.11. Figure of merits of first and second Fano dips with respect to the thickness of the analyte.

Figure of merit (FOM) is an important dimensionless parameter for sensing application and can be calculated as  $\text{FOM} = S/\Delta\nu$  where  $\Delta\nu$  is the linewidth of the resonance. Figure of merits for both the Fano dips FD<sub>1</sub> and FD<sub>2</sub> with respect to the thickness of the analyte has been plotted in the figure 6.11. It has been observed that the FOM of FD<sub>1</sub> is larger than the FOM of the fano

dip FD<sub>2</sub> despite the sensitivity of the FD<sub>2</sub> is larger than the FD<sub>1</sub>. The reason behind the larger FOM of FD<sub>1</sub> is the larger quality factor of the first Fano dip. The linewidth of the first Fano dip is 5 times narrower than the second Fano dip. Figure of merit increases with the increasing analyte thickness and it reaches up to 5 and 3 at the analyte thickness of 15 μm for FD<sub>1</sub> and FD<sub>2</sub>, respectively. By further increasing the analyte thickness, FOM starts saturating and remain approximately constant equal to 6 and 4 for FD<sub>1</sub> and FD<sub>2</sub>, respectively near the analyte thickness 30 μm. Such a high value of figure of merit is due to the high quality factor of the resonances which makes our design a promising candidate for sensing application.

## **6.6 Conclusion**

In conclusion, we propose a hybrid metal-dielectric metamaterial structure to get broadband polarization independent electromagnetically induced transparency in the terahertz region. Metal ring provides us electric dipole which act as bright mode while electric and magnetic dipoles of the dielectric cube excited at different frequencies serve as bright and quasi-dark modes. Electric dipole of the metal ring interferes with the electric as well as magnetic dipoles which creates an EIT window in a broad region from 1.8 THz to 2.2 THz. A steep and constant phase change in transmission results in high group delay of 5 ps in the broad EIT window so that a large delay bandwidth product equal to 2 could be obtained. Therefore, our proposed design can be employed for optical buffers and high transmission band pass filters. In addition to it, the interaction between bright mode of metal ring and quasi-dark mode of dielectric cube results into Fano dip at 1.75 THz with the quality factor of 89.5 and interaction of bright mode of metal ring and bright mode of dielectric cube results into another Fano dip at frequency of 2.25 THz with quality factor of 23. This has been further used to design a Fano resonance based sensor with sensitivities 25 GHz/RIU and 50 GHz/RIU and figure of merits 6 and 4 for the

first and second resonance dips, respectively. Therefore, our proposed design has the potential applications in optical buffers, high transmission band pass filters and sensing.

## References

- [1] S. E. Harris, “Electromagnetically induced transparency” *Physics Today* 50(7), 36–42 (1997).
- [2] M. Fleischhauer, A. Imamoglu and J. P. Marangos, “Electromagnetically induced transparency: Optics in coherent media” *Reviews of Modern Physics*, 77(2), 633 (2005).
- [3] K. J. Boller, A. Imamoglu and S. E. Harris, “Observation of electromagnetically induced transparency” *Physical Review Letters*, 66(20), 2593 (1991).
- [4] B. S. Ham, M. S. Shahriar, M. K. Kim and P. R. Hemmer, “Frequency-selective time-domain optical data storage by electromagnetically induced transparency in a rare-earth-doped solid” *Optics Letters*, 22(24), 1849-1851 (1997).
- [5] J. J. Longdell, E. Fraval, M. J. Sellars, and N. B. Manson, “Stopped light with storage times greater than one second using electromagnetically induced transparency in a solid” *Physical Review Letters*, 95(6), 063601 (2005).
- [6] P. Tassin, L. Zhang, T. Koschny, E. N. Economou and C. M. Soukoulis, “Low-loss metamaterials based on classical electromagnetically induced transparency” *Physical Review Letters*, 102(5), 053901 (2009).
- [7] C. L. Garrido Alzar, M. A. G. Martinez and P. Nussenzevig, “Classical analog of electromagnetically induced transparency” *American Journal of Physics*, 70(1), 37- 41 (2002).
- [8] V. M. Shalaev, “Optical negative-index metamaterials” *Nature Photonics*, 1(1), 41-48 (2007).
- [9] M. Kadic, G. W. Milton, M. van Hecke and M. Wegener, “3D metamaterials” *Nature Reviews Physics*, 1(3), 198-210 (2019).
- [10] S. Hu, D. Liu, H. Lin, J. Chen, Y. Yi and H. Yang, “Analogue of ultra-broadband and polarization-independent electromagnetically induced transparency using planar metamaterial” *Journal of Applied Physics*, 121(12), 123103 (2017).
- [11] H. Chen, H. Zhang, M. Liu, Y. Zhao, S. Liu and Y. Zhang, “Tunable multiple plasmon-induced transparency in three-dimensional Dirac semimetal metamaterials” *Optics Communications*, 423, 57- 62 (2018).
- [12] X. He, X. Yang, S. Li, S. Shi, F. Wu and J. Jiang, “Electrically active manipulation of electromagnetic induced transparency in hybrid terahertz metamaterial” *Optical Materials Express*, 6(10), 3075-3085 (2016).

- [13] L. Zhu, F. Y. Meng, L. Dong, Q. Wu, B. J. Che, J. Gao, J. H. Fu, K. Zhang and G. H. Yang, “Magnetic metamaterial analog of electromagnetically induced transparency and absorption” *Journal of Applied Physics*, 117(17), 17D146 (2015).
- [14] J. Ding, B. Arigong, H. Ren, M. Zhou, J. Shao, M. Lu, Y. Chai, Y. Lin and H. Zhang, “Tuneable complementary metamaterial structures based on graphene for single and multiple transparency windows” *Scientific Reports*, 4, 6128 (2014).
- [15] H. Xu, Y. Lu, Y. Lee and B. S. Ham, “Studies of electromagnetically induced transparency in metamaterials” *Optics Express*, 18(17), 17736-17747 (2010).
- [16] S. Xiao, T. Wang, T. Liu, X. Yan, Z. Li and C. Xu, “Active modulation of electromagnetically induced transparency analogue in terahertz hybrid metal-graphene metamaterials” *Carbon*, 126, 271-278 (2018).
- [17] M. Amin, M. Farhat and H. Bağcı, “A dynamically reconfigurable Fano metamaterial through graphene tuning for switching and sensing applications” *Scientific Reports*, 3, 2105 (2013).
- [18] T. Nakanishi, T. Otani, Y. Tamayama and M. Kitano, “Storage of electromagnetic waves in a metamaterial that mimics electromagnetically induced transparency” *Physical Review B*, 87(16), 161110 (2013).
- [19] Y. F. Hsiao, P. J. Tsai, H. S. Chen, S. X. Lin, C. C. Hung, C. H. Lee, Y. H. Chen, Y. F. Chen, A. Y. Ite and Y. C. Chen, “Highly efficient coherent optical memory based on electromagnetically induced transparency” *Physical Review Letters*, 120(18), 183602 (2018).
- [20] G. Lai, R. Liang, Y. Zhang, Z. Bian, L. Yi, G. Zhan and R. Zhao, “Double plasmonic nanodisks design for electromagnetically induced transparency and slow light” *Optics Express*, 23(5), 6554-6561 (2015).
- [21] Y.Y.Fang, G. Wang, Y. Chen, Y.Xue and H. L. Xu, “Frequency selected coherent optical storage based on electromagnetically induced transparency in rubidium vapor” *Journal of Physics B: Atomic, Molecular and Optical Physics*, 52(2), 025502 (2018).
- [22] N. Liu, L. Langguth, T. Weiss, J. Kästel, M. Fleischhauer, T. Pfau and H. Giessen, “Plasmonic analogue of electromagnetically induced transparency at the Drude damping limit” *Nature Materials*, 8(9), 758 (2009).
- [23] Y. Fan, T. Qiao, F. Zhang, Q. Fu, J. Dong, B. Kong and H. Li, “An electromagnetic modulator based on electrically controllable metamaterial analogue to electromagnetically induced transparency” *Scientific Reports*, 7(1), 1-7 (2017).

- [24] Y. Yue, F. He, L. Chen, F. Shu, X. Jing and Z. Hong, “Analogue of electromagnetically induced transparency in a metal-dielectric bilayer terahertz metamaterial” *Optics Express*, 29(14), 21810-21819 (2021).
- [25] J. Chen, P. Wang, C. Chen, Y. Lu, H. Ming and Q. Zhan, “Plasmonic EIT-like switching in bright-dark-bright plasmon resonators” *Optics express*, 19(7), 5970-5978 (2011).
- [26] L. Zhu, F. Y. Meng, J. H. Fu and Q. Wu, “An electromagnetically induced transparency metamaterial with polarization insensitivity based on multi-quasi-dark modes” *Journal of Physics D: Applied Physics*, 45(44), 445105 (2012).
- [27] F. Xue, S. Liu and X. Kong, “Dual-band plasmon induced transparency metamaterial based on multi-quasi-bright modes” *Physics Letters A*, 127556 (2021).
- [28] M. L. Wan, X. J. Sun, Y. L. Song, P. F. Ji, X. P. Zhang, P. Ding and J. N. He, “Broadband plasmon-induced transparency in plasmonic metasurfaces based on bright-dark-bright mode coupling” *Plasmonics*, 12(5), 1555-1560 (2017).
- [29] S. Hu, D. Liu and H. Yang, “Electromagnetically induced transparency in an integrated metasurface based on bright–dark–bright mode coupling” *Journal of Physics D: Applied Physics*, 52(17), 175305 (2019).
- [30] T. Ma, Q. Huang, H. He, Y. Zhao, X. Lin and Y. Lu, “All-dielectric metamaterial analogue of electromagnetically induced transparency and its sensing application in terahertz range” *Optics Express*, 27(12), 16624-16634 (2019).
- [31] F. Bagci, and B. Akaoglu “Single and multi-band electromagnetic induced transparency-like metamaterials with coupled split ring resonators” *Journal of Applied Physics*, 122(7), 073103 (2017).
- [32] H. M. Li, S. B. Liu, S. Y. Liu, S. Y. Wang, H. F. Zhang, B. R. Bian, and X. K. Kong, “Electromagnetically induced transparency with large delay-bandwidth product induced by magnetic resonance near field coupling to electric resonance” *Applied Physics Letters*, 106(11), 114101 (2015).
- [33] R. Yahiaoui, M. Manjappa, Y. K. Srivastava, and R. Singh, “Active control and switching of broadband electromagnetically induced transparency in symmetric metadevices” *Applied Physics Letters*, 111(2), 021101 (2017).
- [34] C. Y. Chen, I. W. Un, N. H. Tai and T. J. Yen, “Asymmetric coupling between subradiant and superradiant plasmonic resonances and its enhanced sensing performance” *Optics Express*, 17(17), 15372-15380 (2009).
- [35] M. H. Nam, V. T. H. Hanh, N. B. Tuong, B. S. Tung, B. X. Khuyen, V. D. Lam, L. Y. Chen and Y. P. Lee, “Multi-Band Electromagnetically-Induced-Transparency

Metamaterial Based on the Near-Field Coupling of Asymmetric Split-Ring and Cut-Wire Resonators in the GHz Regime” *Crystals*, 11(2), 164 (2021).

- [36] F. Bagci, and B. Akaoglu, “A polarization independent electromagnetically induced transparency-like metamaterial with large group delay and delay-bandwidth product” *Journal of Applied Physics*, 123(17), 173101 (2018).
- [37] S. Hu, D. Liu, H. Lin, J. Chen, Y. Yi and H. Yang, “Analogue of ultra-broadband and polarization-independent electromagnetically induced transparency using planar metamaterial” *Journal of Applied Physics*, 121(12), 123103 (2017).
- [38] S. Hu, D. S. Citrin, and D. Liu, “Flexibly designed polarization-independent electromagnetically induced transparency-like effect via hybrid metal–dielectric terahertz metamaterial” *Journal of Optical Society of America B*, 38(9), C136-C143 (2021).
- [39] L. Xie, W. Gao, J. Shu, Y. Ying, and J. Kono, “Extraordinary sensitivity enhancement by metasurfaces in terahertz detection of antibiotics” *Scientific Reports*, 5, 867 (2015).
- [40] F. Miyamaru, K. Hattori, K. Shiraga, S. Kawashima, S. Suga, T. Nishida, M. W. Takeda, and Y. Ogawa, “Highly Sensitive Terahertz Sensing of Glycerol-Water Mixtures with Metamaterials” *Journal of Infrared, Millimeter and Terahertz Waves*, 35, 198–207 (2014).
- [41] B. You, C. H. Ho, W. J. Zheng, and J. Y. Lu, “Terahertz volatile gas sensing by using polymer microporous membranes” *Optics Express*, 23, 2049 (2015).
- [42] W. Withayachumnankul, H. Lin, K. Serita, C. M. Shah, S. Sriram, M. Bhaskaran, M. Tonouchi, C. Fumeaux and D. Abbott, “Sub-diffraction thin-film sensing with planar terahertz metamaterials” *Optics Express*, 20, 3345-3352 (2012).
- [43] H. Tao, L. R. Chieffo, M. A. Brenckle, S. M. Siebert, M. Liu, A. C. Strikwerda, K. Fan, D. L. Kaplan, X. Zhang, R. D. Averitt and F. G. Omenetto, “Metamaterials on paper as a sensing platform” *Advanced Materials*, 23, 3197-3201 (2011).
- [44] R. Singh, W. Cao, I. Al-Naib, L. Cong, W. Withayachumnankul and W. Zhang, “Ultrasensitive terahertz sensing with high-Q Fano resonances in metasurfaces” *Applied Physics Letters*, 105, 171101 (2014).
- [45] V. A. Fedotov, M. Rose, S. L. Prosvirnin, N. Papasimakis, and N. I. Zheludev, “Sharp Trapped-Mode Resonances in Planar Metamaterials with a Broken Structural Symmetry” *Physical Review Letters*, 99, 147401 (2007).
- [46] Q. Zhang, X. Wen, G. Li, Q. Ruan, J. Wang and Q. Xiong, “Multiple magnetic mode-based Fano resonance in split-ring resonator/disk nanocavities” *ACS Nano*, 11071-11078 (2013).

- [47] H. Cen, F. Wang, R. Liang, Z. Wei, H. Meng, L. Jiang, H. Dong, S. Qin, L. Wang and C. Wang, “Tunable plasmon induced transparency based on bright–bright mode coupling graphene metamaterial” *Optics Communications*, 420, 78-83 (2018).
- [48] L. H. Du, J. Li, Q. Liu, J. H. Zhao, and L. G. Zhu, “High-Q Fano-like resonance based on a symmetric dimer structure and its terahertz sensing application” *Optical Materials Express*, 7(4), 1335-1342 (2017).
- [49] D. G. Mead and L. Genzel, “Interferometry in the asymmetric mode” *Infrared Physics*, 18 (5-6), 555-564 (1978).
- [50] Z. Hao, M. C. Martin, B. Harteneck, S. Cabrini and E. H. Anderson, “Negative index of refraction observed in a single layer of closed ring magnetic dipole resonators” *Applied Physics Letters*, 91(25), 253119 (2007).
- [51] A. Joshi, and M. Xiao, “Electromagnetically induced transparency and its dispersion properties in a four-level Inverted-Y atomic system” *Physics Letters A*, 317(5-6), 370-377 (2003).



# **CHAPTER-7**



---

## CHAPTER-7

---

### CONCLUDING REMARKS AND FUTURE RESEARCH SCOPE

---

This chapter includes concluding remarks about the work incorporated in this thesis and the future perspective of the present work of the thesis. In this thesis, various types of designs related to speciality optical fiber and metamaterials have been proposed and their analysis has been done for different kinds of applications like fiber lasers and amplifiers, communication, nanoantennas, optical buffers or optical memory and sensing.

Photonic crystal fiber which is a speciality optical fiber has been designed in such a way that extended single mode operation could be achieved in the proposed structure of photonic crystal fiber despite large mode area to mitigate the non-linear effects in the wavelength range of 1.0 –1.6  $\mu\text{m}$ . The proposed PCF structure possesses effective-mode area as large as 2147  $\mu\text{m}^2$  at  $\lambda = 1.064 \mu\text{m}$  with confinement losses of  $\sim 1.36 \times 10^{-2}$  dB/m and  $\sim 9.34$  dB/m for FM and FHOM, respectively. Therefore, after a 2.14 m propagating length, the loss of FHOM exceeds 20 dB, and FM mode is only a propagating mode at 1.064  $\mu\text{m}$ . At 1.55  $\mu\text{m}$ , the structure possesses the effective-mode area of FM mode as large as 5688  $\mu\text{m}^2$  with confinement losses of 0.6 dB/m and  $\sim 20.23$  dB/m for FM and FHOM, respectively. After travelling approximately 1 m distance through the PCF, FHOM suffers a more than 20 dB loss while FM offers only a 0.6 dB loss. Therefore, only a 1 m long PCF is sufficient to obtain effective single-mode operation at 1.55  $\mu\text{m}$ . Hence, the proposed PCF structure can be used for high power applications such as high power fiber lasers, amplifiers and communication.

All-dielectric and hybrid metal-dielectric metamaterials have been designed which are useful for the nanoantenna, optical buffers and sensing applications. Electric as well as magnetic dipoles have been optically induced in the nanoparticles. Azimuthally symmetric forward scattering with complete suppression of backward scattering using first Generalized Kerker's condition has been achieved for the longitudinal and transverse modes in the optical region using single ellipsoidal nanoparticle. By changing the direction of the electric field, forward as well as backward scattering can be tuned at different wavelengths. Further, ellipsoidal core (Si) and shell (SiO<sub>2</sub>) metamaterial has been proposed for highly directional properties. In this case forward scattering has been attributed to the Fano resonance. Fano resonant wavelengths in ellipsoidal nanoparticle exhibit higher directivity than the Kerker's type scattering or forward scattering shown by symmetrical structures like sphere and cube. In this thesis, cuboidal nanoparticles in the shape of nanodisk and nanorod have been utilized as dielectric nanoantennas in the visible range. The dimensions of the nanoparticles have been tailored to bring the electric and magnetic dipoles together so that both of them spectrally overlap and on-resonance scattering of electric and magnetic dipole moments take place. There is a Fano dip in the backward scattering and therefore there is an enhancement in the forward scattering which leads to the improvement in directivity and radiation efficiency. These designs have applications in high directional nanoantennas. Directivity and radiation efficiency have been enhanced so that the proposed designs have applications in the development of low loss and ultra-compact optical nanoantennas and high resolution near field microscopy.

Hybrid metal-dielectric metamaterial structure has been designed to get broadband polarization independent electromagnetically induced transparency in the terahertz region. Electric dipole of the metal ring interferes with the electric as well as magnetic dipoles which creates an EIT window in a broad region from 1.8 THz to 2.2 THz. A steep and constant phase change in the transmission results in high group delay of 5 ps in the broad EIT region so that a

large delay bandwidth product equal to 2 could be obtained. Therefore, our proposed design can be employed for optical buffers and high transmission band pass filters. In addition to it, the interaction between bright mode of metal ring and quasi-dark mode of dielectric cube results into Fano dip at 1.75 THz with the quality factor of 89.5 and interaction of bright mode of metal ring and bright mode of dielectric cube results into another Fano dip at frequency of 2.25 THz with quality factor of 23. This has been further used to design a Fano resonance based sensor with sensitivities 25 GHz/RIU and 50 GHz/RIU and figure of merits 6 and 4 for the first and second resonance dips, respectively. Therefore, the proposed design has the potential applications in optical buffers, high transmission band pass filters and sensing.

In this thesis, different types of designs related to speciality optical fiber and metamaterials have been discussed for various applications. However, the designs and their practical applications are not limited to the existing work and can be further expanded as follows:

- Design and analyze all-dielectric metalens on the facet of a photonic crystal fiber which have applications in the high resolution optical imaging, communication, optical lasers and amplifiers, optical tweezers and sensing.
- Design and analyze photoreceptor cells in the eye using dielectric metamaterial nanoantenna for artificial retina applications.
- Active modulation of electromagnetically induced transparency using ultra compact hybrid metamaterial which have application in slow light, nonlinear enhancement, ultrafast optical signal processing.
- Design and analyze hybrid graphene dielectric metamaterial for spectroscopy and sensing applications.